



UNIVERSITÀ degli STUDI di LECCE

Dipartimento di Fisica

Dottorato di Ricerca in Fisica – XXVIII Ciclo

---

# Study of Cosmic Ray Large Scale Anisotropy below the knee with the telescopes of the EEE Project

Ph.D. Student:

**Maria Paola Panetta**

Cotutor

**Prof. Francesco Riggi**

Tutors

**Prof. Ivan De Mitri**

**Prof. Marco Panareo**

---

October 2017



# Contents

<b>1</b>	<b>Cosmic Rays</b>	<b>3</b>
1.1	Short history . . . . .	3
1.2	Energy spectrum of the cosmic rays . . . . .	7
1.3	The cosmic rays composition . . . . .	11
1.4	Acceleration mechanisms . . . . .	13
1.5	Candidate sources of cosmic rays . . . . .	15
1.5.1	Galactic sources: Supernova Remnants . . . . .	17
1.5.2	Extragalactic sources . . . . .	19
1.6	Propagation of the cosmic rays . . . . .	21
1.6.1	Propagation of Galactic cosmic rays . . . . .	21
1.6.2	The transport equation . . . . .	23
1.6.3	Propagation of Extragalactic cosmic rays . . . . .	26
1.7	Diffusion in the Solar System . . . . .	26
1.7.1	The solar Force Field approximation . . . . .	30
1.8	Effect of the Geomagnetic Field . . . . .	31
1.9	Extensive air showers . . . . .	34
1.9.1	The nucleonic component . . . . .	35
1.9.2	The electromagnetic component . . . . .	37
1.9.3	The muonic component . . . . .	38
1.9.4	Energy spectrum . . . . .	42
1.10	Periodic and aperiodic variations at the sea level . . . . .	44
<b>2</b>	<b>Measurements of Anisotropy</b>	<b>47</b>
2.1	Galactic Magnetic Field . . . . .	47
2.2	Cosmic-ray detectors . . . . .	49
2.2.1	Extensive air showers . . . . .	50
2.2.2	Experiments for the EAS detection . . . . .	54

---

<b>3</b>	<b>The Cosmic Radiation and the EEE Project</b>	<b>57</b>
3.1	Telescope Array for the Cosmic Rays detection . . . . .	57
3.2	Sparse Detector Array in High Schools . . . . .	58
3.2.1	ALTA/CZELTA - A sparse very large air shower array	58
3.2.2	NALTA - The North American Large-area Time Co- incidence Arrays . . . . .	59
3.2.3	HiSPARC - High School Project on Astrophysics Re- search with Cosmics . . . . .	61
3.2.4	European Arrays . . . . .	63
3.2.5	MARIACHI - The Mixed Apparatus for Radar Inves- tigation of Cosmic Rays of High Ionization . . . . .	63
3.3	The Extreme Energy Events Project . . . . .	64
3.3.1	Outreach activities . . . . .	65
3.3.2	The EEE telescope Array . . . . .	68
3.4	The Multi-gap RPCs for the EEE Project . . . . .	69
3.4.1	The Resistive Plate Chambers . . . . .	70
3.4.2	RPC working principle . . . . .	71
3.4.3	The Multigap Resistive Plate Chambers . . . . .	73
3.4.4	The EEE MRPCs . . . . .	75
3.5	The EEE Cosmic-Ray station . . . . .	78
3.5.1	Gas System . . . . .	78
3.5.2	Front-End electronics . . . . .	79
3.5.3	High-Voltage system . . . . .	80
3.5.4	The Data Acquisition system . . . . .	82
3.5.5	Trigger system . . . . .	83
3.5.6	Data processing and data quality monitoring . . . . .	85
3.5.7	The coordinated data acquisition . . . . .	86
3.6	The EEE Project physics research Program . . . . .	88
3.6.1	Extensive Atmospheric Showers Detections . . . . .	88
3.6.2	Study of Cosmic rays flux . . . . .	92
3.6.3	Upward-going events . . . . .	94
<b>4</b>	<b>Performance of the EEE MRPC telescopes</b>	<b>97</b>
4.1	Track reconstruction . . . . .	97
4.2	The single MRPC performance . . . . .	99
4.3	The telescope performance measured using cosmic rays . . . .	100
4.4	Time resolution . . . . .	101

---

4.4.1	<i>Time slewing</i> corrections . . . . .	101
4.5	Spatial resolution . . . . .	105
4.6	Efficiency . . . . .	111
4.6.1	Long term stability . . . . .	117
4.7	Comparison with beam-test results . . . . .	123
<b>5</b>	<b>Study of anisotropy effects</b>	<b>125</b>
5.0.1	Transformation of EEE data to equatorial coordinates	126
5.0.2	Muon orientation with respect to primary axis . . . . .	129
5.0.3	Multiple scattering due to the presence of the building	131
5.1	Analysis . . . . .	133
5.1.1	Acceptance and time exposure corrections . . . . .	133
5.2	Overall results and discussion . . . . .	133
<b>6</b>	<b>Conclusion</b>	<b>141</b>
<b>A</b>	<b>Appendix: LV/HV Voltage Control System</b>	<b>143</b>
	<b>Bibliography</b>	<b>149</b>



# Introduction

Cosmic rays below the knee,  $10^{15}$ eV, are of galactic origin, since the transition between galactic and extragalactic origin lies around energies of  $10^{18}$ - $10^{19}$ eV. Galactic cosmic rays are expected to be nearly isotropic, due to their interaction with the galactic magnetic field over the long path to the Earth. Observation of cosmic rays at energies sensibly smaller than  $10^{15}$ eV is a useful tool to inspect the magnetic field structure in the interstellar environment close to our Solar System. In this energy range small anisotropies may be induced by large scale as well as local magnetic field features, which may cause deviations from the isotropic diffusion model. At very low primary energies, of the order of  $\sim 1$  TeV, even sizable effects from the heliosphere may be expected on the cosmic ray distributions. The Compton-Getting effect, introduced in 1935 [19], predicts a dipole component in the cosmic ray anisotropy, due to the motion of the observer with respect to an isotropic cosmic ray plasma rest frame. For instance the anisotropy arising from the Earth motion around the Sun is predicted to be of the order of  $10^{-4}$  and has been sometimes observed [20] [21]. Such measurements are based on the assumption that the direction of secondary muons mirrors, within a few degrees, that of the primary particle. If the search for point sources is not of special concern in this low energy range, the distribution over extended area in equatorial coordinates allows not only to observe the existence of anisotropies but also to investigate its shape.

Secondary cosmic muons at the sea level, may give the possibility to explore the sky in a peculiar energy region, where the influence of local heliosphere and terrestrial phenomena could produce non uniformity over space and time. A large statistics is required to produce significant maps where excess or deficit regions might be evidenced.

The EEE network [100] employs more than 50 MRPC telescopes, spanning more than  $10^\circ$  in latitude and  $11^\circ$  in longitude. The detectors are able to

detect cosmic muons and reconstruct their arrival direction, thus it is a good candidate to collect enough data to explore the sky at sub-TeV energies [150]. Continuous running of the EEE telescopes allows to search for variations in the sky map along different periods of the year and over different sites.

In this thesis a study of the angular distributions of the secondary cosmic rays with primary energies  $\leq$  TeV is reported, with a particular attention to the EEE array performance. Typical geometrical acceptances and time exposure of the EEE telescopes were evaluated. Data from different samples of events, more than  $10^{10}$  collected by different EEE telescopes in different periods of the year were then used to produce sky maps in equatorial coordinates and check for isotropy/anisotropy effects.

# Chapter 1

## Cosmic Rays

Cosmic rays are high energy charged particles, originating in outer space, that travel at nearly the speed of light and strike the Earth from all directions. Most cosmic rays are the nuclei of atoms, ranging from the lightest to the heaviest elements in the periodic table. They also include high energy electrons, positrons, and other subatomic particles. The term *cosmic rays* usually refers to galactic extragalactic cosmic rays, which originate in sources outside the solar system, distributed throughout our Milky Way galaxy. However, this term has also come to include other classes of energetic particles in space, including nuclei and electrons accelerated in association with energetic events on the Sun (called solar energetic particles), and particles accelerated in interplanetary space.

### 1.1 Short history

The history of cosmic rays started in the 1780s when French physicist Charles-Augustin de Coulomb noticed that an electrically charged sphere spontaneously lost its charge, which at the time was strange as scientists believed that air was an insulator, rather than a conductor. In 1879 Crookes performed some studies and observed the influence of the air pressure inside the electroscope on the time to the electroscope's discharge, and conclude that the speed of the discharge decreases with the pressure. After Becquerel's discovery of the spontaneous decay of radioactive elements in 1896, the electroscope was used to measure the radioactivity level of the materials and further investigations showed that air became a conductor when the molecules were ionized by charged particles or X-rays. The history

continued with an exploration of charged gases in closed vessels at the beginning of 20th century. Two Canadian groups, McLennan and Burton [1] and Rutherford and Cooke [2] noticed in 1903 that the leakage of electric charge from an electroscope within an air-tight metal chamber could be reduced as much as 30% by enclosing the chamber within several centimeters thick metal shield. An additional lead failed to reduce the radiation further. The loss of the charge of the enclosed electroscope was due to some highly penetrating rays and it was attributed to radioactive materials in the ground. The most penetrating radiation known at that time was  $\gamma$  ray with well explored attenuation coefficient in the air but it is known when  $\gamma$  ray radiation passes through any matter, its intensity exponentially decreases. Within following years it was found that the radiation did not decrease as rapidly with an altitude as was expected. The first report upon this point was made by Dutch Jesuit priest and physicist Theodor Wulf [4], who made measurements in a lime-pit near the town Brandenburg and then at the top of the Eiffel Tower, the highest construction in the world in those days (330 m altitude). He measured about  $3.5 \text{ ions} \times \text{cm}^{-3}$  on the top and  $6 \text{ ions} \times \text{cm}^{-3}$  on the bottom, which was much less decrease than expected. Later Swiss physicist Gockel [3] started to take an enclosed electroscope in a balloon above the ground. After this first observations, between 1907 and 1911 Domenico Pacini performed experiments, observing variations of the rate of ionization on mountains, over the Bracciano lake, over the sea close to Livorno, and at a depth of 3 meters underwater. In an experiment performed in June 1911, Pacini concluded that ionization underwater was significantly lower than on the sea surface. He could then demonstrate that a certain part of the ionization itself must be due to sources other than the radioactivity of the Earth, [6] thus contributing to the discovery of cosmic rays.

The cosmic ray discovery is commonly attributed to Viktor F. Hess (1912). Also Hess had speculated whether the source of ionization is in the sky rather than in the Earth's crust, and after many balloon flights, he could reveal that the electroscope on board discharged considerably with height. He realized ten balloon flights with pressure and thermal stable instruments: two flights in 1911, seven in 1912, and one in 1913. During his first six flights he did not succeed to reach sufficient height above the ground. The seventh balloon ascended up to the altitude over 5 km (without an air mask) on August 7, 1912. Hess found that although electroscope's rate of discharge

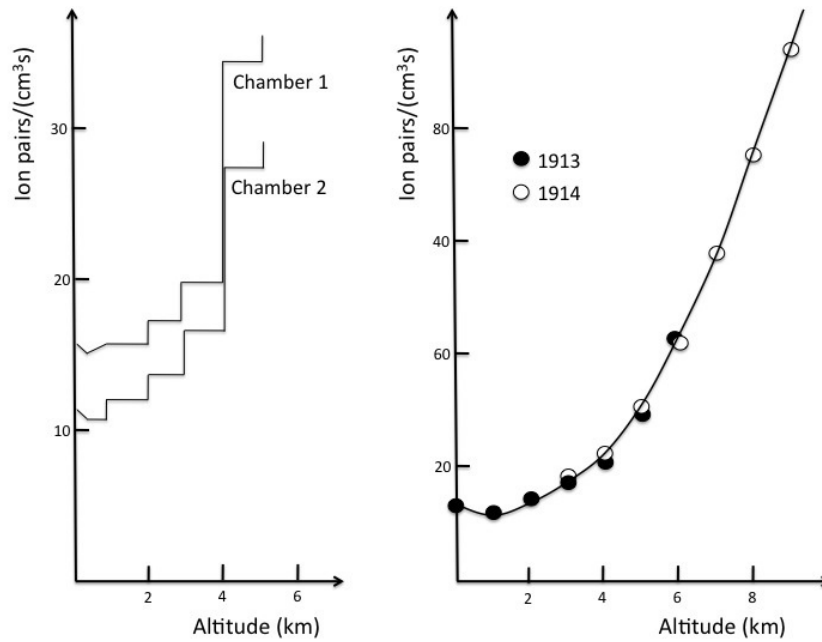


Figure 1.1: Increase of ionization with altitude as measured by Hess in 1912 (left) and by Kolhorster (right).

decreased initially up to about 610 m, thereafter it increased considerably, being four times larger at 4880 m than at sea level, shown in Fig.1.1. He concluded: *The results of the present observations seem to be most readily explained by the assumption that a radiation of very high penetrating power enters our atmosphere from above, and still produces in the lower layers a part of the ionization observed in closed vessels* [5]. After five balloon flights made during night and one during an almost total eclipse of the Sun, Hess further concluded that, since he observed no change of the rate of discharge, the Sun could not itself be the main source of the radiation.

Hess's results were confirmed by W. Kolhorster [8] Fig.1.1, in a number of flights up to 9200 m, and he was awarded the Nobel Prize in physics in 1936 (by the time Pacini was dead) for the discovery of the cosmic rays.

In the twenties American physicist Robert Millikan made further studies by launching balloons and by submerging electroscopes in lakes at different depths. He found that a depth of water equal in mass to the difference in atmospheric altitudes gave the same readings [7]. Thus it was proved that rays must come from above. Millikan believed that his measurements proved that the primary were  $\gamma$  rays, he named them: *cosmic rays*, and that secondary electrons were produced in the atmosphere by Compton scattering.

For many years there was discussion whether cosmic rays are neutral  $\gamma$  rays or charged particles. The invention of the Geiger-Muller detector in 1929 enabled the individual cosmic rays observations. Bothe and Kolhorster built a coincidence counter by using two Geiger-Muller counters, one placed above the other [9]. They found that simultaneous discharges of the two detectors occurred very frequently, even when a strong absorber was placed between the detectors. The experiment strongly indicated that these particles are charged with sufficiently penetrating power, so they have to be very energetic. If charged particles constituted a majority of cosmic rays, they should have to be deflected by the geomagnetic field and the cosmic ray flux should have to be strongest at the poles and weakest at the equator. In 1932 Arthur Compton presented a result of series of his observations

TABLE I. *Cosmic ray intensity at different localities*  
(Ions per cc per sec. through 5 cm Pb, 2.5 cm Cu and 0.5 cm Fe)

Location	Lat.	Long.	Elev.	Barom.	$I_C$	$I_L$	Date
1 Mt. Evans	40°N	106°W	14,200ft	17.61in	6.88 ions	0.57	9/31
2 Summit Lake	40 N	106 W	12,700	18.70	5.84	0.34	9/31
3 Denver	40 N	105 W	5300	24.8	2.93	—	9/31
4 Jungfraujoch	47 N	6 E	11,400	19.70	5.08	0.51	10/31
5 Haleakala	21 N	156 W	9300	21.47	$3.35 \pm 0.05$	0.60	4/32
6 Idlewild	21 N	156 W	4200	25.99	$2.40 \pm 0.05$	0.37	4/32
7 Honolulu	21 N	158 W	70	30.09	$1.89 \pm 0.02$	0.11	4/32
8 S. S. Aorangi	4 S	173 W	60	29.65	$1.83 \pm 0.05$	0.32	4/32
9 Southern Alps	44 S	170 E	6700	23.69	$3.39 \pm 0.05$	0.22	4/32
10 Southern Alps	44 S	170 E	3900	26.10	$2.70 \pm 0.04$	0.21	4/32
11 Dunedin	46 S	170 E	80	30.08	$2.16 \pm 0.03$	0.11	4/32
12 Wellington	41 S	175 E	400	29.85	$2.16 \pm 0.03$	0.12	5/32

Figure 1.2: Latitude dependence of cosmic ray intensity. Local radiation sources were shielded by copper and lead shells [14].

which showed variation of cosmic ray flux with the latitude (Tab. 1.2). In 1934 Bruno Rossi reported an observation of near simultaneous discharges in two Geiger counters widely separated in a horizontal plane during a test of equipment he was using in a measurement of the east-west effect [89]. Three years later Pierre Auger and Roland Maze, unaware of Rossi's earlier report, detected the same phenomenon and investigated it in more detail [11]. Their experiments in Alps revealed that the cosmic radiation events were coincident in time on very large scale (at more than 200 m distance) and they concluded that a primary particles interact with the atoms and molecules in the atmosphere initiating a large air showers. From electromagnetic cascade theory Auger and his colleagues estimated an energy of the incoming particle creating Extensive Air Showers (EAS) to be at least  $10^{15}$  eV.

A wide variety of experimental investigations demonstrated that the primary cosmic rays striking Earth's atmosphere are mostly positively charged particles. There were also some indirect confirmations, such as an explanation of night aurorae phenomena in the polar zone [13]. After these studies a common consensus about nature of cosmic rays has emerged. It was clear that cosmic rays are relativistic charged atomic nuclei moving through space which strike the Earth's atmosphere each generating cascades of secondary particles. The secondary radiation observed at ground level was composed primarily of a *soft component* of electrons and photons and a *hard component* of highly penetrating particles, muons, discovered by Carl D. Anderson and Seth Neddermeyer in 1936 [15].

Discoveries in cosmic ray field stimulated widespread interest among physicists, it led to the genesis of two major fields of research: high-energy elementary-particle physics and cosmic ray astrophysics. First antiparticle, the positron, was discovered in 1932 by Carl Anderson by passing cosmic rays through a cloud chamber and a lead plate surrounded by a magnet [16]. Hess and Anderson shared the Nobel prize in physics in 1936.

Many aspects of the cosmic rays have been examined and discovered since then, the energies of the primary particles cover an energy range from  $10^9$  eV up to  $10^{20}$  eV. But there are still essential questions, which could not be answered yet, like the type of sources the cosmic rays are coming from, which mechanisms are accelerating the cosmic rays to such high energies, how they diffuse in the extragalactic, galactic and interplanetary space. In this chapter, a brief overview on the the cosmic radiation's properties are given.

## 1.2 Energy spectrum of the cosmic rays

Since the discovery of cosmic rays, their energy spectrum has been measured by many experiments at the different energy. It covers an energy range of about 11 orders of magnitude and about 30 orders of magnitude in the flux of the cosmic rays. In Fig.1.3, the energy spectrum measured by different experiments is shown. The energy spectrum, also called the differential flux of cosmic rays can be described by a power law:

$$\frac{dN(E)}{dE} = k E^{-\gamma}$$

with a spectral index  $\gamma$  in the range of 2.5-3.2. Particles up to an energy of about 100 TeV can be measured directly by experiments on balloons or satellites, but for higher energies the flux is too small to measure cosmic rays directly, because their sensitive detection area in the order of  $\sim 1 \text{ m}^2$  is too small, as shown in Fig.1.3. Therefore, experiments have to observe the cosmic radiation indirectly by measuring extensive air showers. These ground based experiments use the atmosphere above them as detection medium, and hence, the detection area can be increased considerably compared to balloon or satellite experiments.

The energy spectrum, in Fig..1.3, shows some features where the spectral index is changing:

- 2.7 for  $E < 10^{15} \text{ eV}$
- 3.1 for  $10^{15} \text{ eV} < E < 10^{19} \text{ eV}$
- 2.75 for  $E > 10^{19} \text{ eV}$

The main of these features is the so-called and it was discovered in 1958: at about 4 PeV the spectral index changes from about 2.7 to 3.1 [27]. The first

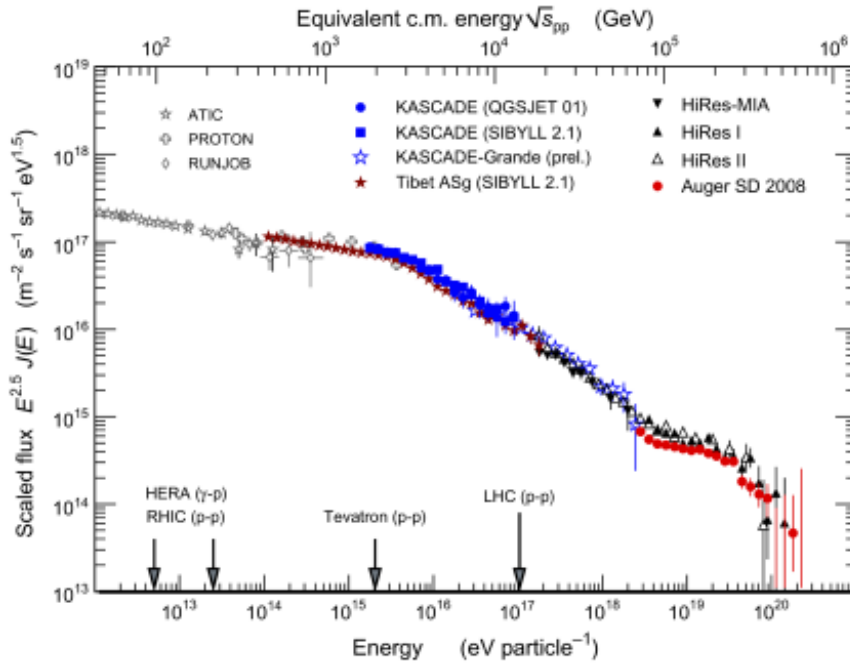


Figure 1.3: Cosmic rays energy spectrum measured by various experiments. A comparison with the energies reached by different accelerators is indicated. The figure was taken from [18].

important feature, the spectral softening, was discovered in 1958: at about 4 PeV. It is usually referred to as the cosmic ray *knee*. It is believed that cosmic rays up to this energy originate inside our galaxy and that the change in spectral index is associated with a change in the chemical composition of the cosmic ray particles, see the section below 1.3. The second change in the spectral index is a spectral hardening at an energy of a few EeV, known as *ankle*. The origin of this change can be explained by a transition from cosmic rays with galactic sources to radiation with extragalactic sources. Based on magnetic confinement arguments, it is believed that cosmic rays with energies beyond the ankle cannot be confined in the galaxy volume by the galactic magnetic field and so this break could mark the transition between the different sources. Larmor radius for a particle with charge

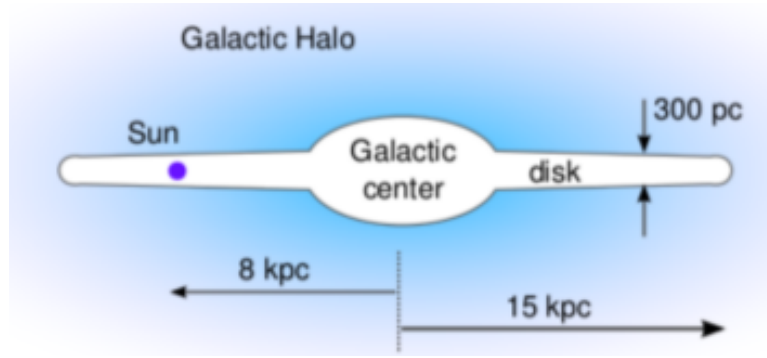


Figure 1.4: Simplified model of the structure of the Milky Way galaxy.

$q = eZ$ , velocity  $v = \beta c$ , immersed in a magnetic field  $\overline{B}$ , is given by:

$$r_l = \frac{E}{Z|e|\overline{B}\beta c}. \quad (1.1)$$

As the Galaxy is filled with a magnetic field whose average intensity is  $B \sim 4\mu G$  [28], we obtain the following Larmor radii  $r_l$  for protons at different energies:

$$r_{l(E=10^{12}eV)} = 3 \cdot 10^{-4} pc \quad ; \quad r_{l(E=10^{15}eV)} = 0.3 pc \quad ; \quad r_{l(E=10^{18}eV)} = 300 pc. \quad (1.2)$$

For particles below  $10^{18}$  eV the Larmor radius is comparable to the dimension of the Galactic disk (Fig.1.4), therefore they are strongly constrained inside the galactic volume by the galactic magnetic field.

The presence of a second knee at about  $4 < 10^{17}$  eV is suggested by the

measurements of Yakutsk [29], Haverah Park [30], Fly's Eye [31], Auger [18]; these experiments see a change of the spectral index from about 3.0 to about 3.3; on the other hand, the experiments Akeno [32] and Agasa [45] do not see the presence of a second knee.

Finally, another feature of the energy spectrum was predicted in 1966 by K. Greisen, G. Zatsepin and V. Kuzmin [35] [36]. They theorized the flux should be strongly suppressed at energies above  $5 \cdot 10^{19}$  eV, the Extreme Energy Cosmic Rays (EECR) since, during propagation, Extreme Energy (EE) protons would interact with 2.7 K Cosmic Microwave Background (CMB) photons. This cutoff is referred to as *GZK-cutoff*. The CMB radiation in the EE proton rest frame is in the order of 200 MeV and more. It exceeds the threshold energy for inelastic pion-production through the  $\Delta^+$  resonance, which immediately decays in the following final state:

$$p + \gamma_{CMB} \rightarrow \Delta^+ \rightarrow n + \pi^+, \quad p + \gamma_{CMB} \rightarrow \Delta^+ \rightarrow p + \pi^0.$$

Since the produced neutrons decay into  $n \rightarrow p e^- \nu_e$ , a proton is always present in the final state, and high-energy photons and neutrinos are produced ( $\pi^0 \rightarrow \gamma \gamma$ ,  $\pi^+ \rightarrow \nu_\mu \mu^+$ ,  $\mu^+ \rightarrow e^+ \nu_\mu \bar{\nu}_e$ ). This process should limit the energy loss length of protons for pion-production to a few tens of Mpc, and the EECR should lose energy in these as long as their energy is above the threshold energy.

$$l_{p\gamma} = \frac{1}{\Delta E_p/E \times \sigma_{p\gamma} \times n_{\gamma_{CMB}}} = 30 \text{ Mpc}. \quad (1.3)$$

where  $\frac{\Delta E_p}{E} \sim \frac{m_\pi}{m_p} \simeq 0.1$  is the fraction of energy lost by the proton;

$\sigma_{p\gamma} \simeq 250 \mu\text{b}$  is the cross-section of the processes  $\gamma + p \rightarrow \pi^0 + p$  and  $\gamma + p \rightarrow \pi^+ + n$ , it is a function of the photon energy in the laboratory frame [37];

$n_\gamma \simeq 400 \text{ cm}^{-3}$  is the CMB photons number density.

The GZK cut-off is not the only effect that can affect the cosmic ray energy spectrum [38], at least other two aspects should be considered. During the propagation, protons can scatter off CMB photons and an electron-positron couple can be produced in the process:

$$p + \gamma \rightarrow p + e^+ + e^- \quad (1.4)$$

with a threshold energy given by  $E_p \geq \frac{m_e m_p}{E_\gamma} \simeq 2 \cdot 10^{18}$ , and where  $E_\gamma$  is the average energy of the CMB photon. The cross section of this process is comparable with that of the production of the  $\Delta_+$  resonance, while the

fraction of energy loss has a value about two orders of magnitude smaller, and the energy loss length about two orders of magnitude large  $l = 10^3 \text{ Mpc}$ . Finally, an adiabatic energy loss, independent on cosmic rays energy, is due to the expansion of the Universe:  $l_{ad} = \frac{c}{H_0} \simeq 4 \text{ Gpc}$ , where  $1/H_0 \simeq 13.7 \text{ Gy}$  is the Hubble time.

There is not completely agreement if these cutoffs are really present in the energy spectrum. Measurements by Agasa [45] show no decrease of the flux for primary energies above  $10^{20} \text{ eV}$  indicating no GZK-cutoff, whereas, the results from HiRes [34] are in agreement with the predicted cutoff energy at about  $5 < 10^{19} \text{ eV}$ . This is also supported by the results of Auger [46], [47], [48].

### 1.3 The cosmic rays composition

The study of the chemical composition of cosmic rays can help to reveal their origin and their acceleration mechanisms. At around  $10^{12} \text{ eV}$ , the flux corresponds to about one incident particle per square meter per second. This particle rate allows the construction of small detectors that can be mounted on balloons or spacecrafts to detect primary cosmic rays directly. However Only for energies up to  $10^{14} \text{ eV}$ , the chemical composition is known precisely due to balloon and satellite experiments. Here the cosmic radiation consists of about 98% of hadrons and 2% of electrons and photons. 85% of the hadronic component are protons and 12% are helium nuclei, the rest are fully ionized nuclei of heavier elements up to iron. In Fig. 1.5 the relative elemental abundance in the solar system is compared with the relative abundance of the cosmic radiation. The abundances are normalized to the abundance of silicon. The abundances in the solar system and in the cosmic radiation are in good agreement, which suggests that the accelerated matter arriving on Earth comes from a region whose surrounding material has the same chemical composition of our Solar System, i.e. the elements are produced by the same nucleosynthesis processes that originated the Sun and the planets..

However there are also disagreements.

- ◇ Two groups of elements, Li, Be, B ( $Z = 3-5$ ) at low masses and Sc, Ti, V, Cr, Mn ( $Z = 20 - 25$ ) at higher masses, are much more abundant in the cosmic rays than in the solar system. In nucleosynthesis these

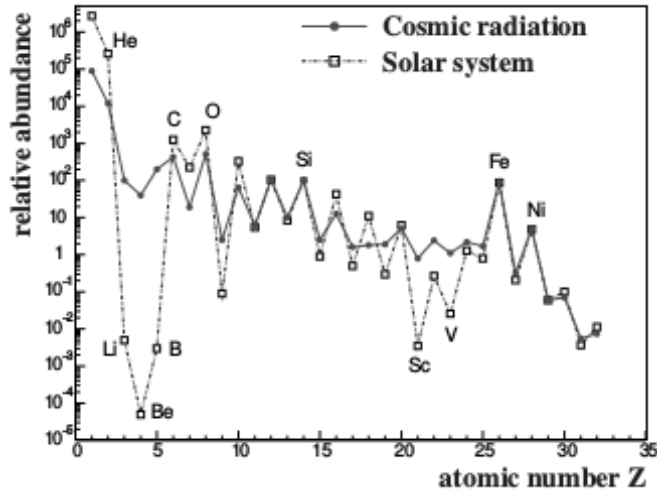


Figure 1.5: Comparison of the relative elemental abundance in the solar system and the cosmic radiation [39].

elements are only produced to a small amount and these are secondary cosmic rays originate in the fragmentation of stable and abundant primary nuclei such as Carbon, Nitrogen and Oxygen ( $Z = 6-8$ ) for the lighter elements, and Iron ( $Z = 26$ ) for the heavier elements in spallation processes that occur in the interstellar medium. The ratio of these secondary to primary abundances provides information about the propagation of cosmic rays in the galaxy, and will be discussed in section 1.4.

- ◇ Secondly, the abundance of hydrogen and helium is lower in the cosmic rays compared to the abundance in the solar system. In the acceleration models, only charged particles can be accelerated efficiently. The ionization energies of hydrogen and helium are relatively high. Therefore, a sufficient amount of these elements are not ionized, and hence not accelerated. Therefore, the abundance of these elements is decreased in the cosmic rays compared to their abundance in the solar system.

Recent balloon measurements [40] indicate that protons dominate the flux up to about 10 TeV. A hardening in the helium spectrum above 200 GeV could make it dominant at higher energies. A change in composition as a function of energy is consistent with current theories of cosmic ray confinement in the galaxy. The Milky Way magnetic field has a strength of about  $2 \mu\text{G}$  in

the vicinity of the Sun [28]. The Larmor radius  $r_l$  of the cosmic rays, from the equation 1.1, increases linearly with energy and is also a function of particle rigidity  $R = r_l B c = pc/Ze$ . Thus the location of the knee in energy should be different for different chemical elements, and the composition of Galactic cosmic rays should become heavier in the knee region, as heavier elements experience a spectral softening at higher energies. Data from air shower arrays, indicates that such a transition to heavier elements indeed occurs [41] [42].

At higher energies, near the ankle region ( $E \sim 3 \cdot 10^{18} \text{ eV}$ ) where extragalactic cosmic rays are expected to become dominant. The composition turns light once again and is consistent with a proton-dominated flux. At the highest observable energies  $E > 10^{19} \text{ eV}$  the results are so far inconclusive. While the Auger Collaboration has reported a composition consistent with iron nuclei [43], the Telescope Array collaboration has indicated that their measurements agree well with a proton-only composition [44]. Important systematic uncertainties in these measurements are due to the lack of knowledge about hadronic interactions at center-of-mass energies higher than several TeV.

## 1.4 Acceleration mechanisms

An important theoretical challenge is the identification of processes that could accelerate particles up to the extreme energies observed in the cosmic ray flux. A model has to describe the characteristics of the cosmic rays, like the observed chemical abundances of the elements, their observed energy density of  $E \sim 1 \text{ eV/cm}^3$ , or the power law of the energy spectrum. In particular the spectral index observed,  $\gamma \sim 2.7$  up the knee and  $\gamma \sim 3.1$  above, should be corrected for propagation in the Galaxy and a spectral index  $\gamma \sim 2$  at the source is expected, see sections 1.2 and 1.6.1.

Contemporary models of the acceleration mechanisms belong to three categories: stochastic acceleration models, direct acceleration models, or top-down models; the different models could also be concurrent.

In stochastic models the cosmic ray particles achieve their final energy by many elastic scattering with magnetized clouds in interstellar space, each with a small increase of the energy. In 1949, Enrico Fermi theorized a mechanism [50] for particles to gain energy through their interaction with magnetized clouds. In this model the particles involved in head-on collisions

with the cloud will gain energy and those involved in tail-end collisions will lose energy. On average, however, head-on collisions are more probable and particles could gain energy over many collisions. If a charged particle of mass  $m$  is magnetically reflected by a gas cloud of mass  $M$  moving with  $\beta_M$ , where  $M \gg m$  and  $M \propto M_\odot$  (solar mass  $M_\odot = 1,99 \cdot 10^{33}$ g), on average at each reflection, the particle gains energy proportional to  $\beta_M^2$ :

$$\frac{\langle E_f \rangle}{E_i} \simeq 1 + \frac{4}{3}\beta_M^2 + \dots \quad (1.5)$$

Since the energy gain is quadratic, this process is known as *second order Fermi acceleration*. Due to the low cloud velocities the energy gain per collision is very small which implies that this process requires very long times to accelerate particles.

Due to energy losses that may occur between collisions, this mechanism is only efficient for particles with a minimum injection energy. The injection energy could be provided by a different process, such as acceleration in astrophysical shocks. In a shock front, two different regions with different characteristics of the magnetic field are generated. A particle traverses a shock wave several times and it is reflected on either side by a diffusive scattering. The relative energy increase is then simply [51]:

$$\left\langle \frac{\Delta E}{E} \right\rangle \sim \frac{4}{3}\beta_M. \quad (1.6)$$

Since the final energy increase is linear in the velocity of the gas, this process is known as *first order Fermi acceleration*, even though it was not originally postulated by Fermi. Particles can be accelerated to energies of up to 100 TeV through this process, which provides the second order mechanism with the required injection energy to go to higher energies [52]. The energy that a particle can achieve depends on the number of crossings in the wave before it escapes, therefore the maximum energy such a process can attain is limited by the lifetime of the shock front. Moreover not only powerful shocks are needed but also strong magnetic fields that can confine the particles while being accelerated. One advantage of this model is that it results in a power law for the energy spectrum with a spectral index of  $\gamma \sim 2.0$  almost independent of the configuration of the shock wave front [53]. Furthermore there are several astrophysical objects, which could produce such shock waves, supernova explosions are one of the most promising candidates,

as it is explained in the next paragraph 1.5.1. Measurements of TeV gamma rays,  $\gamma$  rays, which can be created by the collisions of accelerated protons with the interstellar medium, showed, that hadrons can be accelerated in shock wave fronts [54], [55]. Other sources of shock waves could be the termination shock of a stellar wind [56], the termination shock of a galactic wind [57], or the atmosphere of a neighboring star of a pulsar, which is hit by the pulsar wind [58]. All these galactic candidates are able to accelerate cosmic rays to a maximum energy in the order of  $10^{16}$  eV.

Secondly, in direct acceleration models the cosmic ray particles are accelerated very efficiently in a few steps or even in one single step. These models require strong magnetic and electric fields in order to accelerate particles. Possible objects are polar caps of rapidly rotating pulsars [59], relativistic jets from Active Galactic Nuclei (AGN), or supernovae, that emit highly relativistic jets, which accelerate the cosmic ray particles. The models for this category are describing sources of the cosmic radiation which can be also extragalactic.

Finally, in top-down models the origin of the ultra high cosmic radiation is explained by yet undiscovered phenomena. In this more exotic scenarios, ultra high energy cosmic rays, UHECRs, are created in the decay of high mass topological defects left as relics from the phase transitions after the Big Bang, or super-heavy dark matter particles. Top-down models usually predict an important flux of UHE gamma rays and neutrinos associated with the creation of cosmic rays, and have been constrained using data from air shower arrays. An overview about top-down models is given in [60].

The two latter categories of models, the direct acceleration and the top-down scenarios, predict primary energies of the cosmic radiation above  $10^{16}$  eV, whereas the origin of the cosmic rays up to approximately  $10^{16}$  eV are probably of galactic origin, see section 1.2.

## 1.5 Candidate sources of cosmic rays

A galactic or extragalactic source can be considered a good candidate as a cosmic rays accelerator if it both provides powerful shocks and magnetic fields that can confine the particles for such a time that it can be accelerated up to the highest observed energies. Once the Larmor radius of a particle is comparable to the size of the acceleration region, the probability of escape from the region increases significantly. This relation between maximum

achievable energy  $E_{max}$ , size  $R$ , and magnetic field strength  $B$  is known as the *Hillas criterion* [62] which can be expressed as

$$E_{max} \simeq Z\beta \cdot \left( \frac{B}{\mu G} \right) \cdot \left( \frac{R}{kpc} \right) 10^{18} eV \quad (1.7)$$

where  $Z$  is the cosmic ray charge,  $\beta$  is the velocity parameter of the shock wave. This relation is able to accelerate cosmic rays up to energies of  $10^{20}$  eV or higher.

The search for sources of cosmic rays is performed in two different ways: either directly by searching for correlations in the arrival direction of cosmic rays, or indirectly by looking for high energy neutrino or gamma ray emission that would reveal sites where high energy hadronic interactions are taking place. Their detection technique are briefly reported in the next chapter.

Direct detection is achieved especially at Ultra High Energies, above  $10^{19}$  eV, where the magnetic deflection experienced by charged cosmic rays propagating through the magnetic field of the galaxy is below a few degrees [38]. This is the goal of large air shower arrays like Telescope Array and the Pierre Auger Observatory. The down side to this detection technique is that, as was already mentioned, the fluxes are very low at ultra high energies.

High energy neutrino emission is expected as protons or nuclei interact with shock waves or other medium, producing mesons that subsequently decay in neutrinos. Since neutrinos experience no magnetic deflection they can point back to their sources, moreover their interaction probability is very small allowing them to propagate without absorption over cosmological distances. Their small cross section also represents a challenge to their detection, thus astrophysical neutrino detectors, like IceCube or KM3NET, require volumes of at least  $1 km^3$  to reach reasonable sensitivities [63].

Also gamma rays are produced in the decay of neutral pions should be accompanied the hadron interactions at the sources [64]. The pion decay signature can be overwhelmed by inverse Compton emission at the source which is purely leptonic in origin, but from the spectral characteristics of the gamma ray emission it is possible to determine if pion decays, and hence hadron acceleration, is taking place at the source. This kind of search is conducted in the GeV range with detectors as the Large Area Telescope on board the Fermi  $\gamma$  ray satellite [65], and in the TeV range using ground based Imaging Air Cerenkov Telescopes such as HESS, or MAGIC, etc. The recent discovery of hadronic emission from supernova remnants in our galaxy by

Fermi [66], in Figure 1.6, shows forcefulness for this search method.

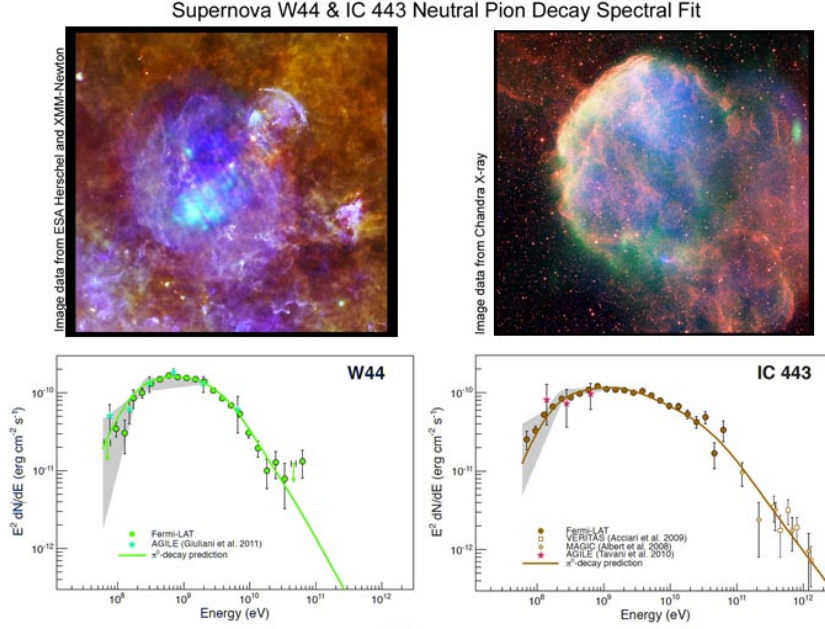


Figure 1.6:  $\gamma$  rays spectrum of the SNR W44 (*left*) and the SNR IC443 (*right*) observed by Fermi Large Area Telescope. The images of their X ray counterparts are also shown (Courtesy: NASA/DOE/Fermi LAT Collaboration, Chandra X-ray Observatory, ESA Herschel/XMM-Newton).

### 1.5.1 Galactic sources: Supernova Remnants

Supernova explosions in our galaxy produce powerful shocks capable of accelerating particles to energies below the knee. The possible connection between supernovae and cosmic rays was first suggested in 1934 by Baade and Zwicky [67], and further developed by Ginzburg and Syrovatskii [68]. As it is said, the energy density of Galactic cosmic rays in our galaxy is  $\rho_{CR} \sim 1eV/cm^3$ , considering a time of escape from the Galaxy of  $\sim 10^7 years$  1.6.1, the power needed to fill the galactic disk volume with cosmic rays is approximately [71]:

$$P_{CR} = \frac{\rho_{CR} V_G}{\tau_{esc}} = 5 \cdot 10^{33} J/s. \quad (1.8)$$

where:

$\rho_{CR} \sim 1eV/cm^3$  is the energy density of cosmic rays in our galaxy,

$V_G = 6 \cdot 10^{60} m^3$  is the galactic volume, assuming a galactic flat disk with a radius

of  $\sim 15 \text{ kpc}$  and a thickness of  $\sim 0.3 \text{ kpc}$ ,  
and  $\tau_{esc} \sim 10^7 \text{ years} = 3 \cdot 10^{14} \text{ s}$  is assumed.

During a core collapse, a supernovae can eject several solar masses ( $\sim 10 M_{\odot}$ ) of material with bulk velocities of around  $5 \cdot 10^7 \text{ m/s}$ . This corresponds to a total kinetic energy released of around  $3 \cdot 10^{35} \text{ J/s}$ , 99% in form of neutrinos and 1% in form of kinetic energy of expanding particles (shock wave). The supernova rate  $f_{SN}$  in a galaxy like our own is about 3 explosions per century, it means that the power delivered by all supernova is  $\sim 10^{34} \text{ J/s}$ . There are large uncertainties in this order-of-magnitude estimates, first of all the galactic volume which is 10 times bigger if the magnetic halo is considered. This means, that in order to obtain the observed energy density of cosmic rays, the energy emitted by supernova explosions has to be transformed into acceleration of the particles with an efficiency of only a few percent.

SNRs are important candidates for Galactic cosmic ray sources also for several reasons. The simplest one is that the chemical composition of the elements produced by core-collapse supernovae is very similar to the abundances of the cosmic rays because, in turn, it is similar to the Solar System. As it is said in section 1.4 in the relation 1.6, the particle gain in the first order Fermi's mechanism depends on the velocity of shock wave  $u_{sw}$ :

$$\eta = \frac{4}{3} \beta_M \quad \text{with} \quad \beta_M = \frac{u_{sw}}{c}. \quad (1.9)$$

$\eta$  can be considered the efficiency of energy transfer from the shock wave to the particle. Considering a supernova emitting materials of  $M \sim 10 M_{\odot}$  solar masses, The velocity of the ejected mass is:

$$u_{sw} \simeq \sqrt{\frac{E_K}{M}} = 5 \cdot 10^8 \text{ cm/s} \quad \text{therefore} \quad \beta_M \simeq 2 \cdot 10^{-2} \quad (1.10)$$

where  $E_K$  is the average energy emitted as kinetic energy.

This value of  $\eta$  corresponds to the needed efficiency required to explain the cosmic rays acceleration in supernovae explosion.

It is possible to express the maximum energy that a charged particle can reach in the acceleration process due to the diffusive shock mechanism from a supernova explosion [71]. The rate of energy increase is given by the ratio between the relation 1.9 and the characteristic period  $T_{cycle}$  of the process,

i.e. the time between two successive scattering processes:

$$\frac{dE}{dt} \simeq \frac{\eta E}{T_{cycle}} \quad \text{with} \quad T_{cycle} = \frac{r_l^{cycle}}{u_{sw}}. \quad (1.11)$$

where  $r_l^{cycle}$  is the typical extension of the confinement region, between two successive scattering, i.e. the Larmor radius for this region. Thus,

$$\frac{dE}{dt} \simeq \eta E \frac{u}{r_l^{cycle}} = \eta E \frac{ZeBu_{sw}}{r_l^{cycle}}, \quad (1.12)$$

Inserting the estimated values for the the thickness of a shock wave in a SNR and the time that a particle can spend in it, the maximum energy can be expressed from the relation 1.7:

$$E_{max} \simeq \frac{dE}{dt} T_{SNR} = \eta ZeBR_{SNR} = 300 Z \text{ TeV}, \quad (1.13)$$

This model explains the spectrum of cosmic-ray protons up to few hundreds of TeV which corresponds to the energy region where the knee begins: the transition between galactic and extragalactic cosmic rays.

The  $\gamma$  rays spectra of the galactic SNR W44 and SNR IC443, reported by the Fermi collaboration, are shown in Figure 1.6, the observations fit very neatly with predictions of neutral pion decays [61]. This represents a powerful evidence for hadronic acceleration in a SNR, although only for GeV protons.

## 1.5.2 Extragalactic sources

According to the Hillas criterion 1.7, acceleration sources for the most energetic cosmic rays have to provide a compensation between magnetic field and size so that the greatest energies can be reached.

Two classes of objects, Gamma Ray Bursts, GRBs, and AGN ,have for a long time been considered as the most likely candidates for the sources of UHECRs. If the composition near the GZK cutoff is heavy, as the Pierre Auger Observatory data seems to indicate, it is very unlikely that these cosmic rays could have come from GRBs.

GRBs should be characterized with  $r_l \sim 10^{-6}$  pc,  $B \sim 10^6$  G,  $E_{max} \sim 10^{20}$  eV, but they produce a huge number of MeV  $\gamma$  rays and any atomic nucleus that could remain in its vicinity long enough to be accelerated to UHEs

will most likely photo-disintegrate into its constituent protons and neutrons before escaping. In this models, photon-proton interactions in the GRB fireball should produce TeV neutrinos detectable by neutrino telescopes. A recent analysis of IceCube data shows no neutrino emission associated with GRBs, which heavily constraints neutrino emission models from GRBs and also their contribution to the cosmic ray flux near GZK energies [72].

AGN are galactic nuclei presumably hosting a black hole with a typical mass of  $M \simeq 10^7 - 10^8 M_{\odot}$ . They are characterized by jets with transverse dimensions of the order of a fraction of parsec, a Larmor radius  $r_l \sim 0.1$  pc and magnetic fields  $B \sim 1 \mu\text{G}$ , necessary to explain the synchrotron radiation from such objects. AGN could accelerate cosmic ray to  $E_{max} \sim 10^{20}$  eV. They are still considered potential sources of extragalactic cosmic rays, indeed recent studies presented a correlation between the arrival directions of UHECRs and nearby AGNs [73].

Since hadronic emissions are linked with harder  $\gamma$  ray spectra, it is expected

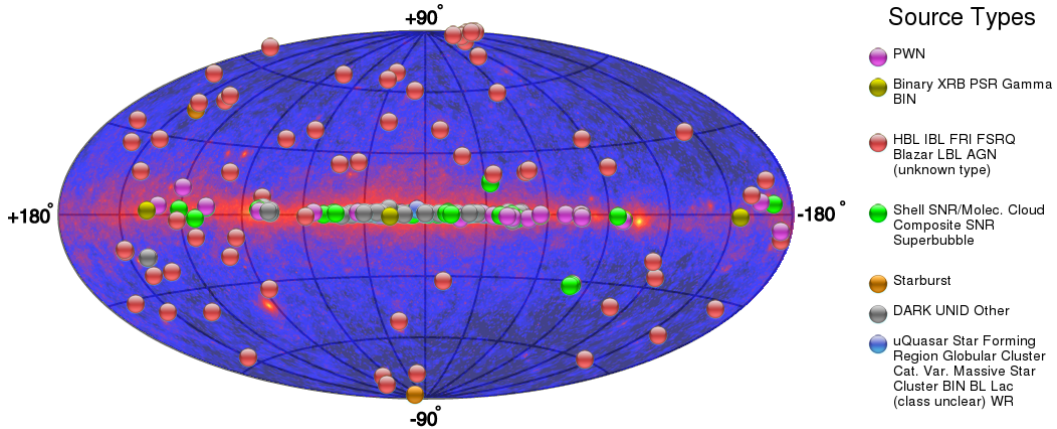


Figure 1.7: Sky map in Galactic coordinates of known sources of TeV  $\gamma$  rays included in TeVCat [74]. The legend indicates the type of source.

that sources with significant emission in TeV  $\gamma$  rays may be cosmic ray accelerators. The Milagro detector observed a significant number of extended  $\gamma$  ray emission regions distributed along the galactic plane, specially in the direction of the constellation Cygnus [69]. Imaging Air Cerenkov Telescopes such as MAGIC, HESS, etc, have identified a total of  $\simeq 150$  sources of TeV  $\gamma$  rays, attributable to galactic and extragalactic objects; a map of the sources catalog is showed in Figure 1.5.2, it is available through the TeVCat

website [74].

## 1.6 Propagation of the cosmic rays

The cosmic rays particle diffusively propagate over long distances from their sources to the earth. They interact with magnetic fields, dust, background photons, and other contents of the medium, and they carry information about the characteristics of the medium through which they have propagated. The propagation mechanisms of cosmic rays are as yet not fully known, but considering all the known phenomena, one can formulate propagation models, which aim to explain the cosmic ray propagation and their high isotropy.

### 1.6.1 Propagation of Galactic cosmic rays

Our galaxy, the Milky Way, is a vast collection of about  $10^{12}$  stars, dark matter, dust, and gas held together by gravity. The galaxy has a disc shape with a radius of about 15 kpc and a width of 300 pc, where solar system is located at a distance of about 8 kpc from the galaxy centre.

Measurements of starlight polarization, Zeeman splitting, and Faraday rotation indicate that the galaxy is permeated by a large-scale magnetic field with a strength of about  $2 \mu\text{G}$  oriented along the spiral arms. This component of the field is accompanied by a turbulent component of almost the same strength but with a shorter characteristic scale of the order of 10-100 pc. The energy density of the magnetic field is  $\sim 0.65 \text{ eV}/\text{cm}^3$ , which is comparable to the cosmic-ray energy density of  $1 \text{ eV}/\text{cm}^3$ . The magnetic field and the ionized gas of the galaxy form a magnetohydrodynamics (MHD) fluid through which the *Alfven* waves can propagate. They are a type of magnetohydrodynamic wave in which magnetic line tension provides the restoring force and the density of the ionized gas provides the inertia to the medium. On their travel, the particles also lose energy by collisions, decay and ionization processes, furthermore, particles can escape the galaxy and get lost. All these effects are causing a change in the spectral index of the energy spectrum from about  $\gamma \sim 2.0$  to  $\gamma \sim 2.7$ .

A significant part of our current knowledge of the propagation of cosmic rays in the galaxy comes from the study of their chemical abundances. Using spallation cross sections, it is possible to estimate the amount of matter

that primary cosmic rays need to traverse producing the observed secondary abundances. In particular, the ratio between boron and carbon (B/C) can be used as reference ratio since B is entirely secondary: Carbon, with Nitrogen and Oxygen are the major progenitors of Boron, and the production cross sections are better known than those of Beryllium and Lithium [75]. The measured B/C ratio from different experiments as a function of energy is shown in Figure 1.6.1.

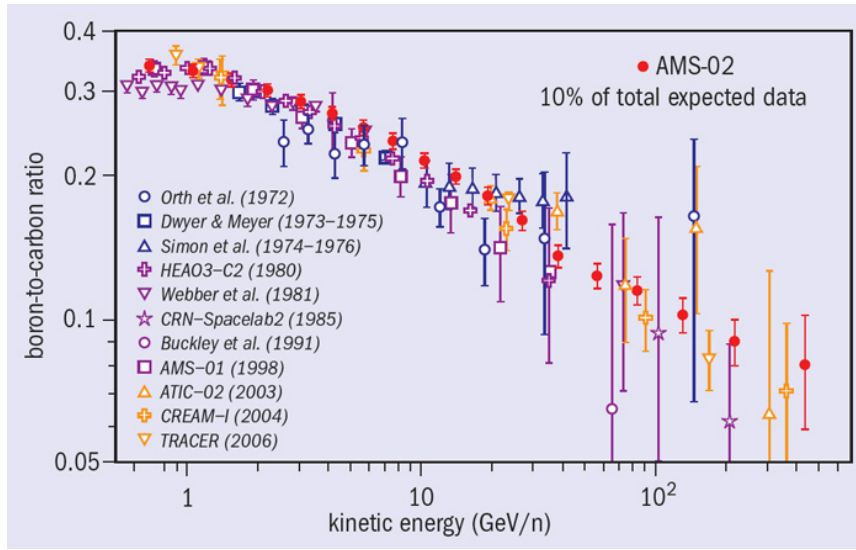


Figure 1.8: Observed Boron to Carbon abundance ratio, measured as a function of the kinetic energy per nucleon by different space and balloon experiments [76]. Previous results of other experiments are shown. The dashed line represents the result of a prediction with the leaky box model, assuming an energy-dependent escape path length [75].

At the energies starting up to  $\sim 1$  GeV/nucleon, the B/C ratio increases due to the dependence of the nuclear cross section on the relative velocity between nuclei; at higher energies, where the fragmentation nuclear cross-section is almost constant, the B/C ratio decreases. This is only a consequence of different path lengths for nuclei with different energies: a dependence of the path length on the particle rigidity  $R$  can be empirically assumed, thus particles with low rigidity suffer a larger deflection during the motion in a magnetic field because, according to 1.1, the Larmor radius is  $r_L = R/B$ . Therefore evolution of the *secondary to primary* (s-p) ratio with the energy confirms that UHE cosmic rays travel through less matter than low energy ones. Data indicates that, on average, a cosmic

ray travels through  $6 - 10 g/cm^2$  before reaching the top of the Earth's atmosphere. Since the column depth along the Galactic plane is of the order of  $10^{-3} g/cm^2$ , that Galactic cosmic rays have long confinement times (time of escape  $\tau_{esc}$ ) of several million years, during which the cosmic rays trajectories are scrambled by the Galactic magnetic field.

### 1.6.2 The transport equation

A realistic description of cosmic ray propagation was proposed by Ginzburg and Syrovatskii [68] where cosmic-ray transport is treated as a diffusion problem, that take account for the discrete nature of the sources, the gradients in the cosmic ray density across the galaxy, and for a model of the structure of the galaxy. The transport equation for a particle of type  $i$  can be written as:

$$\begin{aligned} \frac{\partial N_i}{\partial t} = & \nabla \cdot (D \nabla N_i) - \frac{\partial}{\partial E} [b_i(E) N_i(E)] - \nabla \cdot \mathbf{u} N_i(E) + Q_i(E) - p_i N_i(E) \\ & + \frac{v\rho}{m} \sum_{k \geq i} \int \frac{d\sigma_{i,k}(E, E')}{dE} N_k(E') dE' \end{aligned} \quad (1.14)$$

- ◇ In the first term corresponds to diffusion;  $D$  is the diffusion coefficient that can be expressed as a function of particle velocity  $v$  and diffusion mean free path  $\lambda_D$ , as:

$$D = \frac{1}{3} \lambda_D v$$

Typical values for  $D$  are obtained by fitting cosmic ray data such as the Boron to Carbon (B/C) ratio. At an energy of  $\sim 1 \text{ GeV/nucleon}$ ,  $D$  is  $\sim (3 - 5) 10^{28} \text{ cm}^2/s$ , and increases with magnetic rigidity  $R$  as  $R \sim (0.3 - 0.5)$  for different diffusion models [75].

- ◇ The second term where  $b_i(E) = dE/dt$ , represents the variation in energy of the particles during propagation, either losses through ionization or gains through reacceleration.
- ◇ The third term is the convection term, characterized by the convection velocity  $v$ , or Galactic wind, which corresponds to the bulk motion of the cosmic ray plasma. The convection may be important since Galactic winds have been observed in other galaxies and could be relevant at large distances from the disk as the wind speed increases. In order to agree with s-p ratios and anisotropy measurements, one model divides the galaxy in two zones: one at vertical distances  $< 1 \text{ kpc}$  from the disk with pure diffusion, and a second one with a mix of diffusion and convection at larger distances. A characteristic value of the convection velocity is  $20 \text{ km s}^{-1}$ .

- ◇ The fourth term is the source term  $Q_i(x, E, t)$ , where a cosmic ray source, located at position  $x$ , injects particles of type  $i$  with energy  $E$  at time  $t$  into the medium. This source term is zero for secondary nuclei.
- ◇ The fifth term represents the loss of particles of type  $i$  through decay or collisions,  $p_i$  can be written as:

$$p_i = \frac{v\rho\sigma_i}{m} + \frac{1}{\gamma\tau_i}$$

where  $\lambda_i$  is the mean free path for collisions in a medium with density  $\rho$  and  $\gamma\tau_i$ ,  $\gamma$  the Lorentz factor and  $\tau_i$  is the lifetime of the nucleus.

- ◇ The last term take into account the disappearance by radioactive decay of the nuclei  $i$  and respectively the apparition of the nuclei  $j$  via radioactive decay of the species  $i$  from spallation processes, the feed-down production, where  $\sigma_{i,k}$  is the energy dependent spallation cross section.

The propagation of cosmic rays could be much more complex as the “simple” diffusion model: charged particles interact with magnetohydrodynamic waves reaccelerating. There exist two arguments which lead to consider a reacceleration of cosmic ray particles the first one, the magnetic field inhomogeneities conduct naturally to an energy gain by Alfvén waves, the second one, the ratio of s-p nuclei falling rapidly with increasing energy favors a reacceleration.

Resolving the diffusion equation 1.14 requires the complete analysis of a system of coupled equations where all the parameters are well known: the form and the size of the propagation region of cosmic rays, as well as the distribution of the interstellar gas and of the sources. We do not have all the information for resolving the equation system, but there exist models, approximating the solution with some assumptions. Solutions to the diffusion equation can be found analytically by assuming symmetries in the geometry of the halo, the distribution of sources or by setting boundaries conditions; whereas several software packages exist that find numerical solutions, such as GALPROP, the most widely used one [77], and DRAGON for UHE cosmic rays [78].

### Leaky Box approximation

The Leaky Box model [79], introduced in the 60th, is as an extremely simplified version of the diffusion model, in which we assume that diffusion takes

places rather rapidly: the distribution of cosmic rays in the whole box (i.e. Galaxy) is homogeneous and in contrary it is necessary to allow a certain escape time  $\tau_{esc}$  of cosmic rays from the system. In the equation 1.14, the diffusion term is substituted with:

$$\nabla \cdot (D\nabla N_i) \longrightarrow -\frac{N_i}{\tau_{esc}}$$

For every quantity the average value is used: the cosmic ray spends a mean time  $\bar{\tau}_{esc}$  in the volume and traverses a mean amount of matter  $\bar{\chi}_{esc} = \bar{\rho}\beta c\bar{\tau}_{esc}$ , the particle is moving with a velocity  $u = \beta c$  through the interstellar medium (ISM) of density  $\bar{\rho}$ .

Gaisser [80] analyses the case of sources where particles are injected instantaneously at time  $t_0$  with energy spectrum  $N_0(E)$ . The observed spectrum in the Leaky Box model will be:

$$N(E, t) = N_0(E) \exp(\bar{\tau}_{esc} - t) \quad (1.15)$$

Neglecting energy losses and gains, the transport equation for cosmic rays of species  $i$  can be written as:

$$\frac{N_i(E)}{\bar{\tau}_{esc}(E)} = Q_i(E) - \left( \frac{\beta c \rho}{\lambda_i} + \frac{1}{\gamma \tau_i} \right) + \frac{\beta c \rho}{m} \sum_{k>i} \sigma_{i,k} N_k(E), \quad (1.16)$$

where  $\sigma_{i,k}$  is the spallation cross section for the production of secondaries of species  $i$  from heavier nuclei of species  $k$ ,

and  $\gamma \tau_i$  is the Lorentz dilated lifetime of the nucleus.

For protons, where  $\lambda_p \simeq 55g/cm^2$ ,  $\lambda_{esc} \ll \lambda_p$ , the equation is:

$$N_p(E) \simeq Q_p(E) \bar{\tau}_{esc}(R). \quad (1.17)$$

$R$  is the rigidity in GV.

From the s-p ratio the escape time should be  $\tau_{esc} \propto R^{-\delta}$ , or similarly,  $\tau_{esc} \propto E^{-\delta}$ , where  $\delta = 0,6$ . The spectrum observed at Earth is known to be a power law as  $N_P \propto E^{\gamma+1}$ . The source spectrum may also be written as a power law with spectral index  $\alpha$ , so that  $Q_p(E) \propto E^{-\alpha}$ . Replacing the power law spectra and the energy dependence of the containment time into the relation 1.17, the index must satisfy  $\alpha = (\gamma + 1 - \delta)$ . The cosmic ray index observed at Earth is  $\gamma = 2,7$ , which means that the spectral index at the source should be  $\alpha \simeq 2,1$ , which is in good agreement with the expected

spectrum for acceleration in astrophysical shocks discussed in section 1.4.

Therefore the Leaky Box model permits a direct analysis of flux measurements in function of only three parameters: the escape time, the mean matter density and the abundance sources, and even though this simple model is only an approximation without indication of the many physical processes, it is able to reproduce some important propagation observables.

### 1.6.3 Propagation of Extragalactic cosmic rays

Cosmic rays with energies above  $10^{18}$  eV cannot be contained by the magnetic field of the galaxy and can propagate over intergalactic distances. If their energy is large enough to reach, in the centre of mass system, the resonant production of the  $\Delta^+$ , they losses energy due to the GZK effect, which reduces their mean free path to a few tens of Mpc. Since in intergalactic space the magnetic field intensities are expected to be much lower than in the Galaxy,  $B < 10^{-9} G$ , the trajectories of UHE cosmic rays are less deflected and they can be used to search for cosmic rays sources as they point back to their origin. Once entered the Galaxy UHE particles feel feeble influence from magnetic fields. The deflection angle  $\Theta$  of a particle of energy  $E$  moving in a direction perpendicular to a uniform magnetic field  $B$  after traveling the distance  $d$  is:

$$\Theta \sim \frac{d}{r_l} \simeq 0.5^\circ Z \left( \frac{10^{10} \text{eV}}{E} \right) \left( \frac{d}{\text{kpc}} \right) \left( \frac{B}{\mu\text{G}} \right) \quad (1.18)$$

Therefore a small deflection of  $\sim 1^\circ - 5^\circ$  is expected for proton of energy  $5 \cdot 10^{19}$  eV [81]. This result motivates the search for extragalactic sources of UHE cosmic rays since galactic sources would produce a clear anisotropy on Earth measurements, especially for protons and light nuclei that is not observed.

## 1.7 Diffusion in the Solar System

The Sun is the main source of cosmic rays of energy below  $\sim 4$  GeV. Cosmic rays originated from the Sun were first observed in the early 1940s, and consist of protons, electrons, and heavy ions with energy ranging from a few keV to few GeV. They are originated by solar wind, flares and powerful coronal mass ejections (CMEs). A solar flare is a sudden brightening observed over the Sun's surface, it occurs in active regions around sunspots where intense

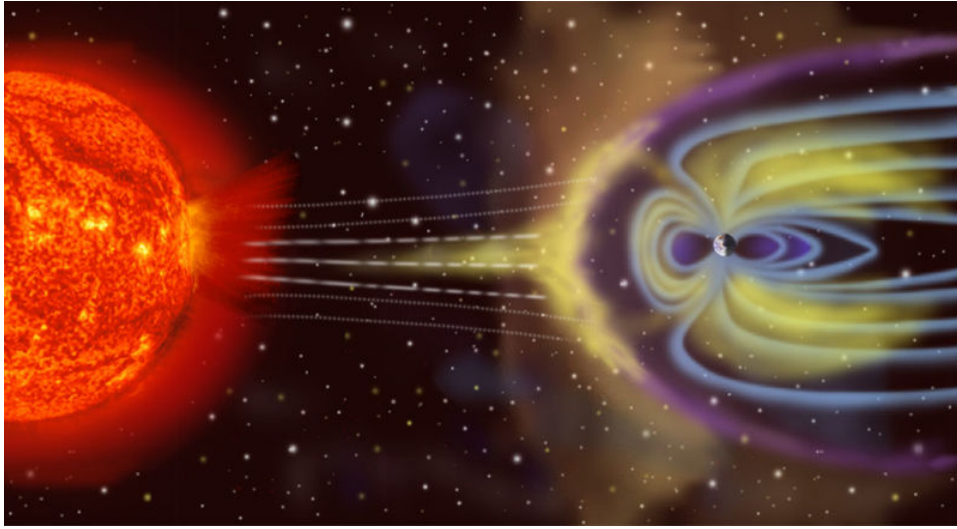


Figure 1.9: An artistic picture of the interaction of the solar wind with the Earth's magnetosphere. Sizes are not to scale.

magnetic fields penetrate the photosphere to link the corona to the solar interior. It is often, but not always, accompanied by a CME. A CME is a significant release of plasma, and therefore magnetic field from the solar corona, it can be observed in coronagraph imagery. Most solar flares and coronal mass ejections originate in magnetically active regions around visible groupings of sunspots. In 1937, Forbush realized that a significant  $\sim 5\%$  decrease of the cosmic-ray intensity correlated with these sudden increasing of the solar activity. The **Active Sun** phenomena appear to strongly increase the solar wind which also consists of charged particles. The high energy particles, emitted in a flare, generates a magnetic field in addition to the Interstellar Magnetic Field from the **Quiet Sun's** field.

The intensity of low energy cosmic rays at Earth is historically observed and measured through detectors based on ground: the neutron monitors. Neutron monitors are designed to measure neutrons (but they detect also protons, etc) produced by the interactions of cosmic rays with the atmospheric nuclei in the Extensive Atmospheric Shower. If the primary cosmic ray that started the cascade has energy over  $\sim 500$  MeV, some of its secondary products, including neutrons, will reach ground level. In Figure 1.7 a typical galactic cosmic rays decrease correlated with a flare is presented. The muon decrease, observed in 5 muon telescopes of the EEE Project is

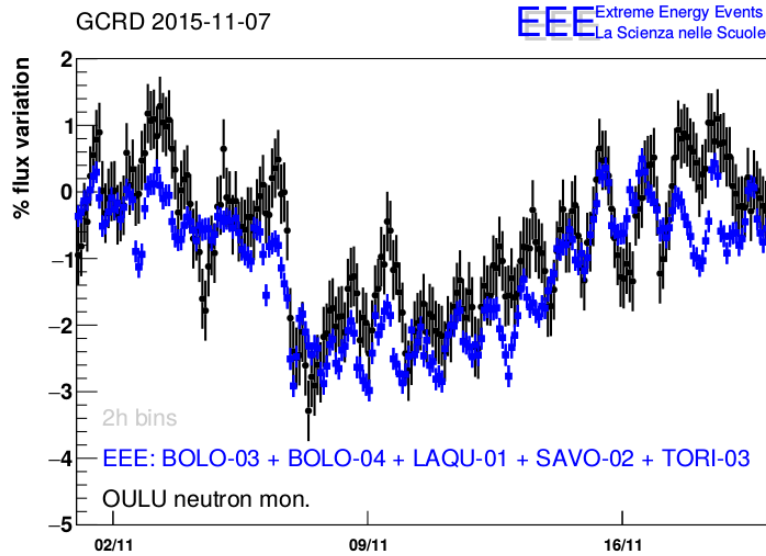


Figure 1.10: GCRD on the date 07-11-2015, muon decreases observed with 5 EEE telescopes, compared to neutron rate from the Oulu station.

compared with Neutron Monitor observations from the Oulu station, see section 3.6.2.

The Quiet Sun activity influences also the probability that cosmic rays with energy below few GeV reach the Earth. When cosmic rays enter our solar system, they must overcome the outward-flowing interplanetary medium also called the solar wind. This *wind* is a stream of charged particles continuously released from the upper atmosphere of the Sun.

In the 1950s, a German scientist named Ludwig Biermann became interested in the fact that no matter whether a comet is headed towards or away from the Sun, its tail always points away from the Sun. Biermann postulated that this happens because the Sun emits a steady stream of particles that pushes the comet's tail away. In fact a fully ionized gas, thus a plasma, basically constituted of protons, electrons and alpha particles, is pushed radially out of the Sun's corona. embedded within the Interplanetary Magnetic Field. Once the plasma has left the solar corona, the dynamic pressure of the wind dominates over the magnetic pressure through most of the solar system, so that the magnetic field is pulled into a complex structure, the Parker spiral, by the combination of the outward motion and the differential rotation of the Sun [85]. It follow an Archimedean spiral pattern, changing in density, temperature and speed over time and over solar latitude and

longitude. At a distance of more than a few solar radii from the Sun, the solar wind is supersonic and reaches speeds of 250 to 750 km/s, with an energy between 1.5 keV and 10 keV.

The flux of galactic cosmic ray nuclei with energies below  $\sim 1$  GeV/nucleon is strongly modulated by their interaction with the magnetic field carried by the expanding solar wind (Figure 1.7). The expanding magnetized plasma generated by the Sun decelerates and partially excludes the lower energy particles from the inner solar system. Consequently the low energy component of the cosmic ray flux undergoes a sizable variation over the solar cycle: this effect is known as *solar modulation*. This influence can be calculated by an equation based on a convection-diffusion model [82]:

$$r^2 \frac{\partial U}{\partial t} = -\frac{\partial}{\partial r}(r^2 V U) + \frac{\partial}{\partial r^2} \left( r^2 \kappa \frac{\partial U}{\partial r} \right) + \frac{1}{3} \left[ \frac{\partial}{\partial r}(r^2 V) \right] \left[ \frac{\partial}{\partial E_T}(\alpha E_T U) \right] \quad (1.19)$$

where  $E_T$  the kinetic energy and  $m$  the mass of the considered cosmic particle,

$V(r, t)$  is the solar wind speed and  $\kappa$  the diffusion coefficient,

$$\alpha = \frac{E_T + 2mc^2}{E_T + mc^2},$$

$U(r, E_T)$  is the differential density,  $r$  the radial distance from the Sun.

The equation describes the effects of convection (first term) and scattering of cosmic-ray particles by magnetic scattering centers (second term) carried along by a radially moving solar wind, with the assumption of spherical symmetry. The third term describes the adiabatic expansion.

The magnetic activity and the solar modulations are monitored mainly through sunspots, by the Wolf number or Sunspot Number (SSN), or the tilt angle of the Heliospheric Current Sheet [83]. They follow a 22 years cycle which consist of two epochs of 11 years, each of negative and positive polarities of the heliospheric magnetic field from the north polar region of the Sun.

The Neutron monitor measurements are anticorrelated with the level of solar activity, i.e., when solar activity is high many sunspots are visible, the cosmic ray intensity at Earth is low, and vice versa. Figure 1.11 shows the correlation between the SSN and the number of neutrons detected at ground.

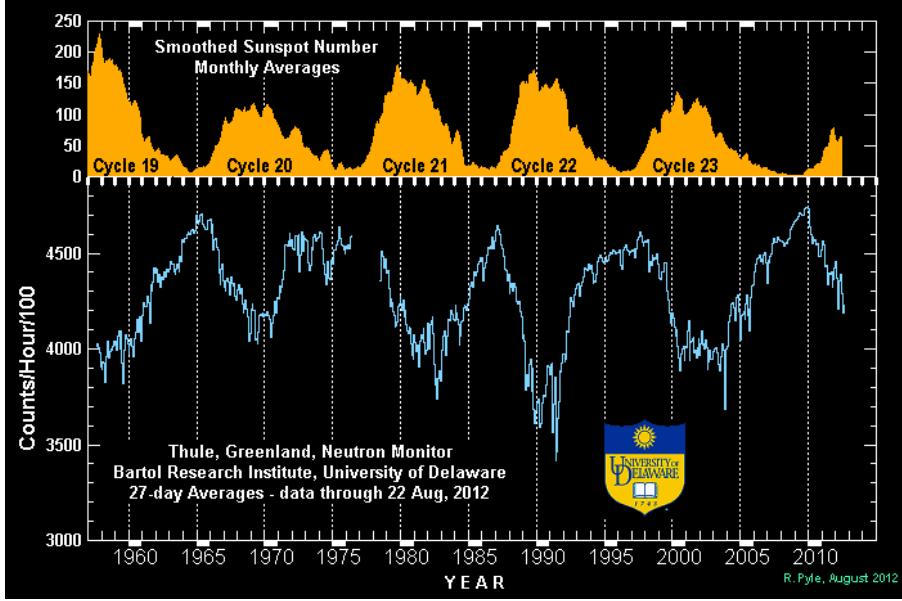


Figure 1.11: The solar modulation during the last 5 solar cycles [86]. The rate of the neutron monitor (bottom of the figure) is correlated the sunspot number (on the top). The neutron rate is measured at the Thule station.

### 1.7.1 The solar Force Field approximation

One method to resolve equation 1.19 is the approximation of a force field, as an analogy to a radial electric field with a potential  $\phi$ . In this approximation the equation of density evolution is:

$$\kappa \frac{\partial U}{\partial t} = -\frac{V}{3} (E_T^2 - m^2 c^4)^{3/2} \frac{\partial U}{\partial (E_T)} \left[ \frac{U}{E_T (E_T^2 - (mc^2)^2)^{1/2}} \right]. \quad (1.20)$$

Integrating the equation, an asymptotic solution at high energies can be obtained. With the application of the boundary conditions the cosmic flux can be written as  $J(E) = vU(E)/4\pi$ , and the variation of the cosmic rays flux can be expressed as follows:

$$J_{mod}(E) = \frac{E^2 - m^2 c^4}{(E + Ze\phi)^2 - m^2 c^4} J(E + Ze\phi), \quad (1.21)$$

where  $Z$  is the particle charge in units of electric charge  $e$ , and  $\phi$  is the **solar potential**.

The solar potential  $\phi$  depends on the solar wind velocity  $V$ , on the radial diffusion coefficient  $k = \frac{\kappa}{\beta R}$ , where the rigidity  $R = \frac{pc}{Ze}$ , on the modulation

boundary  $r_b$  (the influence zone of the solar wind).

$\phi$  is given by the equation:

$$\phi(r, t) = \int_r^{r_b} \frac{V}{3k} dx = \frac{V(r_b - r)}{3k}. \quad (1.22)$$

We can give some values of the different parameters:

$k$  depends on the solar period

$r_b = 100 \text{ AU}$

$V \sim 400 \text{ km / s}$

$R \sim 1 \text{ GV}$

$\phi \sim 250 - 750 \text{ MV}$  for the solar minimum and maximum, respectively.

The solar modulated cosmic ray flux is better called *the Top of Atmosphere flux*, which is an individual element of cosmic rays spectra. It is, in fact, measured on the top of the Earth's atmosphere, this does not correspond to the interstellar cosmic ray flux. Experiments, detecting cosmic rays, have to consider the solar modulation to obtain the flux of interstellar cosmic rays. The interstellar cosmic ray fluxes above 10 GeV/n in a simple approximation can be written as [88]:

$$F(E) \simeq \phi \left( \frac{E}{\text{TeV}} \right)^{-\gamma} (\text{m}^2 \text{s sr TeV})^{-1} \quad (1.23)$$

The correlation of the cosmic ray flux for energies below few GeV with the solar phase is clearly visible in Figure 1.12. Here, the flux of protons as measured by the Bess experiment [87] in several different years is shown. A higher proton flux at energies below few GeV is evident during 1997, when the number of monthly sunspots in Figure 1.11 was at the minimum, whereas the variation of the solar activity does not affect cosmic particles with energy larger than few GeV.

## 1.8 Effect of the Geomagnetic Field

The Earth magnetic field is an offset dipole field where the South magnetic pole is actually located in the Northern hemisphere at latitude  $81^\circ N$  and longitude  $84.7^\circ W$ . and the North magnetic pole is close to the South rotational pole, To reach the top of the atmosphere, charged particles and nuclei below the GeV range are guided by the Geomagnetic field, thus the intensity of the low energy component of the cosmic radiation depends both

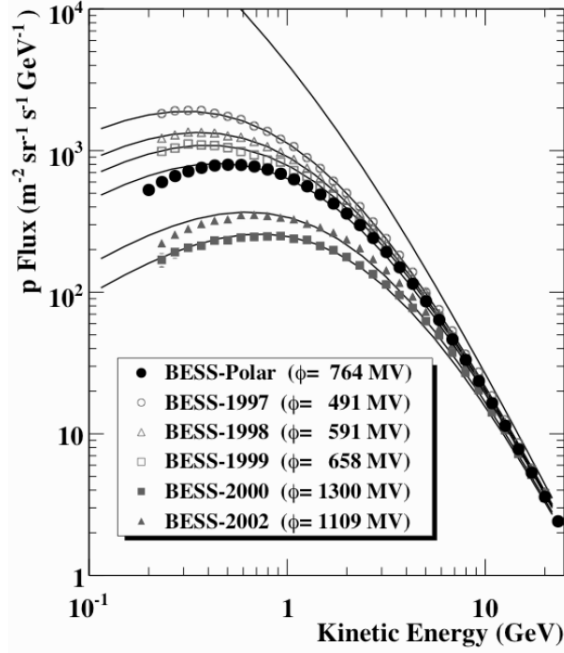


Figure 1.12: The yearly proton energy spectrum measured by the BESS experiment from 1997 till end of 2004.

on the location and time. Moreover for certain magnetic field configurations, there exist regions of space for which the arrival of particles below an energy threshold is forbidden. Around the 1920s Stormer showed the existence of a shielded region for the Earth dipole field configuration [13].

A simple condition which is necessary for a particle to reach the Earth atmosphere is that all trajectories starting from the point considered on Earth, reversing the charge of the particle, reach  $r \rightarrow \infty$ . At low enough energies trajectories can be deflected back to the Earth (or can remain at a finite distance): a cutoff value of the magnetic rigidity  $R$  exists for a particle to be able to reach the Earth, see Figure 1.13 . In a simplified model:

$$B(r, \lambda_B) = \frac{B_0}{(r/r_\oplus)^3} \sqrt{1 + 3\sin^2 \lambda_B} \quad (1.24)$$

where:  $B_0 \sim 0.31$  gauss, the mean value of the geomagnetic field on ground level,  $\lambda$  the geomagnetic latitude,

$r$  is the distance from the centre of the Earth and  $r_\oplus$  the Earth's radius.

The rigidity cutoff  $R$  was calculated analytically by Stormer, for a particle

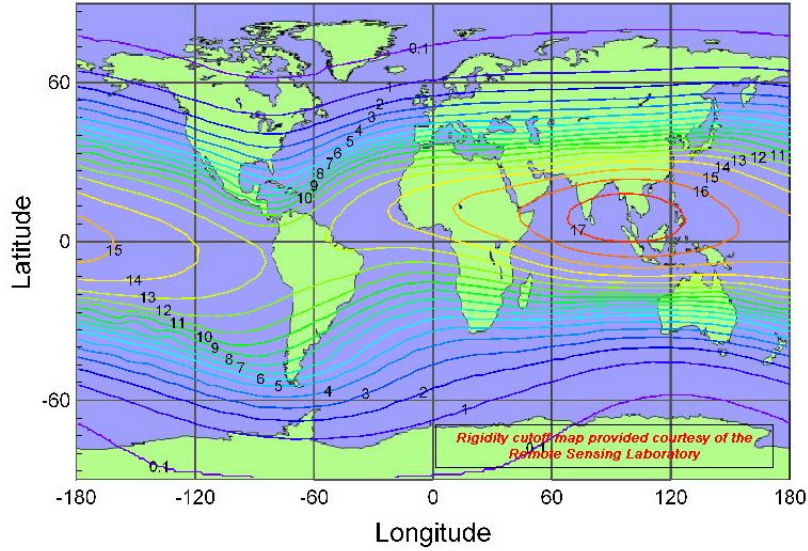


Figure 1.13: Map of the variation of Rigidity cutoff for the different latitude [90]

of charge  $e$  and mass  $m$ , it is:

$$R_s(r, \lambda_B, \theta, \psi_B) = \frac{m}{2r^2} \frac{\cos^4 \lambda}{[1 + (1 - \cos^3 \lambda_B \sin \psi_B)^{1/2}]^2}, \quad (1.25)$$

where:  $\theta$  is the particle zenith angle,

$\psi_B$  the azimuthal angle measured clockwise from the North magnetic pole.

Primary cosmic rays with energy below  $\sim 60$  GeV are influenced by the Earth magnetic field which induces anisotropies in the observed flux, *the latitude effect* [89]. The equation 1.25 includes also the *East-West effect*: low energy cosmic rays from the East are suppressed compared to those from the West. This East-West effect was first observed in the 1930s and was used to infer that the sign charge of most of the primary cosmic rays is positive.

The Earth dipole-like magnetic field induces also another relevant effect known as *the Van Allen radiation belts*, from its discoverer, J. Van Allen. They are two torus shaped layers of energetic charged particles around the Earth, located in the inner region of the magnetosphere, and held in place by the magnetic field [90]. The outer belt consists mainly of energetic electrons, while the inner belt is formed by a combination of protons and electrons, they are shown in Figure 1.14. The belt extends from an altitude of about

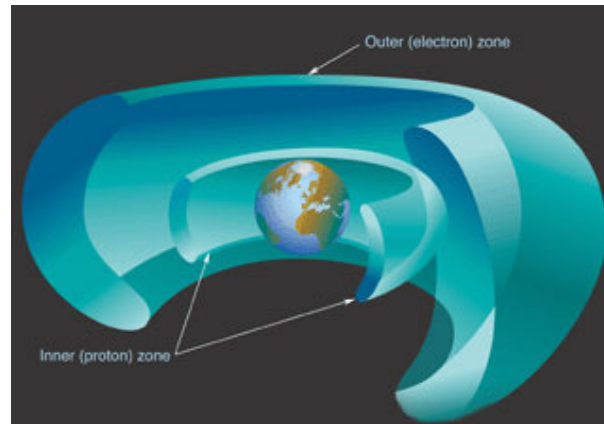


Figure 1.14: *Sketch of the van Allen radiation belts*

1-60  $10^3$  km above the surface. Due to the irregularity of the Geomagnetic centre, in the South Atlantic Ocean the inner belt comes very close to the Earth's surface, dipping down to an altitude of 200 km. This is called *the South Atlantic Anomaly*, where the flux of energetic particles is very high and the orbiting satellites are exposed to higher than usual levels of radiation.

## 1.9 Extensive air showers

When cosmic rays enter the Earth's atmosphere they collide with atoms and molecules, mainly oxygen and nitrogen. The interaction produces a cascade of lighter particles, a so-called air shower secondary radiation that rains down, including x-rays, muons, protons,  $\alpha$  particles, pions, kaons, electrons, neutrons. Thus the cosmic rays composition changes dramatically during their propagation through the atmosphere: while above the atmosphere, protons and helium nuclei dominate the flux, the sea level flux is mostly composed by neutrinos and muons. Most of the produced particles stay within about one degree of the primary particle's path. *Secondary particles* are generated by the interaction of cosmic particles with nuclei and electrons in the upper atmosphere, which leads to an Extensive Air Shower (EAS). The existence of air showers was discovered by P. Auger in 1939 [11].

In a *hadronic* extensive air shower, which is initiated by a hadronic interaction of the primary particle with an air nucleus, the inelastic cross-section of the reaction defines the interaction length for the primary particle

in the atmosphere. The interaction length, or mean free path, for a nucleus of  $i$ -species in the air is given by [80]:

$$\lambda_j = \frac{\rho}{\rho_j \sigma_j^{air}} = \frac{A_j m_p}{\sigma_j^{air}}, \quad (1.26)$$

where  $\rho$  is the atmospheric density,  $\rho_j$  is the nucleon density,  $\sigma_j^{air}$  is the nucleon-air interaction cross section that depends on the energy of the primary particle,  $A_j$  is the nucleus mass number and  $m_p$  is the nucleon mass.

Therefore the interaction probability of a primary particle with an atmospheric nucleus depends on the cross-section and the density of the atmosphere. For particle in the GeV energy range,  $\lambda$  is about  $90 \text{ g/cm}^2$  for protons and  $50 \text{ g/cm}^2$  for helium nuclei, which is a small number if compared to the atmospheric depth. The vertical intensity of the primary cosmic rays can be expressed as:

$$N(E, X) = N(E, 0)e^{-X/\lambda}, \quad (1.27)$$

where  $X$  is the atmospheric depth or column density in  $\text{g/cm}^2$ , traversed since the *top* of the atmosphere ( $\sim 100 \text{ km}$  of altitude).

For a certain primary energy, the height of the first interaction above ground level is not fixed and varies due to the probability distribution of the interaction process. This leads to large fluctuations in the shower development. The development of extensive air showers is characterized by two processes, the production of particles by interaction and the decay of particles. Basically, an air shower comprises of three different classes of secondary particles, a *nucleonic component* containing nucleons or light nuclei created by spallation with the air nuclei, a *hard component* generated by the decay of mesons into muons, and a *soft component* which includes electromagnetically interacting photons and electrons, Figure 1.15 shows schematic view of a EAS main components.

### 1.9.1 The nucleonic component

Only about 1 % of the total number of particles in an air shower is due to hadrons. Nevertheless, the hadronic component has a large impact on the shower development, because it feeds the other shower components.

In the initial collision of the primary particle with an air nucleus, the

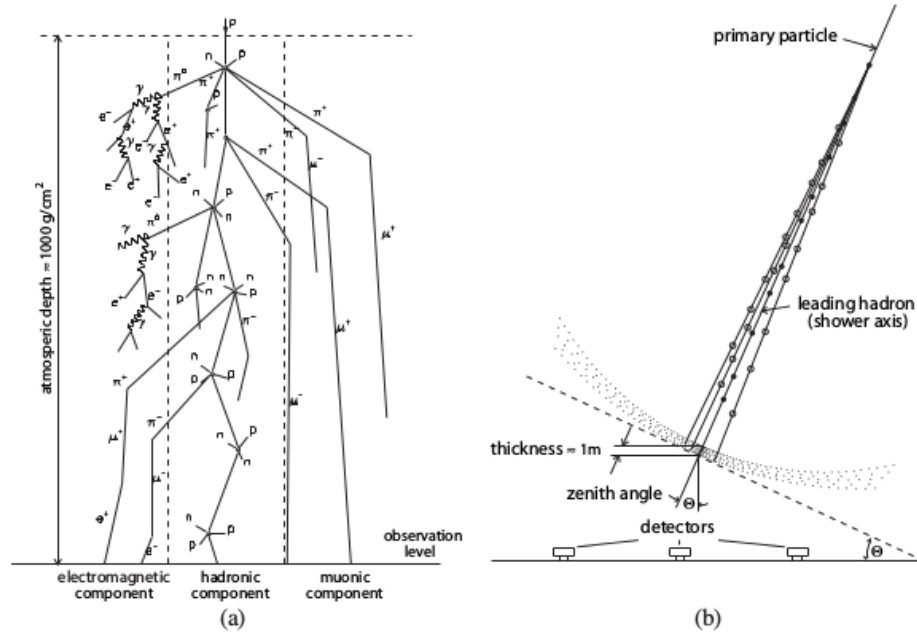


Figure 1.15: Schematic view of the development of an extensive air shower. In the left figure, the different components and their origin are illustrated. In the right figure, the geometry of an extensive air shower is shown.

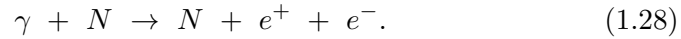
first generation of secondary particles is created in a strong interaction. These secondaries may decay or interact with other air nuclei producing a further generation of secondaries, which in turn may decay or interact again. While the shower propagates towards ground level, these processes occur repeatedly. This leads to a nucleonic cascade with an increasing number of hadrons as the atmospheric depth increases.

During the development of the cascade, the secondaries of each new generation carry less energy per particle. Thus, it becomes more likely for the hadrons to decay than to interact, they also experience energy losses due to ionization in the gas. Therefore, the number of hadrons in a cascade reaches a maximum, afterwards it decreases exponentially. The atmosphere corresponds to about 11 hadronic interaction lengths, thus, the initial primary particle will not reach sea level. The secondary hadronic particles consist mainly of neutral and charged pions  $\pi$ , followed by kaons  $k$ , protons and neutrons. The mean transverse momentum of the secondary hadrons is about 400 MeV, which is small compared to the overall momentum. Thus, the nucleonic component forms a narrow shower with a maximum spread of about 20 m, which propagates along the line of flight of the initial primary

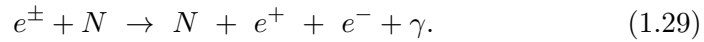
particle. This line represents the shower axis, as shown in Figure 1.15 for an illustration. For hadrons at low energies ( $E < 10$  GeV), especially neutrons, the transverse momentum can not be neglected in comparison to the longitudinal momenta, which leads to a broad distribution of these particles of up to 1 km.

### 1.9.2 The electromagnetic component

The electromagnetic component is fed by the hadronic component of the extensive air shower. Neutral pions decay into two photons, each initiating an electromagnetic cascade. The photons generate electron-positron pairs by the reaction:



The electrons and positrons generate further photons via bremsstrahlung:



Both processes feed each other, which develops to an electromagnetic sub-cascade of the air shower. Additionally, neutral pions are generated continuously along the shower axis. Each of these pions is the starting point of a new electromagnetic cascade. The superposition of the cascades determines the longitudinal development of the number of electromagnetic particles, which multiplies in such a way, that they become the most numerous particles in an air shower. The longitudinal development of a photon-induced shower can be described by [96]:

$$N_e(E_0, t) = \frac{0.31}{\sqrt{\beta_0}} \cdot e^{t(1-1.5t/s)}, \quad (1.30)$$

with:

$$t = \frac{X}{X_0}, \quad \beta_0 = \ln \frac{E_0}{E_{crit}}, \quad \text{and} \quad s = \frac{3t}{t + 2\beta_0} \quad (1.31)$$

where  $t$  is the atmospheric depth measured in units of the radiation length  $X_0$ , which is  $37.15 \text{ g/cm}^2$  in air,

$E_0$  and  $\beta_0$  are the energy and  $\beta$  of the initiating photon,

$s$  is the *longitudinal shower age*, an age parameter which describes the shower development.

At the beginning of the shower  $s$  is equal zero and at the maximum of the shower the parameter becomes one. Thus, for  $s > 1$  the number of particles

decreases. The Critical Energy, the energy at which the energy loss rates due to ionization and due to bremsstrahlung are equal, corresponds in air to  $E_{crit} = 84.2 \text{ MeV}$ . The lateral spread of an electromagnetic shower is caused by Coulomb scattering, it can be described by the NKG function, named after J. Nishimura, K. Kamata, and K. Greisen [96] [97]:

$$\rho_e(r) = \frac{\Gamma(4.5 - s)}{\Gamma(s)\Gamma(4.5 - 2s)} \frac{N_e}{2\pi r^2} \left(\frac{r}{r_M}\right)^{s-2} \left(1 + \frac{r}{r_M}\right)^{s-4.5}, \quad (1.32)$$

with the electron density  $\rho_e$  at the distance  $r$  from the shower axis,  $N_e$  the total number of electrons at observation level, and the Moliere radius  $r_M$ , which is  $r_M = 79 \text{ m}$  at sea level.

The NKG function is valid for purely electromagnetic showers. If the extensive air showers are initiated by hadrons, they lead to several electromagnetic sub-cascades, which superimpose, then the NKG function not describe such showers. Nevertheless, with different parameters it can still be used to approximate the lateral development of the electromagnetic component.

The longitudinal development of electrons shows a pronounced maximum. This is due to the fact, that electrons interact in the atmosphere and get lost. So, the number of electrons measured at ground depends on the altitude.

The position of the maximum of the number of electrons, the shower maximum  $X_{max}$ , depends on the type of the primary particle. The shower maximum depends only weakly on the primary energy, whereas proton induced showers have their maximum deeper in the atmosphere compared to iron induced showers. Therefore, the position of the shower maximum is a measure of the type of the primary particle. and it is utilized by the measurement of air showers using fluorescence detectors, like in Auger or Fly's Eye.

### 1.9.3 The muonic component

The muonic component accounts for 5% of the total number of particles in an extensive air shower. The muons are mainly generated by the decay of charged pions ( $\sim 100\%$ ) and kaons( $\sim 63.5\%$ ) [91] :

$$\pi^+ \rightarrow \mu^+ + \nu_\mu \quad e \quad \pi^- \rightarrow \mu^- + \bar{\nu}_\mu .$$

with decay time  $\tau \sim 2,6 \cdot 10^{-8} \text{ s}$ , and

$$k^\pm \rightarrow \pi^\pm + \pi^0 \quad k^\pm \rightarrow \pi^\pm + \pi^\pm + \pi^\mp \quad k^\pm \rightarrow \mu^\pm + \nu_\mu^\mp$$

with  $\tau \sim 1,2 \cdot 10^{-8}$  s.

The produced muons take on the average 79% and 52% of the energy of the

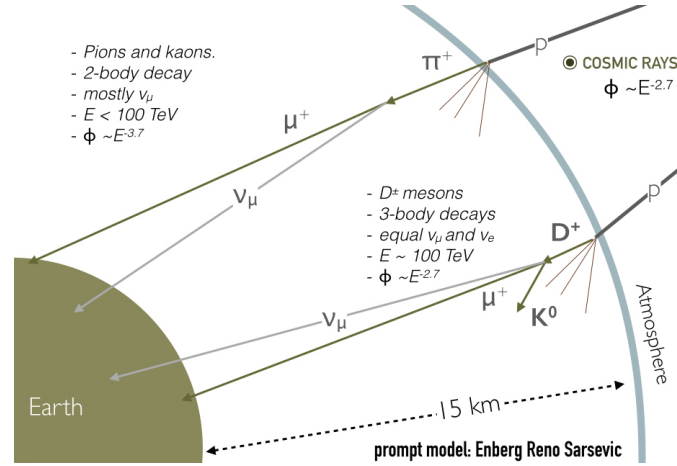


Figure 1.16: Schematic view of the muonic production in Atmosphere.

$\pi^\pm$  and  $k^\pm$ , respectively. The contribution of  $k$ -decays to muon production is a function of the energy and ranges from 5% at low energies to an asymptotic value of 27% for  $E > 1$  TeV. At very high energies a small contribution arises from the charmed particles ( $D^+$  tree body decay). A schematic view is reported in Figure 1.16.

The flux of cosmic rays at sea level is dominated by neutrinos and muons, which point the same incoming direction of the parent meson, therefore within a few degrees, of the primary cosmic rays:

- ◇ The density of the atmosphere decreases exponentially with the height, thus the possibility of an interaction of a meson with an air nucleus increases with decreasing height. Only at large heights the mesons can decay before they interact. The peak of the pions intensity curve is around at an altitude of 15 km. Therefore most of the muons are generated high in the atmosphere, which in turn means, that they are generated at an early stage of the shower development.
- ◇ Muons are mainly emitted in the direction of the line of flight of the parent mesons. Therefore, the lateral distribution of the muons is mainly caused by the momenta of the parent mesons.
- ◇ The contributions of multiple scattering and bremsstrahlung are suppressed by a factor of  $\left(\frac{m^e}{m^\mu}\right)^2$  compared to electrons, thus, these

processes have only a small effect on the lateral distribution. In addition, muons are not effected by strong interaction and lose energy only by ionization. Therefore, muons travel almost undisturbed and their tracks show back to their point of production.

- ◇ Their relatively large lifetime,  $\tau_\mu = 2.2 \cdot 10^{-6} s$ , combined with the relativistic effect of time dilation and their fairly small interaction cross sections, make a large fraction of them able to reach the ground before disappear.
- ◇ Primary electrons are enriched in the atmosphere by atmospheric secondaries (decay of charged and neutral mesons and muons) but their atmospheric spectrum falls quickly due to interactions. The integral vertical intensity of electrons plus positrons is approximately 30, 6, and  $0.2 \text{ m}^{-1} \text{ s}^{-1} \text{ sr}^{-1}$  above 10, 100 and 1000 MeV. Above 1 GeV the integral vertical electrons/positrons flux is less than 3 ‰ of the muons one.

In summary, the most abundant charged particles which can be detected at the sea level, are muons, plus a small fraction of protons  $10^{-2}$ , and an even smaller fraction of electrons and positrons  $10^{-3}$ . Figure 1.17 shows the vertical fluxes of atmospheric muons.

The classical definition of the muonic component as the *hard component* [89] is related to penetration characteristics, it is to say the capability of crossing  $167 \text{ g/cm}^2$ , equivalent to roughly 15 cm of Pb. As a matter of fact this component is made of muon with momenta  $p_\mu \leq 0.32 \text{ GeV}$  and less than 1% are protons, neutrons, electrons and pions.

The analytical form of the muon production spectrum at a given height in the atmosphere can be derived by folding the two-body decay kinematics of the parent mesons with their production spectrum. The latter is generally expressed in terms of the *spectrum weighted* moments:

$$Z_{p\pi^\pm} = \int_0^1 x^\gamma \frac{dN_{p\pi^\pm}}{dx} dx \quad (1.33)$$

where  $\frac{dN_{p\pi^\pm}}{dx}$  is the pion production spectrum,  $\gamma$  is the differential spectral index of the primary cosmic rays.

A similar expression can be obtained for kaons.

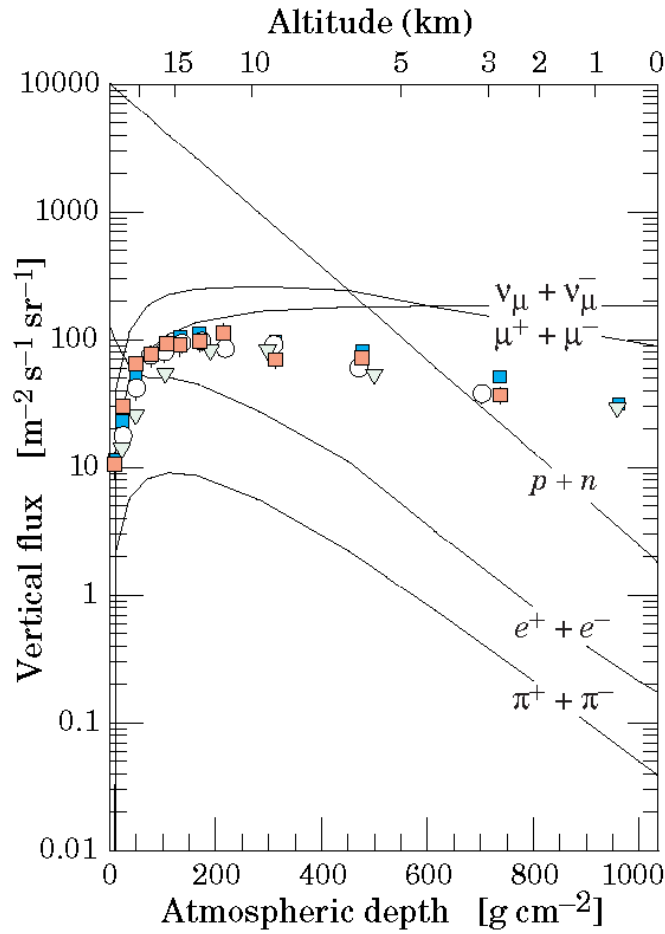


Figure 1.17: Vertical flux of CRs  $E > 1$  GeV in the atmosphere as function of altitude. Negative muon data (markers) and theoretical calculations for the different species (lines) are shown.

Figure 1.17 shows the vertical fluxes of atmospheric muons. The longitudinal development of the muonic component shows an increase of the number of muons up to a maximum number. After the maximum, the number of muons decreases only slowly, showing no pronounced maximum but rather a plateau. This is due to the fact, that the muons do not vanish in interactions and the decay is suppressed by the relativistic time dilatation. The lifetime in the laboratory system is prolonged in such a way, that a decay is improbable. It can also be seen, that the maximum depends weakly on the type of the primary particle, but strongly on the energy of the primary particle. Therefore, the number of muons observed can be used as an energy estimator.

## Charged ratio

Most primary cosmic rays are protons, so there is an excess of positively charged particles with respect to the total number of nucleons. This excess is transmitted via nuclear interactions and decay to pions and further to muons. By assuming that the primary composition is constant in the energy

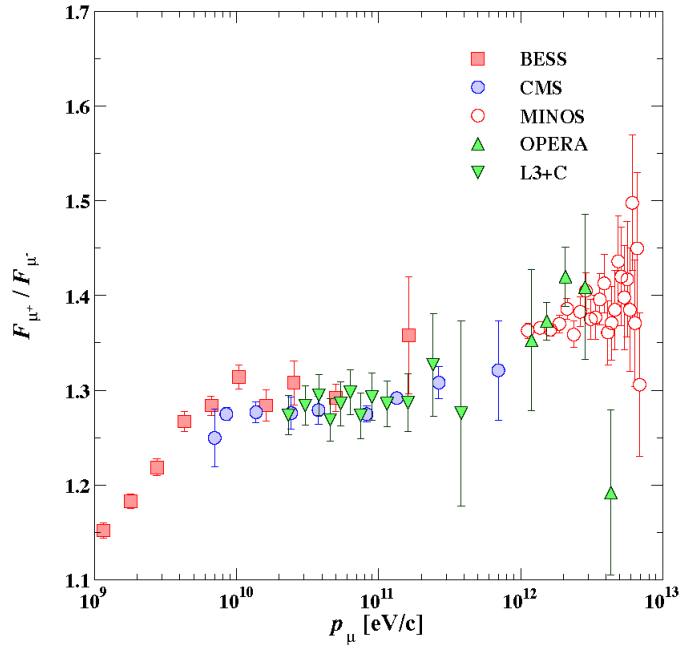


Figure 1.18: Muon charge ratio as a function of the muon momentum.

range considered, this ratio will remain constant with the exception of high energies, where the contribution from kaons.  $p + N \rightarrow \Lambda + k^+$  starts to become sizeable 1.16. The muon charge ratio  $\mu^-/\mu^+$  is expected to increase also with zenith angle as the depth is increasing and likewise the energy of the primaries that produce muons of a given momentum at ground 1.18. This quantity is important to study nucleon-nucleon interactions at very high energy, composition and kaon contribution. Magnetic spectrometers are used for determining this ratio.

### 1.9.4 Energy spectrum

The mean energy of muons at the ground is  $\sim 4$  GeV. The competition between interaction and decay of the particles plays a crucial role and the relative importance of the two processes depends on the energy. Three

different energy regions in the muon spectrum can be identified:

- a)  $E_\mu \gg \epsilon_{\pi,k}$ , where  $\epsilon_\pi = 115 \text{ GeV}$  and  $\epsilon_k = 850 \text{ GeV}$  are the critical energy beyond which meson reinteractions cannot be neglected. This is the typical muon energy range studied by underground detectors or by ground based experiments looking at high inclined directions. In this case, the meson production spectrum have the same power law dependence of the primary cosmic rays, but the rate of their decay has an extra  $E^{-1}$  dependence with respect to the primary and meson spectrum (a consequence of the Lorentz time dilatation). The muon flux takes the form:  $dN/dE_\mu = E_\mu^{-(\gamma+1)}$ , and a zenith dependence  $dN/d\cos\theta \propto (\cos\theta)^{-1}$ .
- b)  $\epsilon_\mu < E_\mu < \epsilon_{\pi,k}$  where  $\epsilon_\mu \sim 1\text{GeV}$ . In this energy range, almost all the mesons decay, and the muon flux has a power law dependence with the same spectral index of the parent mesons (and hence of the primary cosmic ray) and is almost independent on the zenith angle. Most muons lose about  $\sim 2 \text{ GeV}$  to ionization before reaching the ground. The angular distribution of the muon spectrum results  $\propto \sin\theta$ . At lower energies  $E \sim 3\text{GeV}$  the muon spectrum exhibit a totally different angular distribution, i.e.  $\propto \cos^2\theta$
- c)  $E_\mu < 1\text{GeV}$ , muon can decay and the energy losses in the atmosphere cannot be neglected. The spectrum is  $E \propto \cos^2\theta$ , moreover, at lower energy, the angular distribution becomes increasingly steep and geomagnetic latitude and solar modulation play an important role being the primary cosmic ray energy  $E_p < 20 \text{ GeV}$ .

An approximate extrapolation formula valid when muon decay is negligible, for  $E_\mu > \frac{100}{\cos\theta} \text{ GeV}$  and the curvature of the Earth may be neglected ( $\theta < 70^\circ$ ) is:

$$\frac{dN_\mu}{dE_\mu d\Omega} \approx \frac{0.14 E_\mu^{-2.7}}{\text{cm}^2 \text{ s sr GeV}} \left( \frac{1}{1 + \frac{1.1 E_\mu \cos\theta}{115 \text{ GeV}}} + \frac{0.054}{1 + \frac{1.1 E_\mu \cos\theta}{850 \text{ GeV}}} \right) \quad (1.34)$$

Below 10 GeV muon decay and energy loss become important and Gaisser parametrization 1.34 overestimate the muon flux reported in Figure 1.19.

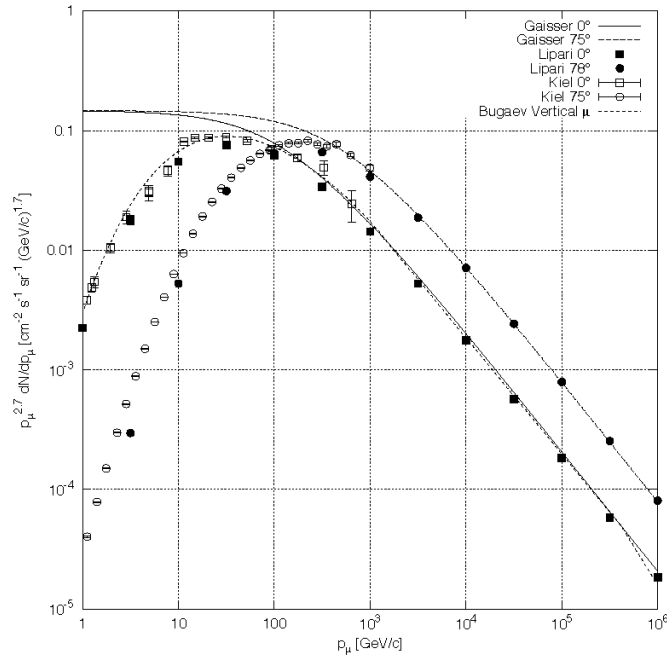


Figure 1.19: Spectrum of muons at  $\theta = 0^\circ$  and  $\theta = 75^\circ$ . The line plots the result from the equation 1.34 for vertical showers.

## 1.10 Periodic and aperiodic variations at the sea level

The integral intensity of vertical muons above 1 GeV/c at sea level is  $I \simeq 70 m^{-2} s^{-1} sr^{-1}$ , for a planar detector  $I \simeq 1 cm^{-2} min^{-1}$ , with recent measurements favoring a lower normalization by 10–15%. [93] *Geomagnetic effects*

The vertical muon intensity at sea level varies with the geomagnetic latitude, altitude, solar activity and atmospheric conditions. The geomagnetic field tends to prevent low energy cosmic rays from penetrating through the magnetosphere down to the Earth's atmosphere. As said in section 1.8, at any point on the Earth one can define a threshold rigidity, for cosmic rays arriving at a particular zenith and azimuth angle 1.25. Primary nuclei having lower rigidity are excluded do not contribute to production of secondaries in the atmosphere. The cutoff values range from less than 1 GV near the geomagnetic poles to about 16 GV for vertical particles near the equator. It results that geomagnetic effects are important for sea level muons up to about  $\sim 5$  GeV. The effect is larger at higher altitudes; Conversi [92] found

that the vertical flux of muons with momentum around 0.33 GeV at latitude  $60^\circ$  was 1.8 times higher with respect to the flux at the equator.

*East-West effects*

As the cosmic ray primaries are predominantly positively charged particles, the flux and spectra in the East and West directions differ up to energies of about 100 GeV; the intensity from the West is stronger than that from the East. This effect increases with altitude.

*Solar modulation*

Galactic cosmic rays decreases, due to Forbush effect, affect the measured muon flux at sea level, giving typical fluctuations of a few percent on a few days basis, see 1.7. The primary cosmic ray spectrum at the top of the atmosphere changes with the 22 year solar cycle as the configuration of the Interplanetary Magnetic Field varies. It results that the muon flux is significantly *modulated* up to energies of about 20 GeV, it mirrors the behavior of primary flux, figure 1.12 due to the *solar potential* 1.20. At the standard momentum of 1 GeV and at high latitudes, as Gaisser said [80], the modulation is 4.5%. Recent results estimated that the total muon flux changes are usually a facto 3 to 5 smaller than the observed neutron flux variations.

*Meteorological effects*

Local changes in temperature and, particularly, pressure above the instrument up to the point of muon production by pions and kaons, produce variations of different amplitude in different energy range. The most conspicuous for muons at higher energies is the seasonal variation [94], but also at lower energy, absorption phenomena can affect the muon flux. The particle intensity can be approximated with an exponential behavior as a function of the pressure:

$$I = I_0 \exp[-\beta(P - P_0)] \quad (1.35)$$

and for small pressure variations one can consider the first order correction  $\Delta I = -\beta\Delta P$ .



## Chapter 2

# Measurements of Anisotropy

### Anisotropy

The arrival direction of charged cosmic rays is basically isotropic, when the low-energy particles affected by the Sun are neglected. This fact can be explained as the effect of the galactic magnetic field which efficiently isotropizes the trajectories of cosmic rays before their arrival at Earth. However, experiments like Milagro, IceCube, ARGO and the Tibet air shower array have observed small anisotropies (at the level of about one part per mille) in cosmic rays with energies above a few TeV.

### 2.1 Galactic Magnetic Field

Precise information on the galactic magnetic field comes from radio astronomy: radio telescopes can measure the Faraday rotation angle and the extent of dispersion of the radiation emitted by pulsars [16]. The Faraday rotation effect is based on the fact that the plane of polarization of linearly polarized electromagnetic waves rotates when they propagate in the presence of a magnetic field  $B$  in a medium with electron density  $N_e$  [ $\text{m}^{-3}$ ]. The rotation depends on the square of the wavelength  $\lambda$ , and on the parallel component of the magnetic field  $B$  along the line of sight to the source:

$$RM = 8.12 \times 10^3 \int_0^L N_e B_{\parallel} dl \quad , \quad RM = \frac{\theta}{\lambda^2} \quad (2.1)$$

where

$\theta$  [rad] is the angle between the direction of wave propagation and the magnetic field direction;

$\lambda$  is the wavelength;

$L$  [pc] is the distance traveled by the radiation;

$B_{\parallel}$  is the component of B parallel to the line of sight;

$N_e$  [ $\text{m}^{-3}$ ] is the electron density.

Therefore, by measuring the variation of the angle of polarization  $\theta$  as a function of the wavelength  $\lambda$  from radio pulsars characterized by linearly polarized radio emission, the rotation measure RM can be estimated and gives information about the integral of  $N_e B_{\parallel}$  along the line of sight. Observations of the Faraday rotation can then be combined with measurements of pulsars dispersion measures defined as the integral along the line of sight of the electron density  $N_e$ . This quantity can be estimated by measuring the arrival time of the pulse  $T_a$  as a function of frequency since the following relation holds:

$$T_a = 4.15 \times 10^9 \frac{1}{\nu^2} \int_0^L N_e dl \text{ s} \quad (2.2)$$

where

$\nu$  [Hz] is the frequency;

$L$  [pc] is the distance traveled by the radiation;

$N_e$  [ $\text{m}^{-3}$ ] is the electron density.

Therefore, it is possible to obtain a weighted estimate of the strength of the magnetic field along the line of sight:

$$\langle B_{\parallel} \rangle \propto \frac{\text{rotation measure}}{\text{dispersion measure}} \propto \frac{\int N_e B_{\parallel} dl}{N_e dl} . \quad (2.3)$$

Different estimates exist on the average intensity of the regular galactic magnetic field, which depends on the distance from the galactic center; a mean value of  $B_z \sim 4\mu\text{G}$  can be assumed. Its orientation is mainly parallel to the galactic plane, with a small vertical component along the z-axis ( $B_z \sim 0.2 - 0.3\mu\text{G}$  vicinity of the Sun). Models of the large-scale structure of the galactic magnetic field exist and provide a regular distribution of the field lines that follows the distribution of matter: a spiral shape [16]. Figure 3.1

shows the direction and strength of the regular magnetic field in the galactic plane. The motion of charged particles with an energy lower than  $E \sim 10^{18}$  eV (see section XX) is strongly influenced by the large-scale structure of the galactic magnetic field as can be seen in fig. XX so that the trajectories of cosmic rays are expected to be efficiently isotropized.

## 2.2 Cosmic-ray detectors

The detection of charged cosmic rays may be done at top of the Earth atmosphere in balloon or satellite based experiments whenever the fluxes are high enough (typically below tens or hundreds of GeV). They operate at an altitude above 15 km where they can detect the interaction of the primary particle inside the detector, but they are limited in detection area and so also limited in the energy range they can measure. Otherwise above this energy the observations are performed by exploiting the cascades induced in atmosphere by the interactions of cosmic rays.

In the following, two satellite experiments are presented. Their detection principle is aimed at (i) the identification of the particle, (ii) the measure of its electric charge and (iii) the measure of its energy and momentum. This is usually obtained by means of a magnetic field, a tracking system and a calorimeter.

### PAMELA

The PAMELA experiment launched in June 2006 measured charged particle and antiparticles out of the Earth atmosphere during a long (six years) time period. A good charge separation between electron and positrons was ensured by a permanent magnet of 0.43 T and a microstrip silicon tracking system up to energies of the order of the hundred of GeV measured by a silicon/tungsten electromagnetic calorimeter complemented by a neutron counter to enhance the electromagnetic/hadronic discrimination power. The trigger was provided by a system of plastic scintillators which were also used to measure the time-of-flight and an estimation of the specific ionization energy loss ( $dE/dX$ ) (Fig.2.1).

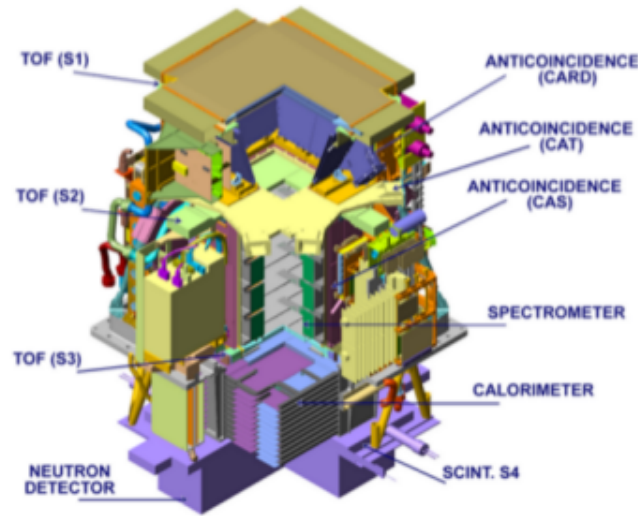


Figure 2.1: The PAMELA detector layout. Credit: PAMELA Collaboration..

## AMS-02

The Alpha Magnetic Spectrometer, AMS-02, was installed in May 2011 on the International Space Station. Its layout is similar to PAMELA but with a much larger acceptance and a more complete set of sophisticated and higher performing detectors. Apart from the permanent magnet and the precision silicon tracker it consists of a transition radiation detector, time-of-flight and anti-coincidence counters, a ring imaging Cherenkov detector and an electromagnetic calorimeter (Fig.2.2).

### 2.2.1 Extensive air showers

High-energy hadrons, photons and electrons interact in the high atmosphere. The process characterizing hadronic and electromagnetic showers is similar. For photons and electrons above a few hundred MeV, the cascade process is dominated by the pair production and the bremsstrahlung mechanisms: an energetic photon scatters on an atmospheric nucleus and produces a pair, which emits secondary photons via bremsstrahlung; such photons produce in turn a  $e^+ e^-$  pair, and so on, giving rise to a shower of charged particles and photons. The longitudinal development of typical photon-induced extensive air showers is shown in Figure 2.3 for different values of the primary energies. The maximum shower size occurs approximately at  $\ln(E/E_0)$  radiation lengths, where the radiation length for air is about 37

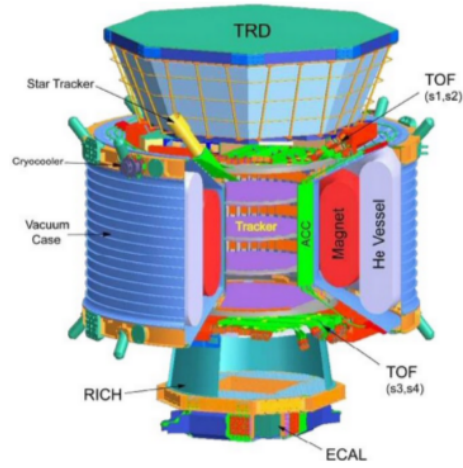


Figure 2.2: The AMS-02 detector layout. Credit: AMS Collaboration.

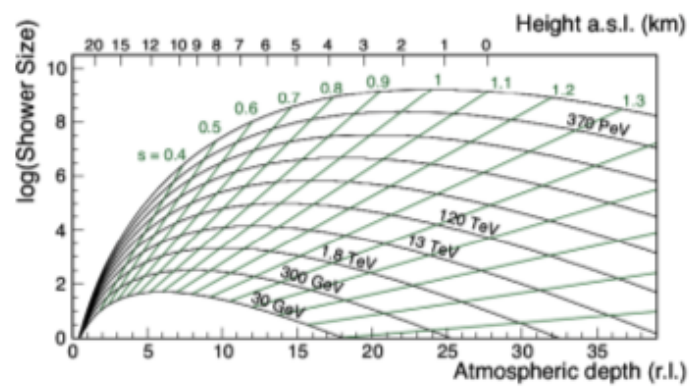


Figure 2.3: Longitudinal shower development from a photon-initiated cascade. The parameter  $s$  describes the shower age.

$\text{g}/\text{cm}^2$  (approximately 300 meters at sea level and NTP). The critical energy  $E_0$ , the energy below which the ionization energy loss starts to dominate the energy loss by bremsstrahlung, is about 80 MeV in air. The hadronic interaction length in air is about  $61 \text{ g}/\text{cm}^2$  for protons (500 meters for air at NTP), being shorter for heavier nuclei. The dependence of the cross section on the mass number  $A$  is approximately  $A^{2/3}$ . The transverse profile of hadronic showers is in general wider than for electromagnetic showers, and fluctuations are larger. Particles release energy in the atmosphere, which acts like a calorimeter, through different mechanisms, which give rise to a measurable signal, mainly fluorescence and Cherenkov radiation.

Extensive air showers (EAS) produced by high energy cosmic rays are detected using three different techniques.

- ◇ **Surface Detectors:** the measurement of a fraction of the EAS particles arriving at the Earth surface through an array of surface detectors (SD),
- ◇ **Fluorescence Detectors:** the measurement in moonless nights of the fluorescence light emitted mainly by the excitation of the atmosphere nitrogen molecules by the shower low energetic electrons through an array of ultra-violet fluorescence detectors (FD) placed on the Earth surface or even in satellites.
- ◇ **Imaging Atmosphere Cherenkov Telescopes:** the measurement of the Cherenkov light emitted by the ultra-relativistic air shower particles in a narrow cone around the shower axis, through dedicated telescopes as the Imaging Atmosphere Cherenkov Telescopes (IACTs).

### Surface Detectors

Surface detectors measure at specific space locations the time of arrival of individual particles. The most widely used surface detectors are scintillation counters and water Cherenkov counters. The arrival direction of an air shower is determined from the arrival time at the different surface detectors of the shower front, which, in a first approximation, can be described by a thin disk that propagates with the speed of light. The impact point of the air shower axis at the Earth surface (the air shower core) is defined as the point of maximum particle density and is determined from the measured densities at the different surface detectors. The measured densities are

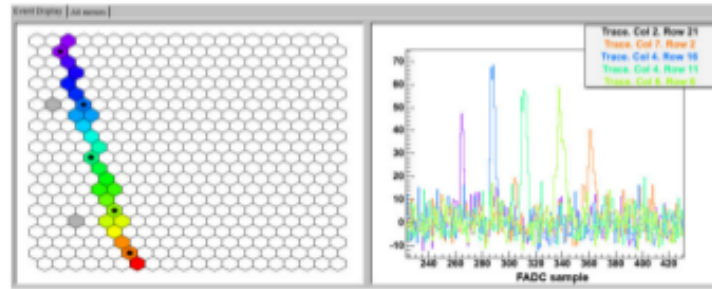


Figure 2.4: Display of one shower in the focal plane of one of the Pierre Auger fluorescence telescopes. Left: Pattern of the pixels with signal; right: response (signal versus time, with a time bin of 100 ns) of the selected pixels (marked with a black dot in the left panel). The development of the shower in the atmosphere can be qualitatively pictured. From [www.auger.org](http://www.auger.org).

usually parameterized by empirical or phenomenological inspired formulae, which depend also on the shower age (the level of development of the shower in the moment when it arrive at the Earth surface). Such functions allow for a better determination of the shower core and for the extrapolation of the particle density to a reference distance of the core which is then used as an estimator of the shower size and thus of the shower energy. The exact function as well as the reference distance depends on the particular experiment setup.

### Fluorescence Detectors

The fluorescence telescopes record the intensity and arrival time of the light emitted in the atmosphere in specific solid angle regions and thus are able to reconstruct the shower axis geometry and the shower longitudinal profile. In Figure 2.4 the image of a shower in the focal plane of one of the Pierre Auger fluorescence telescope (see later) is shown. The third dimension, time, is represented in a color code. The geometry of the shower is then reconstructed in two steps: first the shower detector plane (SDP) is found by minimizing the direction of the SDP normal to the mean directions of the triggered pixels, and then the shower axis parameters within the SDP are found from the measured arrival time of the light in each pixel assuming that the shower develops along a line at the speed of light. The simultaneous observation of the shower by two (stereo) or more fluorescence detectors or by a surface detector array (hybrid detection) provides further geometric constrains which improve considerably the resolution of the shower geomet-

ric reconstruction.

### Imaging Atmosphere Cherenkov Telescopes

Many secondary particles in the EAS are superluminal, and thus they give rise to the emission of Cherenkov light that can be used for the detection. At 8 km, the value of the Cherenkov angle  $\Theta_C$  in air for  $\beta = 1$  is about  $1^\circ$ . Half of the emission occurs within 20 m of the shower axis (about 70 m for a proton shower). The observational technique used by the IACTs is to project the Cherenkov light collected in a large optical reflecting surface onto a camera which is basically an array of photomultipliers, with typical quantum efficiency of about 30%, in the focal plane of the reflector. The camera has a typical diameter of about 1 m, and covers a FoV of  $5^\circ \times 5^\circ$ . The signal collected by the camera is analogically transmitted to trigger systems, similar to the ones used in high-energy physics. The events which pass the trigger levels are sent to the data acquisition system, which typically operates at a frequency of a few hundreds Hz. The typical resolution on the arrival time of a signal on a photomultiplier is better than 1 ns. The shower has a duration of a few ns (about 2 to 3) at ground; this duration can be maintained by an isochronous (parabolic) reflector.

#### 2.2.2 Experiments for the EAS detection

As an example, some different experiments for the detection of UHECRs are described.

##### The Pierre Auger Observatory

The Pierre Auger Observatory in Malargue, Argentina, is the largest cosmic ray detector ever built. It covers a surface of about 3000 square kilometers with 1600 surface detector stations (Cherenkov water tanks) arranged in a triangular grid of 1.5 km side complemented by 24 fluorescence telescopes, grouped into four locations to cover the atmosphere above the detector area (Figure 2.5). Each water tank is a cylinder of  $10 \text{ m}^2$  base by 1.5 m height filled with 12 tons of water (Figure 2.6). The inner walls of the tank are covered with a high reflectivity material. The Cherenkov light, produced by the charged particles crossing the tank, is collected by three PMT placed on the top of the tank. Each tank is autonomous being the time given by a GPS unit and the power provided by a solar panel; it communicates via

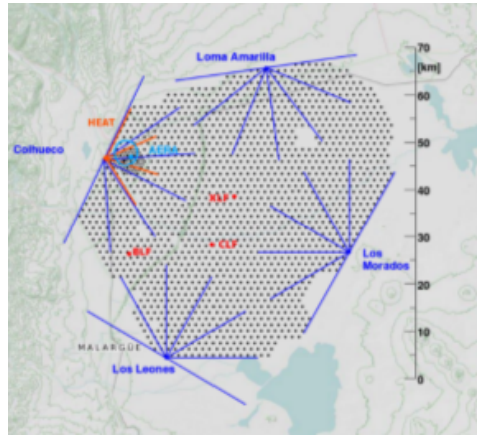


Figure 2.5: The Pierre Auger Observatory near Malargue, Argentina. The radial lines point to the fluorescence detectors (FD,  $4 \times 6 = 24$ ). The black dots are the 1600 ground stations (SD).

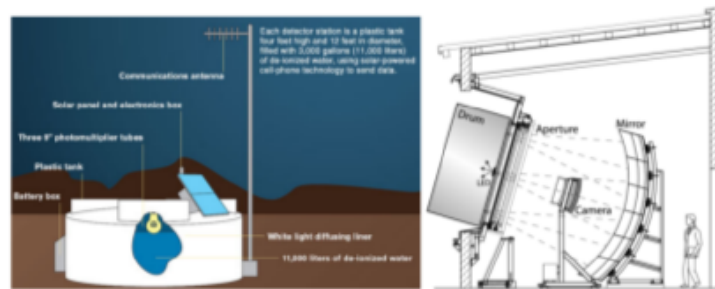


Figure 2.6: Sketch of one of the Pierre Auger surface detectors (left); a fluorescence telescope (right). From [www.auger.org](http://www.auger.org).

radio with the central data acquisition system. Each fluorescence detector is a Schmidt telescope with a field of view of  $30^\circ$  in azimuth and  $29^\circ$  in elevation (2.6). The light enters the telescope through an ultra-violet filter installed over the telescope circular diaphragm cross and is collected in a 3.5 m diameter spherical mirror which focus it in a 440 PMT camera.

### Telescope Array

The largest cosmic ray detector in the northern hemisphere is the Telescope Array (TA) in Utah, USA. Similar to Auger, it is also an hybrid detector composed by a surface array of 507 scintillator detectors, each 3 m in size, located on a 1.2 km square grid, plus three fluorescence stations each one with a dozen of telescopes each instrumented with a 256 PMT camera cov-

ering 3 to 33 degrees in elevation. The total surface covered is about 800 square kilometers.

### **HAWC**

HAWC is a very high-energy gamma-ray observatory located in Mexico at an altitude of 4100 m. It consists of 300 steel tanks of 7.3 m diameter and 4.5 m deep, covering an instrumented area of about 22000 m<sup>2</sup>. Each tank is filled with purified water and contains three PMT of 20 cm diameter, which observe the Cherenkov light emitted in water by superluminal particles in atmospheric air showers. Photons traveling through the water typically undergo Compton scattering or produce an electron-positron pair, also resulting in Cherenkov light emission. This is an advantage of the water Cherenkov technique, as photons constitute a large fraction of the electromagnetic component of an air shower at ground.

## Chapter 3

# The Cosmic Radiation and the EEE Project

### 3.1 Telescope Array for the Cosmic Rays detection

The main difficulty in studying the high energy cosmic rays is their extremely low intensity. Detection of cosmic ray phenomena over large areas requires therefore bigger detection areas, which at present are economically feasible only with more sparse EAS arrays, on average much fewer than one detector per  $\text{km}^2$ . In fact, global positioning system (GPS) technology makes it possible to perform precision timing over large areas, enabling several detectors to be deployed as essentially one huge network. With the aim to increase the area coverage a growing number of cosmic ray air shower detector arrays around the world use high schools sites as nodes for the detectors.

Densely populated areas are the ideal location for the measurement stations. The necessary infrastructure, such as Internet and mains voltage, is available there. The average distance between high schools and other public organizations is roughly the same as the desired distance between measurement stations: about 1 km. Besides offering suitable locations, high schools can provide sufficient enthusiastic manpower (teachers, technical assistants and pupils) to monitor the detectors and keep them operational.

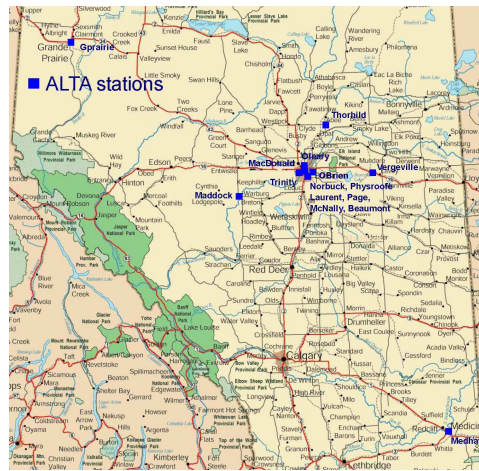


Figure 3.1: A map of ALTA detector sites in Canada. The cluster of blue boxes in the center of the map marks the detection network in Edmonton (Alberta).

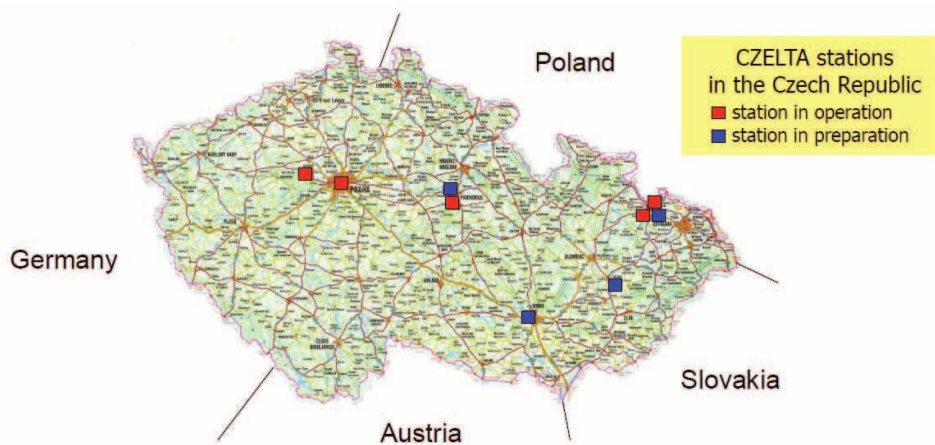


Figure 3.2: A map of CZELTA detector sites in the Czech Republic.

## 3.2 Sparse Detector Array in High Schools

### 3.2.1 ALTA/CZELTA - A sparse very large air shower array

The University of Alberta, the Czech Technical University in Prague and the Silesian University in Opava realized a project for the detection of high energy cosmic rays with a relatively sparse network of detection stations Fig. 3.1. In 1998 in Alberta, building on a proposal first presented in 1995, the first node of this kind of sparse very-large-area network of cosmic-ray detectors began to take data. The detection network covering the area in Canada is called ALTA Alberta Large-area Time coincidence Array and the network located in the Czech Republic is named CZELTA CZEch Large-area Time



Figure 3.3: Picture of a ALTA station in Canada, the boxes contain the scintillation detectors.

coincidence Array, Fig. 3.2. The primary objective of the common project ALTA/CZELTA is to find correlation in the arrival times of air showers over large distances and to find non-random component of air shower arriving at the single site [102]. The detection station are placed mainly on the roof and on the attic of high school buildings in Canada and in the Czech Republic. Student from those schools who are interested in research participate in the project. The hardware of the station is identical for both sub-network ALTA and CZELTA [101]. Each station is composed of three scintillation detectors, which are placed into a triangle configuration as in Fig.3.3, and use GPS signals for time-labeling of events. The distance between all pairs of scintillator is 10 m. One scintillation detector has dimensions of 60 cm x 60 cm x 1 cm and is connected to a photomultiplier, which detects photons originating from the passage of an extensive air shower through the scintillator. The detectors work in a coincidence. A shower of secondary particles must hit all three scintillation detectors in order to be stored. In such a case, the energy of a primary particle is at least  $\sim 10^{14}$  eV, as in Fig.3.4.

### 3.2.2 NALTA - The North American Large-area Time Coincidence Arrays

In 2000 the Cosmic Ray Observatory Project CROP, centered at the University of Nebraska, set up five schools with detectors from the decommissioned Chicago Air Shower Array, CASA [103]. Around the same time the Washington Large-area Time-coincidence Array, WALTA, installed its first detectors.

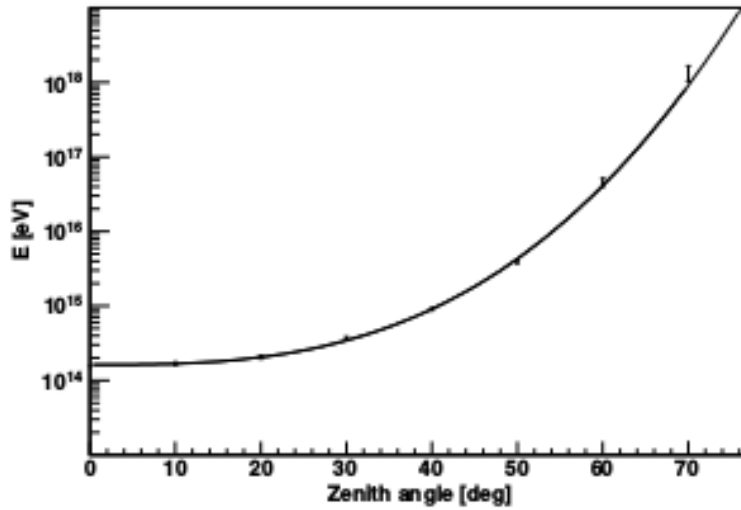


Figure 3.4: Minimal energy of a primary proton which can produce a detectable shower in a ALTA/CZELTA station as a function of a zenith angle.

The detector systems are simple, following the ALTA/CZELTA model they use a small local array of plastic scintillators, which are read by custom-made electronics. The ALTA/CROP/WALTA arrays involve more than 60 high schools and there are three further North American educational arrays in operation: the California High School Cosmic Ray Observatory, CHICOS, and the Snowmass Area Large-scale Time-coincidence Array SALTA in the US, and the Victoria Time-coincidence Array, VICTA, in Canada. And seven more North American projects have been developed. The CHICOS array is the largest ground-based array in the North America. Its detectors, donated by the CYGNUS collaboration [105], are deployed on more than 70 high-school rooftops across 400 km<sup>2</sup> in the Los Angeles area. Each site has two 1 m<sup>2</sup> plastic scintillator detectors separated by a few meters. CHICOS observed some excess events, with  $\Delta T = 30$  *mus*, but with further results were found to be compatible with random coincidences [104].

Most of the major groups in Canada and the US have formed a loose collaboration, the North American Large-area Time Coincidence Arrays NALTA, with more than 100 detector stations spread across North America, Fig. 3.5. The aim is to share educational resources and information. It is also planned to have one central access point where students and researchers can use data from all of the NALTA sites, creating a single giant array.



Figure 3.5: The geographical distribution of the main educational cosmic rays array centers in NALTA.

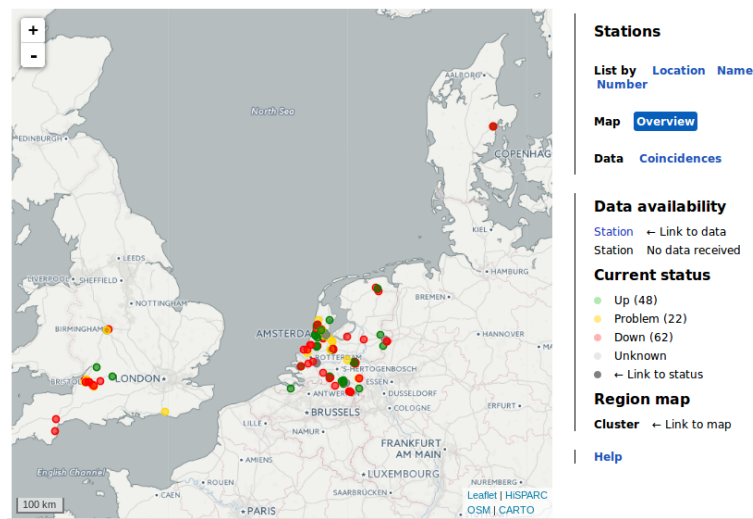


Figure 3.6: Map of HiSPARC stations, from the HiSPARC public database. The status of each station is indicated by colored indicators [106].

### 3.2.3 HiSPARC - High School Project on Astrophysics Research with Cosmics

The High School Project on Astrophysics Research with Cosmics, HiSPARC, experiment, consisting of a growing number of cosmic rays measurement stations scattered over the Netherlands, Denmark and the United Kingdom,

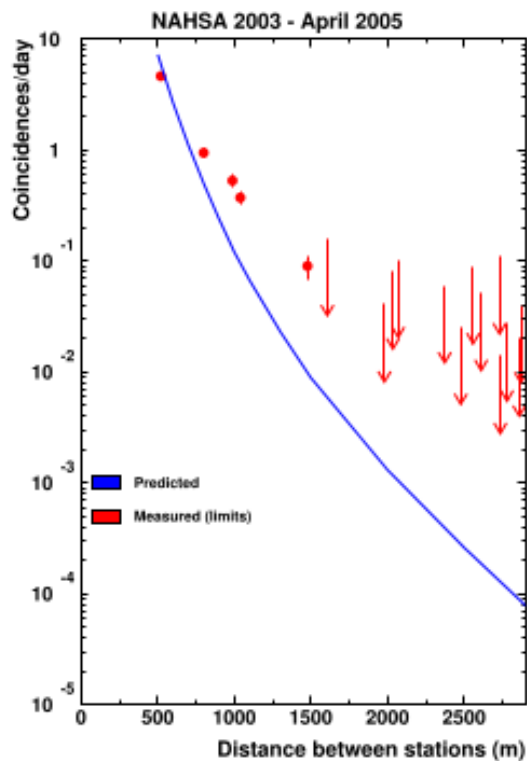


Figure 3.7: The number of measured and expected coincidences between stations in HiSPARC as function of the distance.

detects EAS particles using scintillators. The HiSPARC experiment started in 2001 when the first stations got built under the name NAHSA, under the guidance of the Radboud University of Nijmegen in the Netherlands. At present more than 100 high schools from different country are involved in a “school” international collaboration. The stations of the HiSPARC array are uniform: a minimum setup consisting of two ski-boxes with scintillator and photomultiplier, a GPS device and a HiSPARC II readout and control box [107]. The HiSPARC II box is responsible for the data acquisition, the control of the PMTs (high-voltage) and the control and readout of the GPS device. HiSPARC array detected events at more than one kilometer distance with three different station. On February 2005 an event was seen in Amsterdam, where the relative distances between the three detectors were 845,1216 and 1535 m, and on March an event was recorded in Nijmegen, where the distances were 988, 2477 and 2780 m. The energy of the latter event has been estimated to be almost  $8 \times 10^{19}$  eV, in the ultra-high-energy “ankle” region of the cosmic-ray energy spectrum [108]. The chance proba-

bility of the occurrence of this triple coincidence has been estimated to be less than  $3 \times 10^{-4}$ , Fig. 3.7 The HiSPARC collaboration is also planning to use a recent development of the Low Frequency Array Prototype Station, LOPES experiment in Karlsruhe. Using a relatively simple radio antenna, LOPES detects the coherent low frequency radio signal that accompanies the showers of secondary particles from ultra high energy cosmic rays [109]. A large array of these low frequency radio antennas, the LOFAR observatory, is already being constructed in the Netherlands [110].

### 3.2.4 European Arrays

Many European countries are also getting involved in studying the extreme energy universe with detector networks inside High Schools. The Stockholm Educational Air Shower Array, SEASA, has a dense cluster of scintillator stations located at AlbaNova University Centre, with the aims to study the cosmic ray anisotropy around the knee [112]. There are the School Physics Project in Finland, a project of more than 10 stations in the Lisboa area in Portugal. In the UK, the King's College in collaboration with the Canadian ALTA group places detector systems in the London area, RoALTA in Romanian, COSMOS a l'Ecole, MAZE in Poland [103]. Many others interested European universities have organized themselves in the EuroCosmics consortium which is a network of research institute and high schools across Europe to study physics, properties and origin of cosmic rays.

### 3.2.5 MARIACHI - The Mixed Apparatus for Radar Investigation of Cosmic Rays of High Ionization

Innovative detection techniques have also been employed in North America. The Mixed Apparatus for Radar Investigation of Cosmic Rays of High Ionization is a research project created and directed by Brookhaven National Laboratory for the detection of UHECR via bi-static radar interferometry using VHF transmitters [111]. The plan is for the experiment to detect UHECRs by means of a VHF signal, which could be reflected off the ionization patch produced by a cosmic ray shower. The stations, also equipped with conventional cosmic ray shower detectors, continuously will listen to a radio frequency that illuminates the sky above it searching the ionization trials of the UHECRs.

### 3.3 The Extreme Energy Events Project

The Extreme Energy Events Project, EEE Project, is a high energy physics experiment with the main goal of studying the EAS on ground level by means of a very large detector array. The EEE Project was conceived in 2003 by its scientific leader, professor Antonino Zichichi [100], and is carried out by the Italian institute Museo Storico della Fisica e Centro Studi e Ricerche Enrico Fermi - *Centro Fermi* [99], in collaboration with CERN, MIUR (the Italian Ministry of Education, University and Research) and INFN (the National Institute of Nuclear Physics).<sup>1</sup>

Essentially the project makes use of the standard technique, the detection of the shower muon component of the EAS, arriving to the ground level, generated by the energetic primaries when they enter the atmosphere. Due to the high energy of the primaries, the corresponding showers may impinge on the ground with millions of particles scattered on some km radius area. Therefore a network of detectors with an elevate number of stations, distributed on a large surface has been needed. The peculiarity of the EEE Project lies in the fact that the station are hosted in Italian high schools, plus CERN and INFN sections, spared across Italy, covering an area of around  $3 \times 10^6$  km<sup>2</sup>, placed as the Fig.3.8. Several educational cosmic ray projects have been proposed in recent years, involving also high school institutions, Fig.3.2. Most of such projects, installed in High Schools, make use of detector stations which include two or three scintillators operating in coincidence, to provide a local trigger which can be used to search for long distance correlations. The EEE Project is the only array which does not employ plastic scintillator as a detector, instead is based on the use of Multigap Resistive Plate Chambers (MRPC), which are gas detectors with very good time and position resolution. A picture of a EEE cosmic ray station, hosted in a italian high school in Savona, in shown in Fig:3.9

The tracking capability of the EEE telescopes allows to carry out a variety of physics investigations [ref. scientific activity], in particular the detection of the EAS muon component. Each array's station can reconstruct the direction of incoming muons produced in the EAS, thus the EEE Project detectors allow to evaluate with reasonable precision the orientation of the primary nucleus [ref. Looking], [ref. parMonteCarlo]. Beyond its interesting

---

<sup>1</sup>CERN Conseil Européen pur la Recherche Nucléaire, MIUR Ministero Istruzione Università e Ricerca, INFN Istituto Nazionale di Fisica Nucleare.



Figure 3.8: Map of the EEE network sites: the red points correspond to schools hosting a detector, the blue ones to schools participating in the EEE Project even without hosting a detector.

scientific goals, the EEE Project aims at introducing high school students to particle and astroparticle physics through their direct involvement: most of the activities related to the experiment are carried out by high school students and teachers, working in close contact with scientists and technicians. From the point of view of scientific communication and outreach activities, this is a very important added value to the Project.

### 3.3.1 Outreach activities

The innovative aspect of the the EEE Project is that the stations, located in Italian high schools, are operated by teachers and students of these school, and the MRPC detectors themselves have been built at CERN by the same

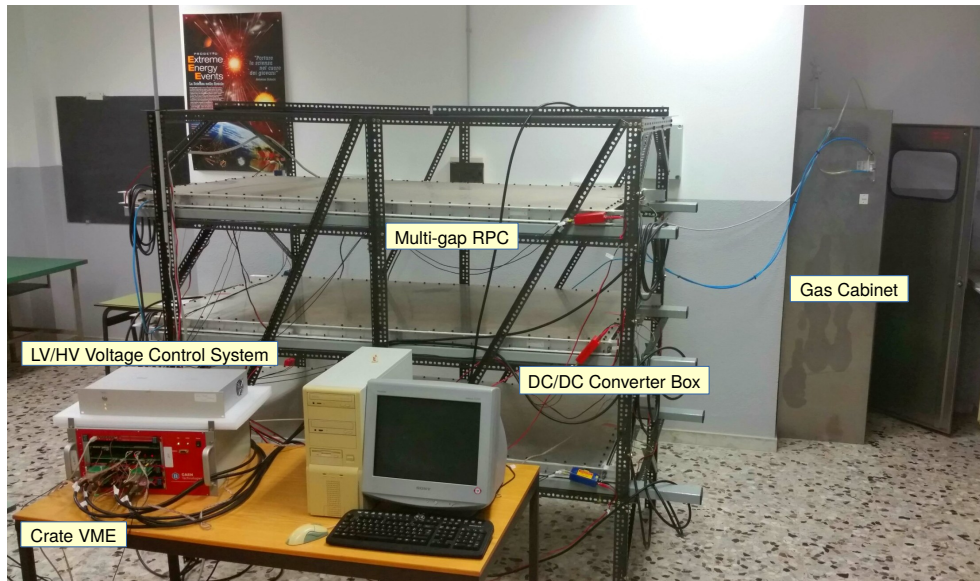


Figure 3.9: The EEE cosmic ray station at ITIS Galileo Ferraris in Savona.

teachers and students. Thus the EEE Project has the possibility to be a very effective method to communicate the meaning of the scientific research to a wide selected audience, summarized in its motto: *Bring Science to the heart of the young* [100] [99]. This was one of the reasons why it was decided to locate the EEE telescopes in high schools and to have students help hands on in the assembling, testing and monitoring of the detectors and in data taking and analysis.

When a new EEE telescope is going to be added to the array most of its building process is participated by the students: after some introductory lessons by the school teachers on cosmic ray physics and MRPC detectors, roughly five students per school are selected to go to CERN with 1 or 2 teachers for a one-week stay to assemble the chambers, under the guidance of scientific collaboration researchers. This proves to be a very fruitful period for the students, during which they learn how to work in a team and live, even if only for a short time, the researcher life. At the end of the week they are taken to visit some of the LHC experiments, where they can see detectors very similar to the ones they just built and which are actually used in collider experiments.

Once the chambers arrive at the schools, with the help and under the supervision of the researchers from the scientific institutions, students and teachers take part in the first tests and in the commissioning; moreover, they

CITTÀ	ISTITUTO
Altamura (BA)	Liceo Cagnazzi
Ancona	Liceo Classico C. Rinaldini
Arezzo	ITIS G. Galilei
Bari	Liceo Scientifico A. Scacchi
Bologna	Liceo Scientifico E. Fermi
	Liceo Classico L. Galvani
Cagliari	Liceo Scientifico L.B. Alberti
	Liceo Scientifico Michelangelo
	Liceo Scientifico A. Pacinotti
Catania	ITIS S.Cannizzaro
Catanzaro	IIS E. Fermi
Cosenza	Liceo Scientifico G.B. Scorza
Frascati (RM)	Istituto Tecnico E. Fermi
	Istituto Salesiano Villa Sora
Grosseto	Rete Scuole della Cittadella dello Studente - IIS A.Manetti (2 TELESCOPI)
Grottaferrata (RM)	Liceo Scientifico B. Touschek
L'Aquila	Liceo Scientifico A. Bafile
	ITIS A. D'Aosta
Lecce	Liceo Scientifico G.Banzi Bazoli
	ITIS E. Fermi
	Liceo Classico Palmieri
Lodi	Liceo Scientifico G. Gandini
Lodi	ITIS Volta
Parma	Liceo Scientifico G. Marconi
Paternò (CT)	Liceo Scientifico E. Fermi
Reggio Emilia	IIS L. Nobili
Roma	ITIS H. Hertz
	Liceo Classico P. Albertelli
Salerno	Liceo Scientifico G. Da Procida
Salerno	Liceo Statale "Regina Margherita"
Savona	Liceo Chiabrera - Martini
	ITIS Ferraris-Pancaldo
	Liceo Scientifico O. Grassi
Siena	Istituto Sarrocchi
	Liceo Galilei
Teramo	IIS Alessandrini - Marino - Forti
Torino	Liceo Classico M. d'Azeglio
	Liceo Scientifico G. Ferraris
	Liceo Scientifico G. Bruno
	Liceo Scientifico A. Volta
Trapani	Liceo Scientifico V.Fardella
Treviso	Liceo Duca degli Abruzzi
Trinitapoli (BAT)	IISS S. Staffa
Viareggio (LU)	IIS Galilei - Artiglio
	Liceo Scientifico Barsanti e Matteucci

Figure 3.10: The Italian high schools hosting an EEE station [99]

measure the chamber efficiency, and the angle of orientation of the chambers with the geographic North. Later on, during the data taking stage, the students are taught how to monitor the telescopes and they provide the daily checks which are mandatory to keep the system running.

Furthermore, schools join the EEE Project even without hosting a EEE telescope. As in a real scientific collaboration their teams of students and teachers help monitoring directly EEE stations located in other schools by

means of the EEE Data Acquisition Monitor, the dedicated web interface which provides the on-time status overview of all the EEE array stations [ref. EEEmonitor].

Since the first coordinated data taking of all the EEE network (2014), data from all the EEE station are available for the students [ref. RunCoord], from schools with and without a telescope. They learn how to treat and analyze them using specific analysis tools, part of which have been developed by teams of teachers and students themselves.

They deepen their knowledge about particle physics through targeted lectures and “master classes” in specific areas of data analysis, and every year they participate at annual meetings between all the schools in the EEE Project where they are invited to exchange ideas and experiences each others.

Monthly video-conferences for the schools participating to the project are held since November 2016. In these meetings students are updated on the latest news of the project and present their activities to the entire collaboration.

Almost all the schools, moreover, set up their own EEE Project web page, where they store all the relevant info on about how the project develops at the different sites.

In addition, since younger students work in close contact with more experienced ones, the acquired skills are transmitted in the most natural way.

At the present around 100 schools have been involved in the EEE Project, the average number of students taking part to the EEE Project is around 8 per school, for a total of around eight hundred young students and 150 teachers. Every year new schools join the project, and the MRPCs network continuously increases its surface coverage. Undoubtedly the EEE Project combines successfully its scientific results with a powerful educational approach.

### **3.3.2 The EEE telescope Array**

The sparse array of the EEE Project consists of muon telescopes, most of which are located in high schools buildings distributed all across the Italian territory, while two of them are installed at CERN and three at INFN sites in order to perform checks, develop new tools and solutions for the tele-

scopes operations and data acquisition. The network is organized with close detectors concentrated in the same town, “cluster” of 2, 3, 4 telescopes with relative distances from hundred meters to few kilometers, and additional sites far hundreds of kilometers from the others to increase the total surface covered. A map of the EEE cosmic ray stations, in red, is shown in Fig. 3.8. Currently the largest distance between the EEE telescopes is about 1200 km, between CERN laboratories and Catania, and the smallest 18 m between the two stations at CERN. The present list of the Italian high schools hosting an EEE station is also shown in Fig. 3.10.

The EEE Project started with the construction of the first clusters in seven pilot towns, taking data since 2008. After 10 years, at present 52 telescopes have been built.

The particular grid design chosen for the EEE sparse array provides to investigate several aspects of the cosmic ray radiation:

*as single detector* the EEE telescope is a high precision tracking detector that can study the flux of secondary cosmic muons, their arrival directions and the up-going particles, and how the variations of the local flux is influenced by several aspects, such as the environmental parameters or sudden solar events.

*as telescopes cluster* in the same metropolitan area, it aims to study the properties of the EAS in which muons are originated.

*as an array* using sites placed hundred kilometers apart, it makes possible to investigate long-baseline correlations caused by two (or more) time-correlated EAS originated by a common mechanism.

### 3.4 The Multi-gap RPCs for the EEE Project

The detector technology chosen for the experiment had to fulfill several design requirements, as long term operation, high detection efficiency, good time and spatial resolution, being inexpensive for large area coverage. Moreover each station has to reconstruct the orientation of the incoming particles. The construction technique has to be rather simple, and based on commercially available materials, that can be part of the everyday life for the young students participating to the chamber assembling. The final choice was a telescope made of three MRPC [?], whose design is a larger, simpler ver-

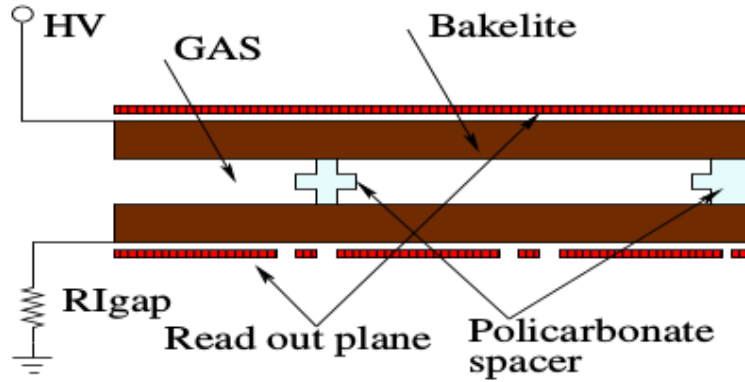


Figure 3.11: Schematic view of a single RPC gap.

sion, but with operation characteristic similar to the MRPC developed for the ALICE Time Of Flight detector <sup>2</sup> [117].

### 3.4.1 The Resistive Plate Chambers

Resistive Plate Chambers, RPC, were developed in 1981 by R.Santonico and R. Cardarelli [118] [119]. The RPCs are gaseous parallel-plane detector, with a typical space-time resolution of the order of  $1 \text{ cm} \times 1 \text{ ns}$ , with digital readout.

The RPC operation is based on the detection of the electrical discharge generated when a charged particle passes through a gas volume. RPC are the evolution of the Parallel Plate Avalanche Chamber, PPAC, introduced by Pestov [120], which used a metallic plane as electrode; as a consequence of this choice when a charged particle generated an electrical discharge, the electrical potential on the detector surface decreased, increasing the dead time of the detector. The introduction of a resistive plate as electrode removed this limitation and made easier the realization of the detector. A typical RPC is made of two bakelite plate kept parallel by insulating spacer, which define the size of the gas gap. Fig. 3.11 shows a schematic image of an example configuration of an RPC. These plates are painted with a graphite coating of surface resistivity 200 to 300  $\text{k}\Omega/\text{cm}$ , which is used to distribute the high voltage on the electrodes. The shown configuration utilizes read out strips running along the whole length of the chamber. The strips are separated from the graphite coating by an insulating layer. A very high uniform field, produced by a differential potential applied on the bakelite

<sup>2</sup>ALICE A Large Ion Collider Experiment.

plates, produces the avalanche multiplication of the ionization electrons. The signal is read out via capacitive coupling to metal strips or pads placed at both sides of the detector.

### 3.4.2 RPC working principle

When a particle goes through a material it loses energy in according to the Bethe-Bloch formula [122]. The inelastic collision of a particle in gaseous means can produce electron-ions pair *primary ionization*. If the electron generated from the primary ionization has enough energy, it can itself generate an electron-ions pair *secondary ionization*.

If an electric field is applied to the gas container the electron and ions start to drift along the field line. The electron liberated by this secondary ionization process will also be accelerated by the electric field. During its subsequent drift, it undergoes collisions with other neutral gas molecules and thus it can create additional ionization. Since the average energy of the electron between collisions increases with increasing electric field, there is a threshold value of the field above which this secondary ionization will occur. In typical gases, at atmospheric pressure, the threshold field is of the order of  $10^6$  V/m [121]. The gas multiplication process therefore takes the form of a cascade, known as *Townsend avalanche*, in which each free electron created in such a collision can potentially create more free electrons by the same process. The fractional increase in the number of the electrons  $n$  per unit path length is governed by the Townsend equation:

$$\frac{dn}{n} = \alpha dx \quad (3.1)$$

$\alpha$  is the first *Townsend coefficient* for the gas and corresponds to the inverse of the electron mean free path for ionization. Its value is zero for electric field values below the threshold and generally increases with increasing field strength above this minimum. For a spatially constant field, as in parallel plate geometry,  $\alpha$  is a constant in the Townsend equation. Its solution then predicts that the density of electrons grows exponentially with the distance as the avalanche progresses:

$$N(x) = N_0 e^{\alpha x} \quad (3.2)$$

where  $N_0$  is the initial number of electron,  $\alpha$  depends on the applied high voltage and on gas mixture and  $x$  is the path where avalanche grow up. If the single-electron response is known, the amplitude properties of pulses produced by many original ion pairs can be deduced. Provided that the space charge effects are not large enough to distort the electric field, each avalanche is independent and the total charge  $Q$  generated by  $N_0$  original ion pairs is:

$$Q = N_0 e M \quad (3.3)$$

where  $M$  is the *average gas multiplication factor* that characterizes the counter operation.

The multiplication factor cannot be increased at will with increasing the path  $x$ . Other processes, like photon emission inducing the generation of avalanche spread over the gas volume, and deformation of the electric field due to space-charge eventually results in a spark breakdown. A phenomenological limit for the multiplication before breakdown is given by the Raether - or Meek - condition [123] [124]:

$$\alpha x \sim 20 \text{ or equivalently } M \sim 10^8 \quad (3.4)$$

after which breakdown occurs. The charge produced by RPC operating in region near the Meek's limit is about 100 pC, this is called streamer operation.

A charge  $Q_0$  that enters the resistive electrode surface 'decomposes' with time  $t$  following an exponential:

$$Q(t) = Q_0 e^{-t/\tau} \text{ with } \tau = \rho \epsilon_0 \epsilon_r; \quad (3.5)$$

where  $\rho$  is the volume resistivity of the material,  $\epsilon_0$  is the dielectric constant and  $\epsilon_r$  is the relative permittivity of the resistive material. The volume resistivity is connected to the conductivity  $\sigma$  by  $\rho = 1/\sigma \text{ } \Omega\text{cm}$ . Typical glass resistive plates have a volume resistivity of  $\rho \simeq 10^{12} \text{ } \Omega\text{cm}$ , leading to a 'relaxation time'  $\tau \simeq 1 \text{ s}$ . The volume resistivity of Bakelite is of the order  $\rho \simeq 10^{10} \text{ } \Omega\text{cm}$ , which gives a 'relaxation time'  $\tau \simeq 10 \text{ ms}$ . The charges in the resistive electrodes cause the high voltage and thus the electric field in the gas gap to drop locally around the initial avalanche or discharge. Here the detector has a blind spot for a time of the order of the relaxation time  $\tau$ , but the remaining counter area is still sensitive to particles.

RPCs may be operated in *avalanche mode* or in *streamer mode*. While in avalanche mode RPCs streamers are an unwanted side effect, streamer mode RPCs make use of the large current pulses induced by the streamers, which simplifies the read out of the device. As the streamer signals are quite large (between 50 pC and a few nC), no preamplification is needed and the signals can be discriminated directly [126]. Double gap chambers operate at electric fields of 40 kV/cm in streamer mode and with 2 mm wide gaps reach efficiencies of 99% but with a time resolution of around 1 ns [127].

In avalanche mode, the increase of the gap width affects both the time performance and the multiplication factor and then the pulse charge distribution of the detector, as in eq. 3.2. The performance becomes poorer at wider gaps, due to the larger fluctuations during the avalanche development. Because the average pulse charges are a factor ten lower than in streamer mode, the avalanche mode allows to operate this device with high but it also makes it necessary to introduce low noise electronics. The statistical distribution of electrons energy, and therefore of  $M$ , in general does not allow one to operate at average gain above  $10^6$  if one wants to avoid breakdown.

In order to avoid that  $M$  exceeds the value fixed by the Raether condition, gas mixtures containing electronegative gases are used. These gases have a very high ionization potential and so they tend more easily to capture free electrons (attachment) rather than to let ionize. In particular have been tested gas mixture with small amounts of sulfur hexafluoride  $SF_6$  which is able to limit the avalanche grow, *saturate avalanche regime operation*. Results show that gas mixture with  $SF_6$  assure operating plateau in pure avalanche mode with detection efficiency  $\epsilon > 98\%$  [125].

RPCs read-out electrodes can be shaped like strips or pads. A long read-out strip can be approximately considered as a signal transmission line, with an end terminated by the front end electronic and the other by means of a proper resistor. The charge induced on the strip divides in two equal parts, and the signal propagate in two opposite directions, and the capacity  $C$  is independent of the strips length.

### 3.4.3 The Multigap Resistive Plate Chambers

The Multigap Resistive Plate Chamber, MRPC, was born in 1996 from an R&D program in the LAA project at CERN devoted to large-area devices, principally for muon detection [128]. The key difference between the MRPC

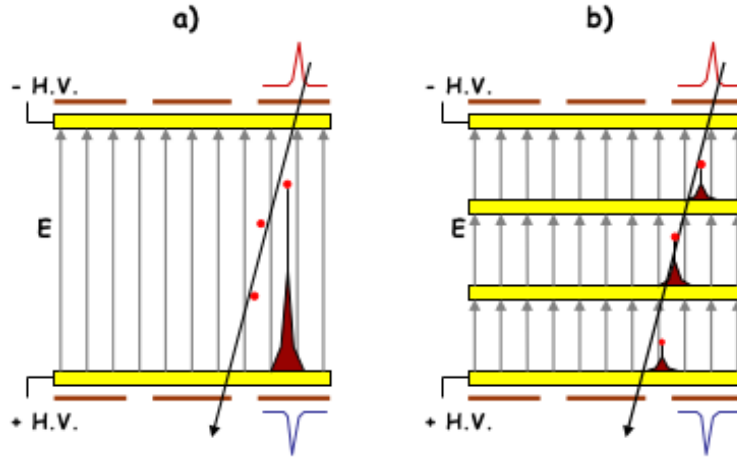


Figure 3.12: Schematic diagram and principle of operation of a Multi-gap RPC (b) compared to a conventional single-gap RPC (a).

and the more traditional single-gap resistive plate chamber is that the multi-gap consists of a series of equal-sized gas gaps all read out with a single set of readout strips or pads. These gaps are created by inserting extra plates of resistive material, generally glasses, in-between the outer resistive plates. An anode and cathode electrode are placed on the outer surfaces of outermost resistive plates and all interior plates are left electrically floating.

They combine the advantages of a wide-gap RPC (high efficiency) with the better time resolution performance of a small-gap chamber. A key issue in the operation of these detectors is the fact that the electric field is high and uniform and therefore the electrons produced by ionization start avalanching immediately; there is no drift time associated. There is also a further advantage of subdividing the gas gap into many small gaps. A through-going particle produces individual and separate clusters of primary ionization; each of these clusters will start an avalanche and the final signal will be the sum of all avalanches.

In a single-gap device, these avalanches are not independent and the resultant signal is as if there was only one large avalanche subject to fluctuations, as in the schematic view of Figure 3.12a. On the contrary, for multigap chambers the signal is truly the sum of independent avalanches, since the avalanches occur in independent sub-gaps, Figure 3.12b. Fluctuations within the avalanche mechanism dominate the single-gap behavior while an average of many avalanches is the resultant signal in MRPCs.

Other main advantages of the MRPC technology are:

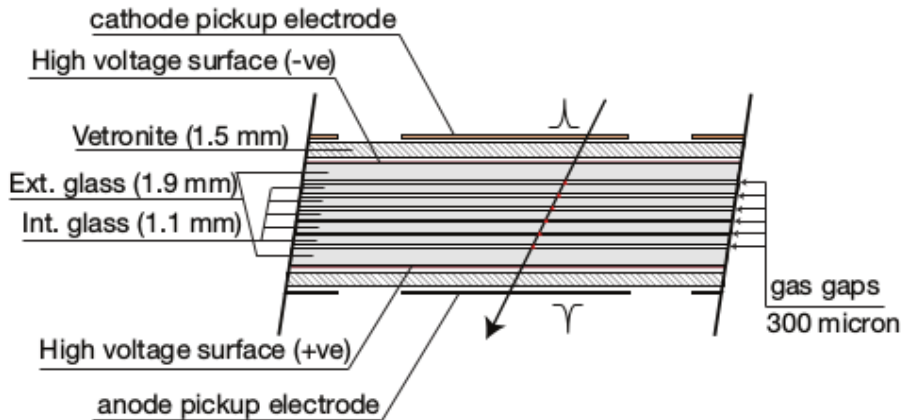


Figure 3.13: Schematic representation of a 6 gap MRPC. A differential signal is obtained by reading out both anode and cathode.

- ◇ the chamber operates at atmospheric pressure.
- ◇ the signal induced on the pickup electrodes by the movement of electrons and ions in the avalanche is the sum of the signals from all gaps. There is no late tail in the time response and the charge spectrum has a peak well separated from zero, thus the setting of the threshold is far less critical with respect to exponential shaped charged spectra.
- ◇ the resistive electrodes quench streamers so that they do not initiate a spark breakdown; this allows for high-gain operation. The stable state has equal gain in all gaps.
- ◇ the construction technique is rather simple and based on commercially available materials.

### 3.4.4 The EEE MRPCs

The tracking telescope of the EEE Project is composed of three MRPCs spaced by a vertical distance of  $\sim 50$  cm, ranging between 40 cm and 1 m, depending of the different stations. A detailed report of the assembly procedure is reported in [130]. Each MRPC consists of a stack of resistive glass plates, with voltage applied only to external surfaces. In the MRPC six gas gaps are obtained interleaving two glass plates of  $164 \times 85 \times 0.19$  cm<sup>3</sup>, with five smaller floating glasses of  $158 \times 82 \times 0.11$  cm<sup>3</sup>, as in Fig 3.13. Commercial nylon fishing line of  $300 \mu\text{m}$  thick is used as spacer between glasses, held tense by plastic screws, mounted along each edge of the vetron-

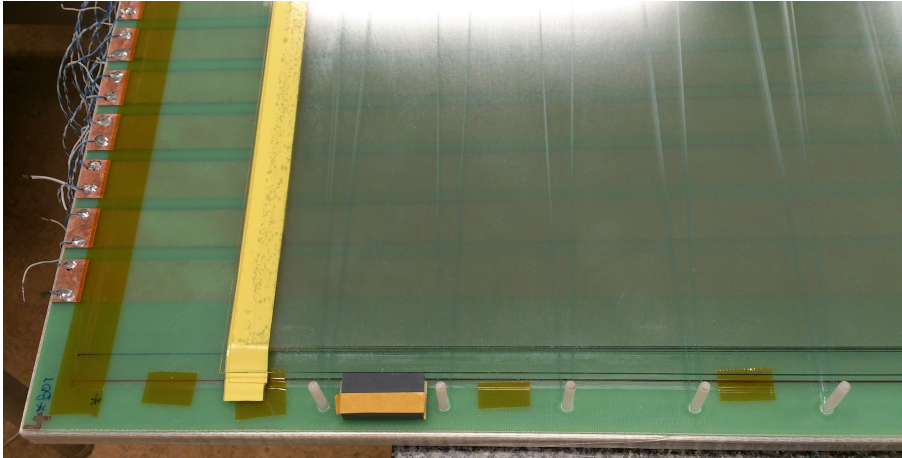


Figure 3.14: The fishing line runs across the surface of the glass, and around the plastic screws along the edges. It creates the gas gap with a width equal to the diameter of the fishing line ,  $300 \mu\text{m}$ .

ite sheet, as shown in Fig.3.14. The outer glasses are coated with a special resistive paint, LICRON 1<sup>3</sup>. It comes as an aerosol and can be sprayed by hand. The resistive paint allows a volume resistivity of  $\sim 10^{13} \Omega\text{cm}$ . The outer glasses act as high voltage electrodes, while the inner ones are left electrically floating. The glass plates are transparent to the signals associated to the avalanches generated inside the gas gaps: they terminate the avalanche development in each gap, and act as dielectric plates for the fast signal produced by the movement of electrons in the gas avalanches. The induced signal is the sum of all gas avalanches in any of the gas gaps. Two vetronite panels are mounted on both sides of the stack of glass plates with an area is  $90 \times 180 \text{ cm}^2$ , Fig.3.13. A mylar film ( $175 \mu\text{m}$  thick) is placed between each vetronite sheet and the outer glass plate. The high voltage connections, the anode and the cathode of the MRPC, are applied to each outer glass, at the opposite side, and are made by a copper tape with a small pad of carbon tape, that is directly put between the Licron coating and the vetronite panel. The mylar film is cut out in that point, in order to create some space for the connections, Fig.3.15. Each of the two vetronite sheets insulates 24 copper strips from the anode and the cathode, respectively. This readout strips are obtained applying a self-adhesive copper tape, on the vetronite, as shown in Fig.3.16. The copper tape is 2.5 cm wide, a 0.7 cm gap is left between the strips, so the pitch of the readout strips is 3.2

<sup>3</sup>Licron, Permanent Static Dissipative Coating 1756, <http://www.techspray.com/>

cm wide. Consequently, a transmission line is created for the anode and the cathode side both, bringing the induced signals out to the shorter edges of the MRPC. A twisted pair cable is soldered to the anode and cathode readout strips; thus a differential signal is transmitted from the MRPC via this cable connected to the inner surface of the front-end card mounted at the two ends of the chamber.

Two honeycomb panels, 15 mm thick, is attached to the two vetronite sheet using double-sided adhesive tape. They ensure the structure which is then enclosed in an aluminum box (1m x 2m x 5cm) equipped with standard gas connectors, The aluminium box is eventually sealed to make a gas-tight enclosure.

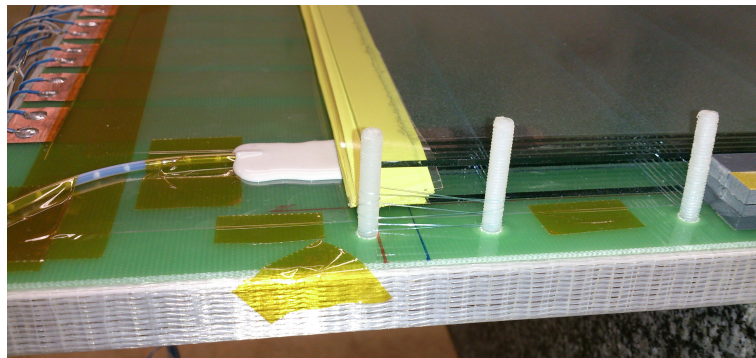
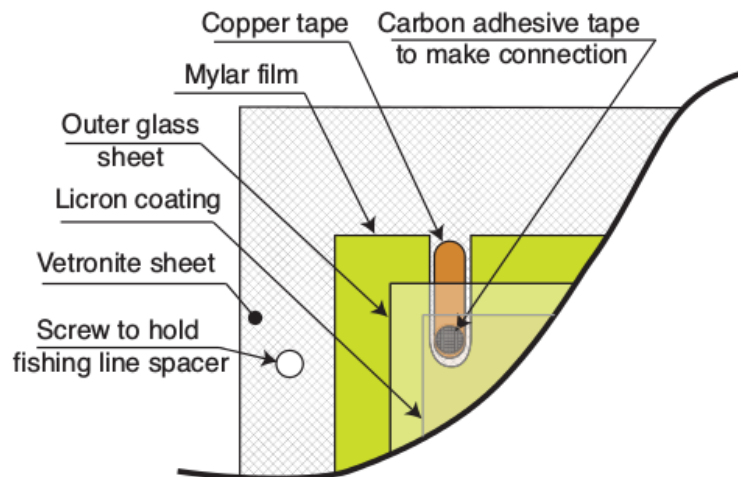


Figure 3.15: *Up*: Corner area diagram of a MRPC with the high voltage connection to the Licron coating. *Down*: Picture during the MRPC assembly showing the glass stack and the h.v. connection.

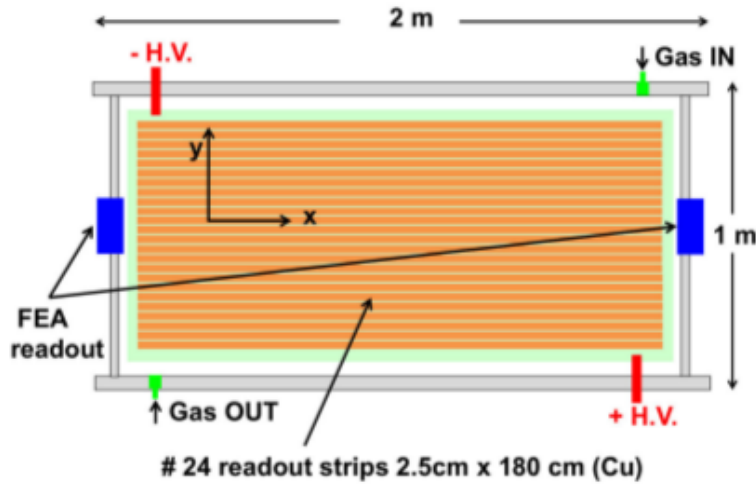


Figure 3.16: Readout copper pads on the Vetronite.

## 3.5 The EEE Cosmic-Ray station

### 3.5.1 Gas System

The gas mixture is continuously fluxed inside the chambers with a gas flow of about 3 l/h at atmospheric pressure. Since EEE stations operate in high schools, particular attention has been put on safety issues, gas mixture does not have to contain any flammable component, and the detector has to operate at atmospheric pressure. For this reasons, isobutane, which is routinely used with this kind of chambers is removed from the mixture. The MRPCs are flushed with a 98% of  $C_2H_2F_4$  (R134A) and 2% of  $SF_6$  gas mixture, to enhance streamer-free operation in the gap between two resistive plates.

The chambers operate in avalanche mode with a typical operating voltage around 18 kV supplied by appropriate DC/DC converters.

The choice of the  $SF_6$  fraction has been worth considering, in fact with its increasing competing processes affect the MRPC characteristics [131]. To raise the efficiency plateau, higher electric fields are required with increasing fractions of  $SF_6$ , which also increases the drift velocity and results in an improved time resolution. On the contrary, since  $SF_6$  has large capture cross sections for low energy electrons, increasing the  $SF_6$  concentration reduces the growth in the avalanche significantly. This leads to a reduction in the MRPC counting rate and efficiency, and a worsening in the time resolution.



Figure 3.17: The Front-End Analogue (FEA) card with the NINO ASIC chips.

### 3.5.2 Front-End electronics

The signal initiated by a charged particle traversing the detector is induced on the readout copper strips and proceed to both ends of the MRPC, from the anode and the cathode strips as differential signals. They are transmitted, by means of twisted pair cables to the two front-end cards, mounted at the ends of the MRPC. There are 6 Front-Ends Analog card - FEA card - two for each MRPC, the *right* side and the *left* side: see Fig.3.16.

Each FEA card is equipped of 24 channels, one for each readout strip, and hosts NINO ASIC (Application Specific Integrated Circuit) chips for the MRPC signals [132]. The NINO ASIC chip, developed for the ALICE TOF MRPC-strip detector, is an ultra fast front end preamplifier/discriminator, fabricated with  $0.25\ \mu\text{m}$  CMOS technology. It has 8 amplifier and discriminator channels, thus tree chips are necessary.

Each channel is designed with an amplifier with  $< 1\ \text{ns}$  peaking time, a discriminator with a minimum detection threshold of  $10\ \text{fC}$ , and an output stage. Each channel in the NINO ASIC chip takes differential signals from the pickup strips as input, and amplifies them in a four stage cascade amplifier. The NINO ASIC encodes the charge of the input signal into the width of the output signal, with a minimum output width of  $6\ \text{ns}$ . The threshold to the chip's discriminator stage can be adjusted between  $157\ \text{mV}$  and  $250\ \text{mV}$ , by means of a trimmer in the FEA card. Each FEA provides an OR signal between all the differential signals from the 24 readout strips, for the trigger purpose. It also collects the output signals from the 3 NINO chips and connects them, through 2-5 meters long 24-pairs Amphenol cables, to the

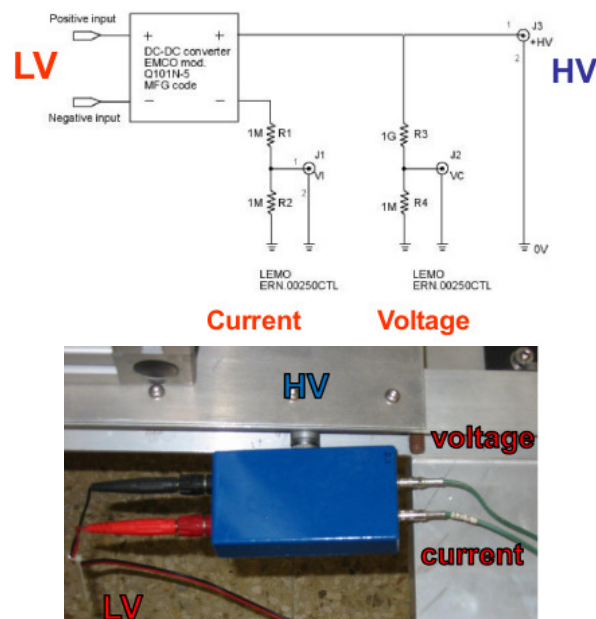


Figure 3.18: DC-DC converters voltage dividers scheme.

multi hit Time to Digital converters (TDC). Thus the signal *leading/trailing edges* width, measuring by means the TDCs, is correlated to the charge of the input signal, and no further readout electronics is needed to measure the charge. Measuring this width, the *Time Over Threshold* width, allows the correction for time slewing without the need for an ADC [ref:performance].

### 3.5.3 High-Voltage system

The high voltage up to 20 kV in the EEE MRPCs is applied by means of two proportional ultra-miniature DC/DC converters [134]. One, the *positive*, delivers up to 10 kV, and the other one, the *negative*, produces down to -10 kV, for an input voltage both in the range  $[0 \div 5]$  V and a proportional gain of about 2k. The two DC/DC converters are directly mounted onto both side of each MRPC: therefore no high-voltage cables are needed.

It is possible to monitor HV and current supplied to MRPC through two voltage dividers located in DC/DC converter's boxes. The scheme of this circuit is shown in Fig.3.18. for the DC-DC converters and for the MRPCs front-end cards. The remnant stations use standard desk power supply.

A brief description of Voltage Control System's circuit, block diagram



Figure 3.19: LV/HV control system graphic interface. 1. LV to DC/DC converters; 2. the module's status; 3. HV and currents from MRPCs; 4 Temperature of the NI board and voltage from FE boards.

and main components is reported in Appendix A and in [133].

The main component of the circuit is the Data Acquisition (DAQ) module [135], which is interfaced to a PC through a standard USB port and it is controlled by a dedicated software in LabVIEW platform [159]; its graphic interface is shown in Fig:3.19.

Through this voltage control system it is possible:

- ◇ to set both low voltages to 6 DC/DC converters  $[0 \div 5]$  V and 6 FE boards  $[2.5 \text{ V}]$  Fig:3.19(1);
- ◇ to check the LV/HV control system status Fig:3.19(2);
- ◇ to monitor on the HV and current in the MRPCs Fig:3.19(3);
- ◇ to monitor the temperature of the DAQ board and sense voltage in the FE boards Fig:3.19(4).

Since the computer in the EEE laboratories is permanently online, the LV/HV system can be continuously monitored from remote. Monitoring contemporaneously the MRPCs, especially in an environment such different from a scientific laboratory, is needed to keep under control the efficiency detectors and to be sure their performance remains stable in time.

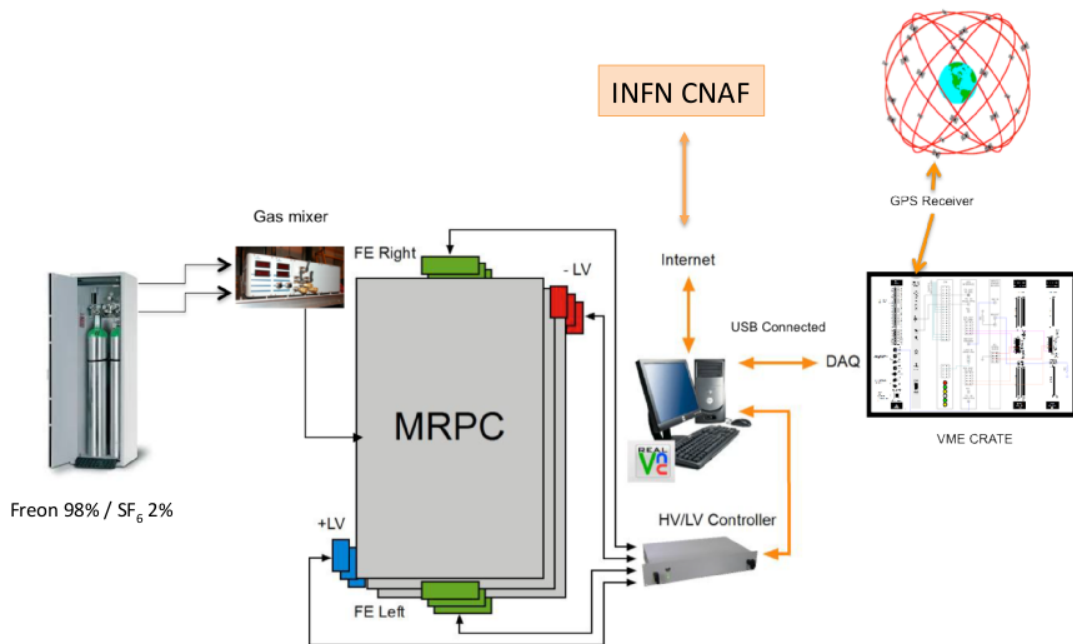


Figure 3.20: A schematic design of the DAQ system in a EEE station.

### 3.5.4 The Data Acquisition system

The data acquisition system of the EEE telescope is based on the VME standard. Each station of the EEE Project (EEE station) is equipped with a VME Crate who supplies the VME modules:

- ◇ VME *bridge* CAEN V1718: the data acquisition is controlled by a LabView program running on a PC connected to the VME crate via a VME *bridge*, through a USB standard port.
- ◇ Two multi-hit TDCs CAEN V1190A-V1190B: the differential signals from 144 channels (24 channels from each FEAs, a *left* and a *right* ones for each MRPC) are fed into two TDCs module, V1190A with 128 channels and V1190B with 64 channels.
- ◇ Trigger board: one or more modules generate the data acquisition trigger.
- ◇ EEE Clock Distribution & Trigger shape cards (*Clock Card*): the card improves the time performance of the EEE telescope, allowing the synchronization of the internal clock of the two TDCs.

The DAQ system schema is shown in Fig:3.20.

When a charged particle passes through the EEE telescopes and generates a signals in the MRPCs, discriminated and amplified by the NINO amplifiers, the FEA card forms an OR-signal from the 24 readout strips. From the FEA this six differential signals (LVDS) are collected and elaborated by a trigger card, and a six-fold coincidence of both FEA of the three MRPCs generates the data acquisition trigger, it is described in the next section. The impact point of the particle in each chamber, is reconstructed by means of the hit strip in one direction ( $x$ ) and by the difference of signal arrival time at the strip ends, the right and the left sides, measured by two multi-hit TDCs in the other direction, Fig.3.16.

The absolute time of each event in the EEE telescope is recorded and synchronized by means of Global Positioning System modules, in order to get the event time stamp in UTC time, and to correlate the information collected by different telescopes. Three different kinds of GPS receivers are used in the EEE station:

- *HYTEC VME*, the older, placed in the VME Crate and connected to the trigger board by means a GPS-Interface board [136].
- *Spectracom TSync GPS* placed directly in the school's PC and connected via a PCI bus. The time information is read by the LabView software.
- *GPS TRIMBLE SMT 360* - a new trigger card has been developed, with an embedded engine GPS for timing application to implement the event time stamping at level of the trigger card.

The EEE telescope is also provided with a weather station (Oregon Scientific) able to measure outdoor and indoor temperature and pressure. Data from the weather stations are also integrated into the binary output files in order to correct the collected data for meteorological effects.

### 3.5.5 Trigger system

The DAQ of the EEE system is built around the USB-VME unit. It is not possible to read data synchronically at each trigger, using a VME bridge, because the USB cycle time limits the VME reads imposing an unacceptable dead time on the system; thus the data are read out asynchronously.

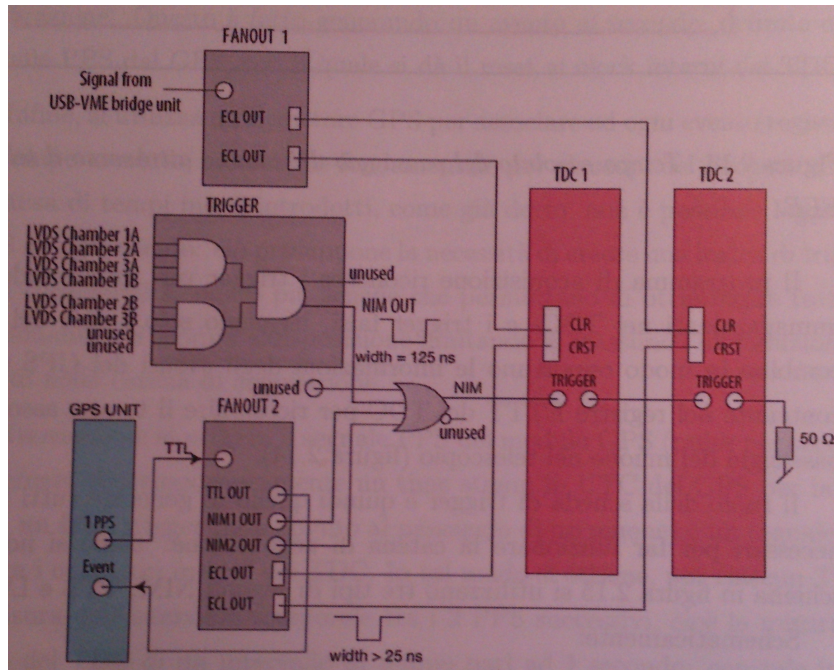


Figure 3.21: Block diagram of the trigger card.

Due to the same dead time considerations, one can not read the data from GPS module every event.

The GPS unit provides the *one pulse per second* - 1 PPS - which is used to create a time stamp and to reset the internal counters of the TDCs. Every time an event trigger occurs, the trigger board fed into each TDC a ECL signal, and the TDCs put data into their FIFO. The TDCs have internal 40 MHz clock, and two counters are combined together - the *bunch counter* (25 ns LSB and 12 bits), and *extended time tag* - ETT (800 ns LSB and 27 bits) - to form one time offset with respect to last GPS time stamp. Additionally since the two TDCs have independent clocks, they are also calibrate by means of the PPS. The LabView DAQ system running on the PC has to sort out and put the data from the two TDCs into single events and also read out the GPS unit at appropriate times and insert the GPS values within the data stream at correct place. The absolute time of an event is this time offset plus the GPS time stamp (each PPS). The difference between the two bunch counters of the leading edge from the right and left sides of each MRPC are used to reconstruct the hit position along the strip.

The role of the trigger card is to create all the signals needed by such a

system, the block diagram is shown in Fig:3.21.

- ◇ At the start of the data acquisition the trigger card receives a NIM/TTL signal from the VME-bridge, converts it to ECL that is fed into the two TDCs. These are the *CLEAR* inputs which ensure that the buffers of both the TDCs are cleared, the event numbers are zeroed and they match up in the data from the two TDCs (Fanout 1 in Fig:3.21).
- ◇ The trigger forms the 6 fold coincidence of the strips OR output from the two sides of the tree MRPC (Trigger in Fig:3.21).
- ◇ When the trigger card receives 1PPS signal from the GPS unit, it generates a TTL signals the is fed back to the GPS unit - this will generate a time stamp in the GPS memory that can be later read-out. The two ECL outputs are delayed by  $\sim 1.5 \mu s$  and used to reset the counters (bunch id and ETT) in the TDCs, *Clear reset* - CRST-signals. Two NIM outputs are also generated, NIM1 in time with the input from the GPS, NIM2 delayed by  $\sim 1.5 \mu s$ . They are connected to the TDCs, where they generate two empty events, delayed by  $1.5 \mu s$ . This time jump in counter values is recognized by the DAQ system that will then read out the GPS time and insert a *GPS event* into the data stream. (Fanout 2 in Fig:3.21).

### 3.5.6 Data processing and data quality monitoring

The data-processing infrastructure for the EEE experiment is provided by CNAF (*Centro Nazionale Analisi Fotogrammi*), the central computer facility of the Italian National Institute for Nuclear Physics (INFN) and one of most prominent centers for distributed computing in Italy. The data acquisition is organized in units (or *runs*) of 50,000 events each corresponding to 15-30 minutes of data taking, depending on the acceptance and efficiency of the telescope. During periods of coordinated data acquisition, the DAQ systems are running continuously under the direct supervision of the students and professors. Data are automatically transferred to CNAF from each of the schools participating in the project and processed in near real time (few hours) on a dedicated machine.

For each run the track reconstruction is performed: The hits on the chambers are selected as particle events by means of the variable  $\chi^2$ : the quadratic sum of the three-dimensional distances between the hit position and the best

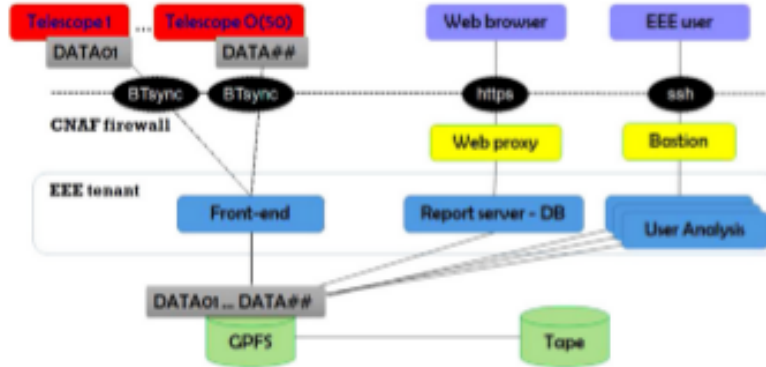


Figure 3.22: The general architecture for the EEE data flow at CNAF.

fit track. The track reconstruction method at CNAF is reported in section 4.1. The impact time in each MRPC is reconstructed as the average of the signal arrival times at the strip ends (*left* and *right*), see section 4.5.

A data summary tape (DST) in ROOT [137] format is created for calibration and science analysis purposes. All the bookkeeping is performed via a dedicated MySQL database. Run-by-run and daily summary reports are also automatically produced for each telescope and made available through a central web interface by the data-processing pipeline, Fig.3.23.

### 3.5.7 The coordinated data acquisition

For the first time at the end of 2014, the EEE telescope network tested a simultaneous and completely automatic acquisition and data storage at the central computer facility of the INFN, the *Centro Nazionale Analisi Fotogrammi* CNAF [140]. At present all the network station data are transferred and stored at CNAF, where events are analyzed and particle tracking procedure is implemented. The PC of each EEE station is connected by means of a BTsync client [141], a peer-to-peer software to synchronize data folders in real time.

In November 2014 a first coordinated data taking, Pilot Run (2 weeks) was performed, with several telescopes running simultaneously. Afterwards a large number of telescopes of the EEE array participated in Run1 (45 days), which lasted from February to April 2015. The second combined data taking, RUN2, started in October 2015 and lasted until end of May 2016, with 40 telescopes involved and 15 billion of events collected. The

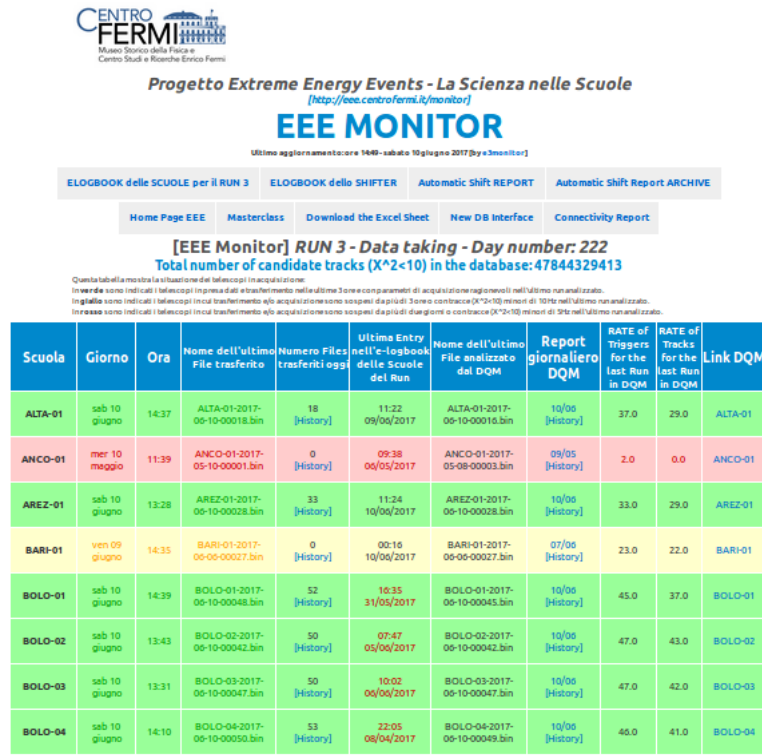


Figure 3.23: Web interface for the automated DAQ report from the EEE telescope array data transfer at CNAF.

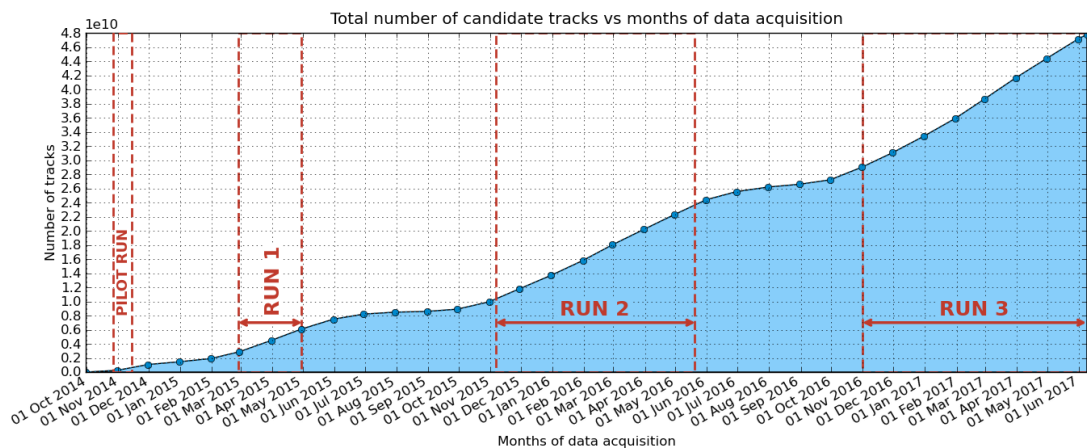


Figure 3.24: Total numbers of candidate tracks collected at CNAF [138]

current run, RUN3, started at the end of October 2016 and will continue until May 2017. Up until now the EEE network of telescopes has collected

more than 30 billion of cosmic tracks, as reported in 3.24.

### 3.6 The EEE Project physics research Program

Results from the recent coordinate data acquisition, on main topics such as EAS detections and studies of the cosmic ray flux, have been reported in [144], [145], [146], [148].

The analysis activity is currently in progress and focused on several items like coincidence searches, time variations of the muon flux, East-West asymmetry, cosmic ray anisotropy [ref:chapter-anisotropy], upward-going particles, observation of the moon shadow. Here we report briefly the most recent results.

#### 3.6.1 Extensive Atmospheric Showers Detections

The telescopes relative distances of the EEE network are ranging from a few hundred meters for clusters of 2, 3 and 4 telescopes in the same city, to more than 1000 km for the farthest stations. Particles from the same EAS can be detected as coincidences by stations some kilometers apart. The EAS detection is a main goal of the EEE scientific program, and a systematic study on the number of coincidences detected by pairs of EEE telescopes is extensively investigated [149], making use of Monte Carlo simulation programs (like CORSIKA) e.g. to compute the expected numbers of coincidences as a function of the distance between the two sites [139].

The distribution of the time difference  $\Delta T$  between the events time stamp from two telescopes  $>0.5$  km far away, for the Cagliari and Frascati sites, are shown in Fig 3.26, and 3.25. The coincidence peak due to particles belonging to the same EAS stands out on the background of accidental coincidences. The Signal is the area of a Gaussian fit within  $\pm 1 \sigma$ , whereas the Noise level is defined as the flat background, dues to accidental coincidences, within an equal time window  $2\sigma$  wide.

From all measurements it is evident that the coincidence rate diminishes as the distance between the telescopes increases, as expected: from a certain distance on, to distinguish the signal among the background level is mandatory to collect big data samples, thus, to operate the telescopes with the maximum duty cycle possible. Figure 3.25 shows the first detection of

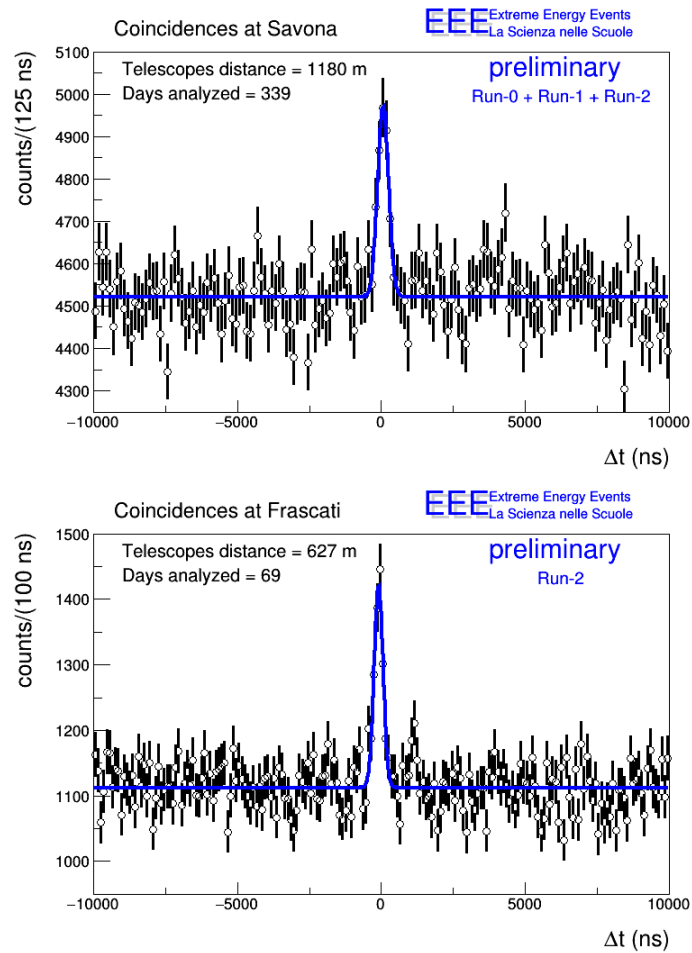


Figure 3.25: Observations of coincidences peak between stations in Savona - *top*, and in Frascati - *bottom*.

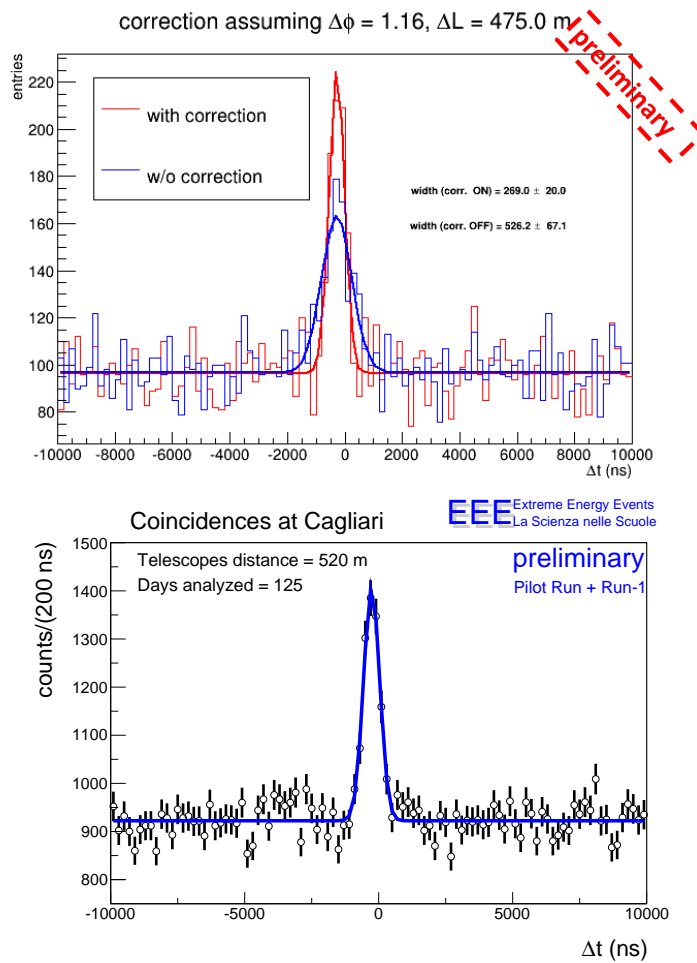


Figure 3.26: Observations of coincidences peak between stations in Cagliari - *on top*: first results with and without corrections - *on bottom*: most recent results (with correction).

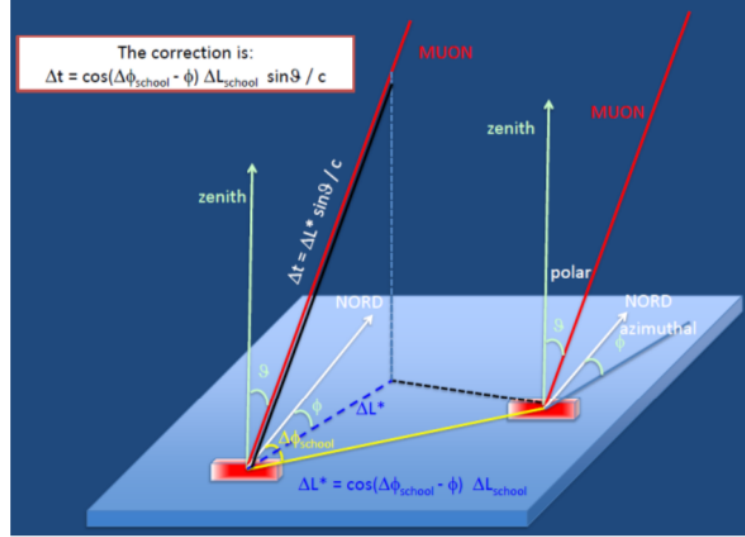


Figure 3.27: Graphical representation of muon from the same EAS, impinging two EEE telescopes. The time difference  $\Delta T = T_1 - T_2$  depends on the distance between the stations, on the polar angle  $\theta$  the EAS axis and on the angle  $\theta$  the EAS axis and the line connecting the two telescopes

coincident events, data from PilotRun+Run1+Run2, obtained between two telescopes in Savona where the distance of is about 1.2 km.

To achieve the result shown, a careful investigation of techniques for effectively rejecting the background of accidentals has been exploited. The arrival time difference of particles in the same EAS depends on the axis shower direction. EEE telescopes can detect the direction of the shower secondaries. Such a feature allows to correct, event by event, the time delay between two telescopes because of the propagation of the wave front of the shower. Under the approximation of flat shower front, the time difference depends on:

$$c\Delta T = \Delta L^* \sin\theta \quad \text{where} \quad \Delta L^* = \cos(\Delta\phi_{school} - \phi)\Delta L_{school} \quad (3.6)$$

$\Delta L_{school}$  is the distance between the different stations;  $\Delta\phi_{school} - \phi$  the angle if the EAS axis and the imaginary line joining the two stations (so the azimuth angle between the station and the North) as reported in Fig.3.27. This correction is very important when looking at coincidences at very large distances, since above 1 km the time delay may be of the order of few microseconds.

The Signal/Noise ratio can be further improved by selecting events where

tracks have a small relative angle, because most of muons belonging to the same EAS arrive with an orientation near the shower axis.

In the High Energy EAS research among faraway telescopes, the corrections of the time intervals for distances reduce background due to accidental coincidences, they increase the signal to noise ratio, and decrease the  $\sigma$  of the coincidences peak, as in Fig.3.26. The width of the coincidences peak is indeed proportional to the relative distance between the telescopes because of the spread in the muon paths.

### 3.6.2 Study of Cosmic rays flux

The EEE telescopes is a tool able to monitor the cosmic-ray flux, with a selective sensitivity to the muon component. The high sensitivity of the telescopes allows to detect small fluctuations of the local muon flux, e.g. due to meteorological effects or to non-periodic solar phenomena. Thus the network can detect the Galactic Cosmic-Ray flux Decreases GCRDs, associated to solar phenomena as Coronal Mass Emissions and solar flares- the *Forbush decreases* [152]. The GCRD monitoring is of interest for the understanding of phenomena that occur on the solar heliosphere, as well as on other observable stars. The effect on the solar wind directly affects the measured galactic cosmic ray flux on Earth, giving typical flux fluctuations of a few percent on a few days basis (see 1.7).

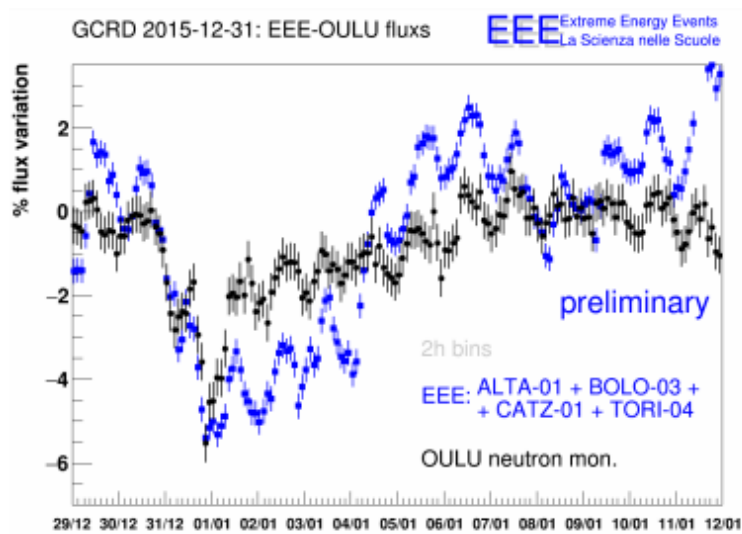


Figure 3.28: GCRD on the date 31-12-2015 - muon decrease observed with 4 EEE telescopes, compared to neutron rate from the Oulu station.

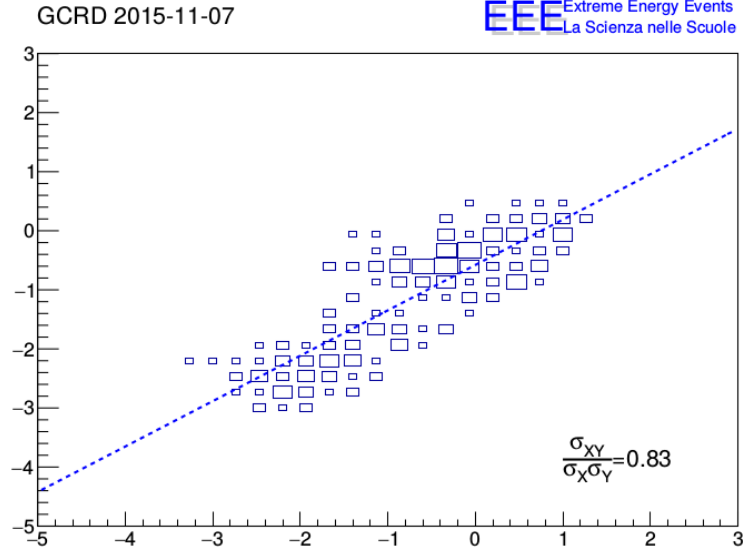


Figure 3.29: The plot shows the excellent correlation between OULU and EEE percentage flux variation [152].

Local values of temperature and pressure influence both cosmic rays flux at the sea level and gas density in the MRPC, as it is reported in section 1.10. The measurement of few percent secondary particle flux variations requires a set of corrections in order to cancel out systematics which may mask GCRDs. They are mainly coming from the absorption phenomena which occurs in atmosphere to the EAS shower development to the ground. This effect is related to the cosmic ray interaction length in atmosphere [146]. The secondary particle intensity  $I$  can be approximated with the relation 1.35 thus consider the first order correction:  $\Delta I = -\beta \Delta P$ .

Each MRPCs telescopes is provided with a weather station able to measure temperature and pressure outdoor and indoor. Also this local values, acquired together with the telescopes data, are transferred to CNAF. The muon rates  $R_{measured}$  in each telescope need to be normalized to the effective rate  $R_{eff}$  (to a reference pressure  $P_0$ ) by means of a barometric coefficient  $\beta$  evaluated in each different environment:

$$R_{eff} = (1 - \beta \Delta P) R_{measured} \quad (3.7)$$

The MRPCs particle rate is normalized applying a barometric coefficient evaluated in each station, and the high sensitivity of the telescopes allows to detect this rapid variations,  $\sim 5\%$ , behaving as a solar monitor array with

wide coverage and with precise timing.

The EEE network observations are generally highly correlated with neutron monitor stations, as in figure 3.29, although these are more sensitive to low-energy primaries, showing usually lower energy threshold than EEE muon tracking detectors. Muons detected in the EEE telescopes originate from events of higher energy in the atmosphere: this feature explains the different amplitude of the decreases when observed by NM. A GCRD, observed during the Run2, is shown in figure 3.28 in comparison with the Oulu Neutron Monitor data.

The GCRD survey through the EEE telescope array, because of its selective sensitivity to the muon component, the higher rigidity cutoff and the broad longitude/latitude and altitude coverage proves to be a complementary instrument w.r.t. to NM, allowing comparisons and the extraction of new GCRD features.

### 3.6.3 Upward-going events

The MRPCs telescope can provide the event Time of Flight, between the bottom and the top chambers, the particle track length, and thus a rough value of the particles speed  $\beta$ . Upward going events can be discriminated from downward going by mean of the  $\beta$  value. Upward going events are observed in EEE telescopes, as a population of  $\sim 1/2000$  of the downward going particle detected. Most of them could be explained as relativistic electrons

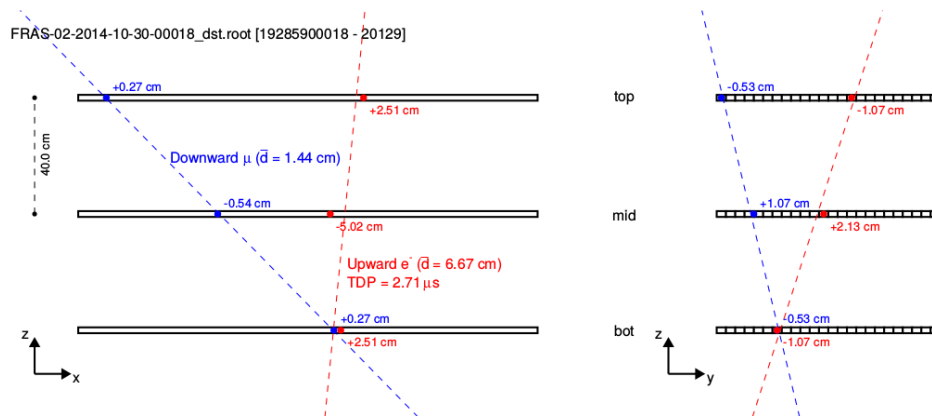


Figure 3.30: Event display of two tracks, separated in time by  $\sim 2.7 \mu\text{s}$ . The downward-going candidate muon (in blue) and the upward-going candidate electron (in red).

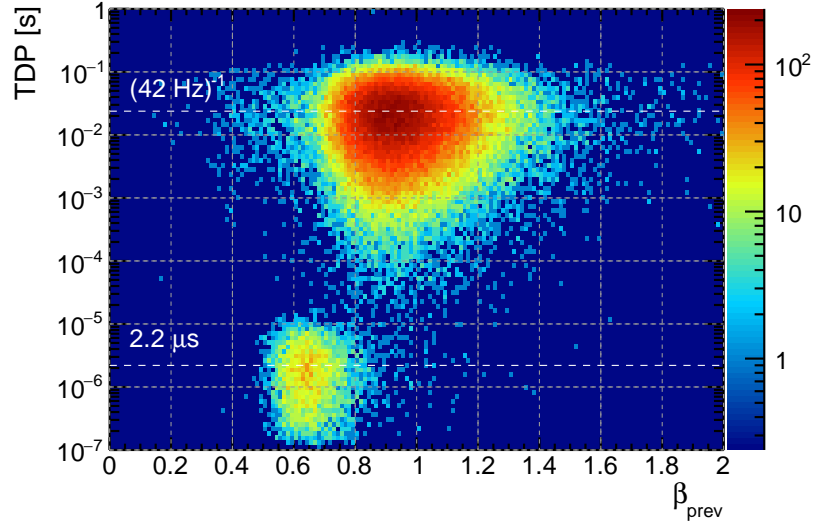


Figure 3.31: Distribution of the delay between the upward track and the previous downward event –TDP vs  $\beta$  of the previous event. The telescopes rate is  $\sim 42$  Hz.

coming from the muon decay. A fraction of them can be generally highly correlated with a “parent” muon passing through the telescope by means of the time delay respect to previous events [151]. As shown in figure 3.30 a downward going parent–muon stopping in the bottom chamber, or in the ground below it, decays. It generates an upward going electron–daughter, that triggers the chambers. The two events are discriminated in time with a delay equal to the muon lifetime  $\tau \sim 2\mu\text{s}$ . In figure 3.31 the up going electron–daughter time delay, the Time Difference to the Previous event (TDP) vs the parent–muon  $\beta$  are plotted. As expected, the parent–muon energy is lower than non–correlated events energy.



## Chapter 4

# Performance of the EEE MRPC telescopes

The study of Extensive Air Showers, and in particular the angular distribution requires excellent performance in terms efficiency, tracking capability and stability. The data from two recent coordinated data taking periods, from the Run 2 and Run 3, have been used to measure these quantities and the results are described, together with a comparison with expectations and with the results from beam test performed in 2006 at CERN.

### 4.1 Track reconstruction

Data reconstruction is centrally managed at CNAF, section 3.5.6.

Raw data are first processed to calibrate the telescope. Each readout channel has indeed a time offset which slowly drift in time, mainly in relation with temperature. The drift is very slow and can be assumed constant within a single run of  $\sim 1$  h. For each channel, the two channel for each strip, *left* and a *right*, the mean arrival time (named  $t_l$  or  $t_r$  depending on the strip side) of the signal w.r.t the trigger is computed and a realignment in time is performed, the *mean strip* correction in 4.5. Once the calibration matrix has been computed real reconstruction is started. Signals registered on both side of the same strip are paired to form a hit point. Transversal coordinate is given by the strip number, while the longitudinal coordinate is given by the difference in the arrival time of the signal to the two chamber side. A time is also assigned to the hit, computed as the mean of  $(t_l + t_r)/2$  and thus independent from the hit position. A first cut is then applied to exclude non

physical hit by constraining the longitudinal position and the time of the hit: only those hits whose timing information (from TDC) is compatible with a point whose coordinates are included in the strip geometry are selected. After all hits are reconstructed clusterization of close hits is done.

In several cases in the trigger event, only a single strip is involved and the cluster size is equal to 1; for events which produce a signal in two or three close strips, a cluster is built, whose centre is the average position of the fired strip. Hits (named 1 and 2) are clusterized if some requirements are met:

- hits are on adjacent strips
- the differences  $\Delta t_1 - \Delta t_2$ , where  $\Delta t_{1,2} = t_{l1,2} - t_{r1,2}$ , is below 2 ns
- the hit time difference  $t_{h1} - t_{h2}$ , where  $t_{h1,2} = \frac{t_{l1,2} + t_{r1,2}}{2}$ , is below 2 ns

Finally track reconstruction is performed. The cluster coordinates are fed into two independent unweighted linear fits to triplets of points for each combination of three hits in the top, middle and bottom chambers in the two orthogonal  $XZ$  and  $XZ$  views. The two fits are then combined to provide the best-fit track parameters and a corresponding variable  $\chi^2$  computed. The  $\chi^2$  is defined as the quadratic sum of the three-dimensional distances  $r$  between the cluster positions and the best-fit track,

$$\chi^2 = \sum_{i=1}^3 \frac{r_i^2}{3}, \quad (4.1)$$

i.e., between the director cosines and the track intercept with the middle MRPC plane (the index  $i$  in the sum is running over the three MRPC planes). An average of the  $\chi^2$  contributes both, is used as an indicator of the fit quality.

When all candidates have been identified they are ordered by their  $\chi^2$ . Starting from the best candidate (lower  $\chi^2$ ), all the other candidate tracks sharing an hit point with it are excluded, then the process continues with the second best track and so on. At the end a set of tracks with no hits in common are defined and transferred to the output file for analysis.

The track selection for the measurements presented in these studies is done by requiring  $\chi^2 < 10$  (experimental cut), track quality checks are also applied, to consider only those tracks which have a correct time of flight between the top and bottom chambers and a correspondingly correct track

length. The average cluster multiplicity in these cases is one cluster per plane for 88% of the events. In Figure 4.1 a typical  $\chi^2$  distribution is presented, peaks are due to  $\chi^2$  contribution of the plane YZ, because only few value are allowed by the distances  $r$  between strips. In Sec. 4.6.1 a few quantities

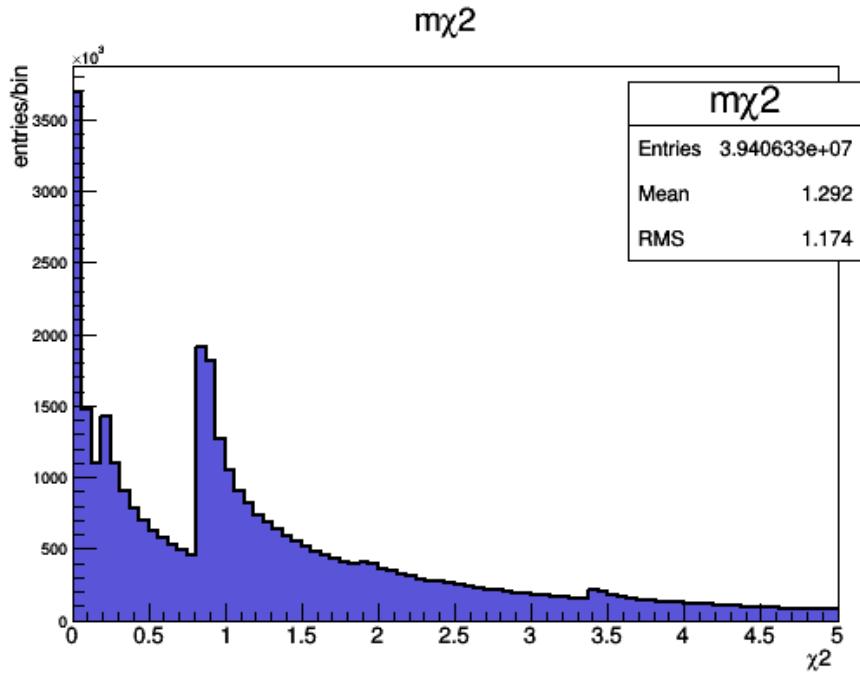


Figure 4.1:  $\chi^2$ -distribution for CAGL-02 tracks, peaks are due to the strips segmentation.

related to the tracking are presented in order to show the stability of the system.

## 4.2 The single MRPC performance

The performance of a single MRPC was measured at the CERN Proton Synchrotron facility. A detailed report of the set-up and the beam-test results has been already described in [142]. The chamber efficiency vs high voltage was measured, with the value at plateau reaching 100%. Time resolution, obtained as the  $\sigma$  of the strip mean time distribution, is 142 ps, without corrections. A value of 100 ps can be obtained, implementing time slewing corrections, see paragraph 4.4.1, and of 70ps with additional corrections for pulse width, and taking into account the scintillators time jitter.

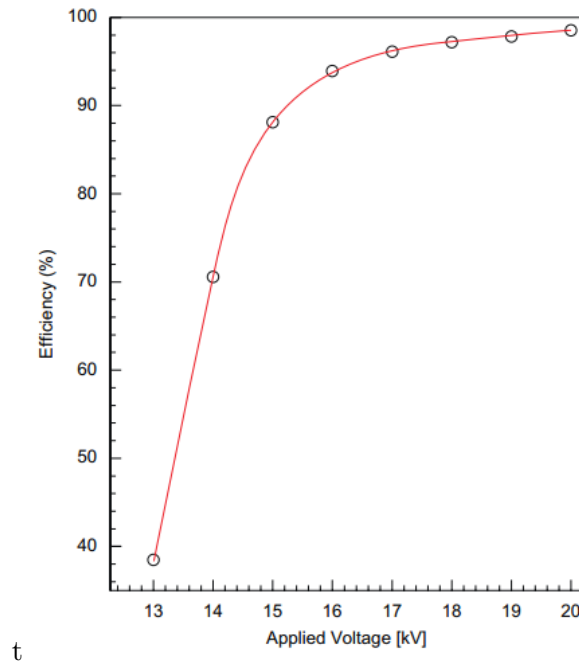


Figure 4.2: Efficiency vs. HV, test beam.

Spatial resolution, measured along the strip length, the longitudinal chamber side, by two TDCs is 94 ps, that corresponds to a resolution of  $\sim 8$  mm.

### 4.3 The telescope performance measured using cosmic rays

A sample of  $\sim 20 \times 10^9$  tracks collected during the Run 2 and Run 3 was used to measure time and spatial resolution of the MRPCs.

In the study of the time resolution, the events collected in TORI-03, PISA-01 and TORI-02 were selected in the Run 2 sample. The main feature of the selected telescopes is the common clock distribution to the 2 TDC boards, provided by a dedicated card. In Run 3 the clock distribution card has been installed in all the other EEE telescopes and this allows to perform the measurement with a complete set of telescopes and compare the results with Run 2 data. A complete comparison between the spatial resolutions during the Run 2 and the Run 3 has been carried out, from most the detectors of the array.

## 4.4 Time resolution

Fig. 4.3 shows the  $\Delta t_{hit}$  distribution of TORI-03 (Run 2 data); the distribution is fitted with a gaussian function and gives as a result  $\sigma_{\Delta t} = 243$  ps. Considering the 3 chambers, the final result on the time resolution is  $\sigma_t = 210$  ps. The analysis performed on PISA-01 (the other telescope in Run 2 equipped with the board to deliver the same clock to both TDCs) gave as a result  $\sigma_t = 270$  ps. It is worth noting that the *time slewing* correction is not applied in this case, as the analysis performed on the Run 3 data does (see the next paragraph).

The main limit for the time resolution depends on the time bin (100 ps) of the TDCs that provide the signal arrival time measurement. The *Good* track events ( $\chi^2 < 10$ ) are reconstructed at CNAF, and the hits on the chambers are selected as particle events. The impact time in each MRPC is reconstructed as the average of the signal arrival times at the strip ends as explained in section 4.1. The study of the time resolution  $\sigma_t$  has been performed by measuring the time information on the upper and lower chambers and use these values to determine the expected time on the middle chamber; this value is then compared with the hit time measured on the middle chamber. The width of the obtained distribution will be proportional to the time resolution of the telescope. The formula used to get this time distribution is:

$$\Delta T_{hit} = (T_{Top} + T_{Bot})/2 - T_{Mid} \quad (4.2)$$

Fig. 4.3 shows the  $\Delta T_{hit}$  distribution of TORI-03 (Run 2 data); the distribution is fitted with a gaussian function and gives as a result  $\sigma_{\Delta T} = 243$  ps. Considering the 3 chambers, the final result on the time resolution is  $\sigma_T = 210$  ps. The analysis performed on PISA-01 and TORI-02 (the other telescope in Run 2 equipped with the board to deliver the same clock to both TDCs) give similar results  $\sigma_T = 207$  ps,  $\sigma_T = 230$  ps respectively. It is worth noting that the *time slewing* correction is not applied in this case, as the analysis performed on the Run 3 data does.

### 4.4.1 *Time slewing* corrections

The readout electronics used in the EEE project [132] is such that the measured hit time is given by the time when the signal becomes larger than the

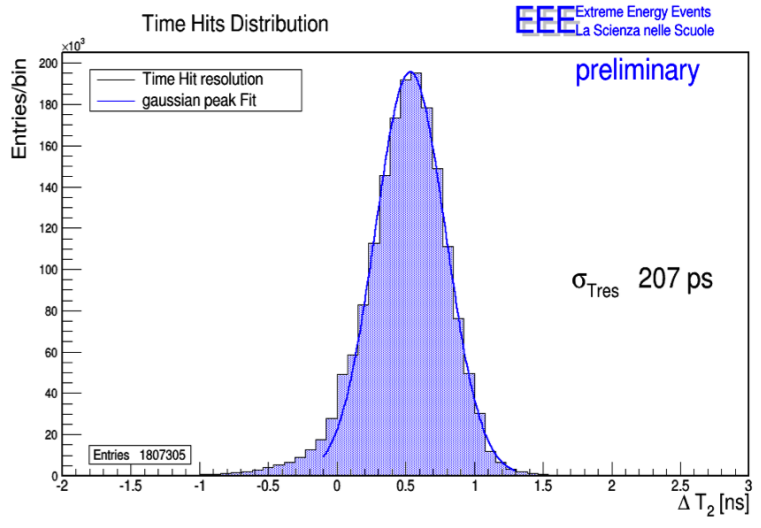


Figure 4.3:  $\Delta T$  distribution of one of the EEE telescope TORI-03, showing the gaussian fit and the time resolution  $\sigma_t = 210$  ps.

threshold<sup>1</sup>, the so-called *leading edge*. The time when the signal gets smaller than the threshold is instead called *trailing edge*. The Time Over Threshold (TOT) corresponds to the time difference between the leading and the trailing edge and is the time during which the signal released by the strips remains over the threshold of the signal discriminator. The TOT depends on the charge released in the ionization and on the signal amplitude and the effect of its jitter has to be corrected in order to get the real hit time (*time slewing* correction). The correction (performed on each chamber) makes use of the correlation between TOT and the difference between the measured times and the time expected on the concerned chamber. This correlation is fitted with a 4-th order polynomial. Figure 4.4 shows an example of one the telescopes of the EEE array. The fit parameters are then used to obtain the correction to the measured times according to their TOT. The correction to the measured time is applied as follows:

$$\bar{t} = t - t_s(TOT) \quad \text{where} \quad t_s(TOT) = c_0 + c_1 TOT + c_2 TOT^2 + c_3 TOT^3 \quad (4.3)$$

$t_s(TOT)$  is the time-slewing correction function, and  $c_n$  are the polynomial coefficients.

Once the correction is determined it is applied to each hit time and a new

<sup>1</sup>the threshold is set to the middle value for all the FEAs

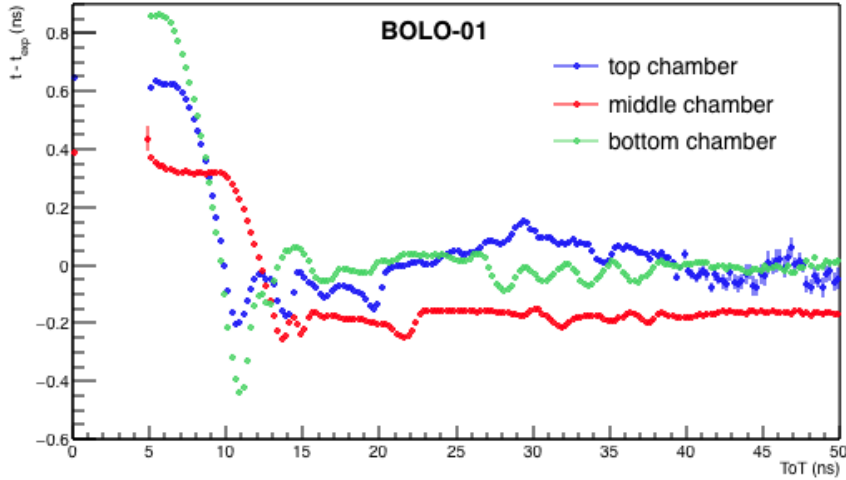


Figure 4.4: Correlation between TOT and the difference between the measured times and the time expected on the concerned chamber. The distributions are shown for the telescope BOLO-01 as an example; similar distributions are found for the other telescopes and used to perform the time slewing correction

time distribution is built by using the corrected time, in order to measure the time resolution. Some examples are shown in Figure 4.5. where the distributions before and after the time slewing correction are visible. The measurement has been performed on all the telescopes of the array and a  $\sim 20\%$  improvement after applying the correction is visible in all of them.

Depending on the telescope the time resolution ranges from 178 to 270 ps. In Fig. 4.6 a distribution obtained with the value of time resolution from 33 telescopes of the array is shown. The result from a gaussian fit gives a time resolution  $\sigma_t = 243$  ps, with a sigma of 44 ps. This resolution is within expectations and totally compatible with Run 2 results and with the resolution needed for the analysis performed by EEE. It can be compared with the value measured at the beam tests performed in 2006 at CERN [142]: 142 ps without time slewing correction and  $\sim 100$  ps with correction and  $t_0$  subtraction, to be noted that at the beam tests the beam was perpendicular to the detector, with a well selected spot thanks to a set of MWPC, with a defined energy and triggered by scintillators [142].

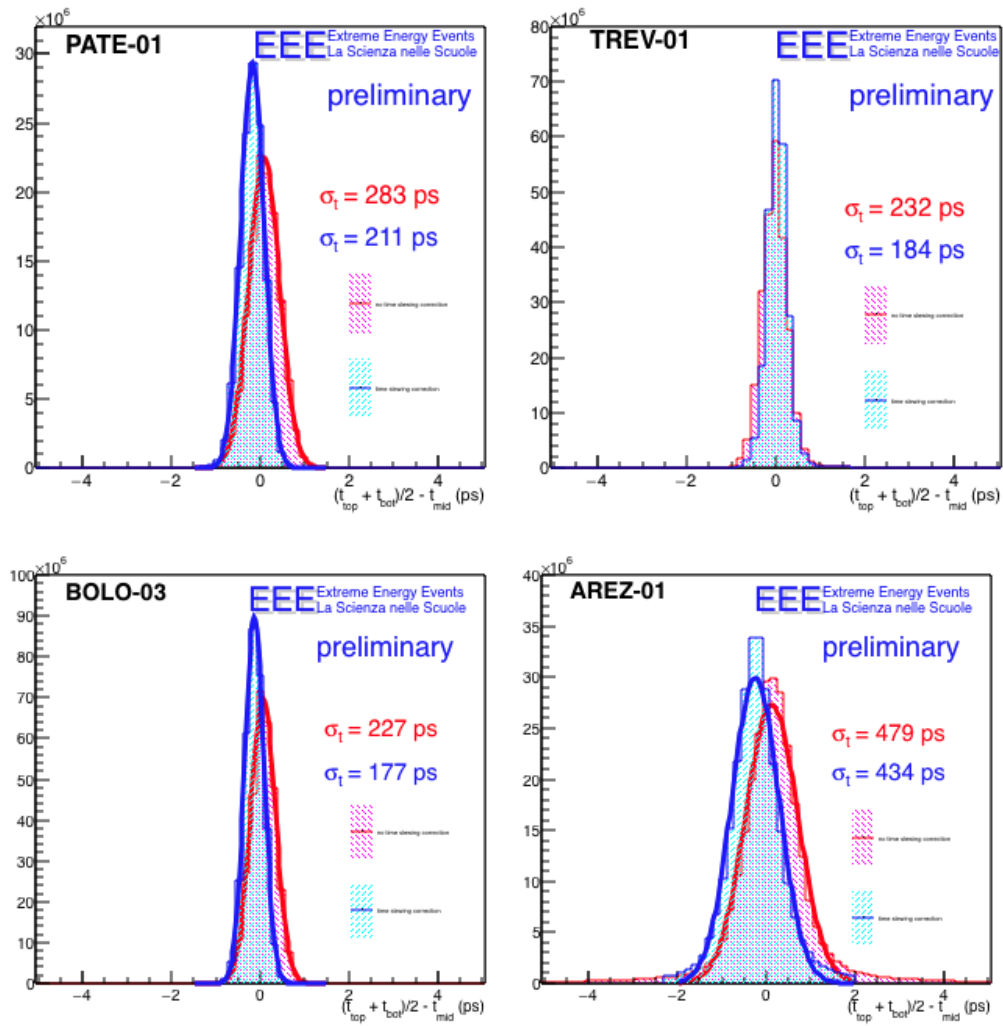


Figure 4.5: Time resolution of the telescopes: BOLO-01, BOLO-03, TREV-01 and AREZ-01, measured with data taken in Run 3; the distribution and the time resolution before and after time slewing correction are shown.

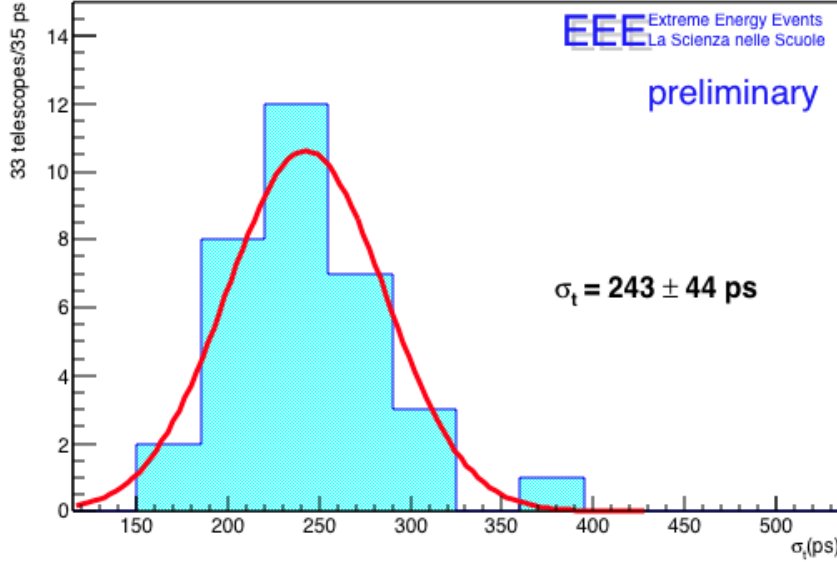


Figure 4.6: Time resolution of all EEE telescopes measured with data taken in Run 3, from 33 telescopes; the error is given by the gaussian fit of the time distribution and the result  $\sigma_t = 243$  ps is fully compatible with the expectations.

### Comparison study between Run 2 and Run 3

A data sample of events collected in a period of 30 days during the Run 2 and the Run 3 (section 3.5.7) has been analyzed from each EEE telescope with stable acquisition parameters, for a total amount of  $2.72 \cdot 10^9$  tracks from 41 stations in the Run2 and  $3.46 \cdot 10^9$  tracks from 46 stations in the Run 3.

### 4.5 Spatial resolution

As the time resolution, the space resolution is obtained by studying the distributions of the particle impact points in the tree MRPCs. The impact point in each chamber is reconstructed in the transversal direction  $y_i$  to the strips, by means of the strip involved by the cluster and, if the electron cluster has generated signals in two or more strips, by means of the average position of the hit strips. In the other direction,  $x_i$ , longitudinal to the strips, the impact point is evaluated from the signal arrival time at the two strip ends, the *right* ( $T_{right}$ ) and the *left* ( $T_{left}$ ) sides, measured by

two multi-hit TDCs. The space resolution has been performed similarly to the time resolution, by measuring the spatial information on the upper and lower chambers and by using these values to determine the expected position on the middle chamber, in the  $xz$  and  $yz$  planes both. This value is then compared with the hit measured on the middle chamber. Thus:

$$\Delta X_2 = \frac{x_{Bot} + x_{Top}}{2} - x_{Mid} \quad , \quad \Delta Y_2 = \frac{y_{Bot} + y_{Top}}{2} - y_{Mid} \quad (4.4)$$

Assuming the same space resolution in the tree chambers, as in the time resolution, the width of the obtained distribution will be proportional to the spatial resolution of the telescope and the space resolution along the longitudinal side and along the transversal side to the strip can be calculated as

$$\sigma_{x_{res}} = \sqrt{\frac{2}{3}} \sigma_{\Delta X_2} \quad , \quad \sigma_{y_{res}} = \sqrt{\frac{2}{3}} \sigma_{\Delta Y_2}. \quad (4.5)$$

### Longitudinal spatial resolution

The two signal arrival times are related to the  $x$  coordinate, to the chamber's length  $L$  and to the signal drift velocity in the strip  $v_{drift}$ :

$$T_{right} = \left(\frac{L}{2} - x_i\right) \frac{1}{v_{drift}} \quad \text{and} \quad T_{left} = \left(\frac{L}{2} + x_i\right) \frac{1}{v_{drift}} \quad (4.6)$$

Therefore the  $x_i$  position is evaluated as an average from both equations, by the difference of the two times:

$$x_i = \frac{T_{left} - T_{right}}{2} v_{drift} \quad (4.7)$$

where  $v_{drift} = 15.8$  cm/ns.

The  $x$  distribution on each strip appears not centered at zero, as the distribution  $\delta_T = T_{left} - T_{right}$ , because of some differences in the single signal paths in the FEA, in the TDC channels, or in the amphenol cables. As an example the time difference  $\delta_T$  in the tree chambers from a TORI-02 datafile is plotted in Fig.4.7. A single datafile contains  $5 \times 10^4$  trigger events. A first calibration, the *mean strip* correction, was applied in each sample analyzed at CNAF, by centering the time different distribution at zero. Another calibration has been performed later, the *strip by strip* calibration, by centering the  $x$  distribution in each strip at the "zero" of the chamber (79 cm). Some of the  $x$ -coordinate distributions from the strips in the Top, Middle and

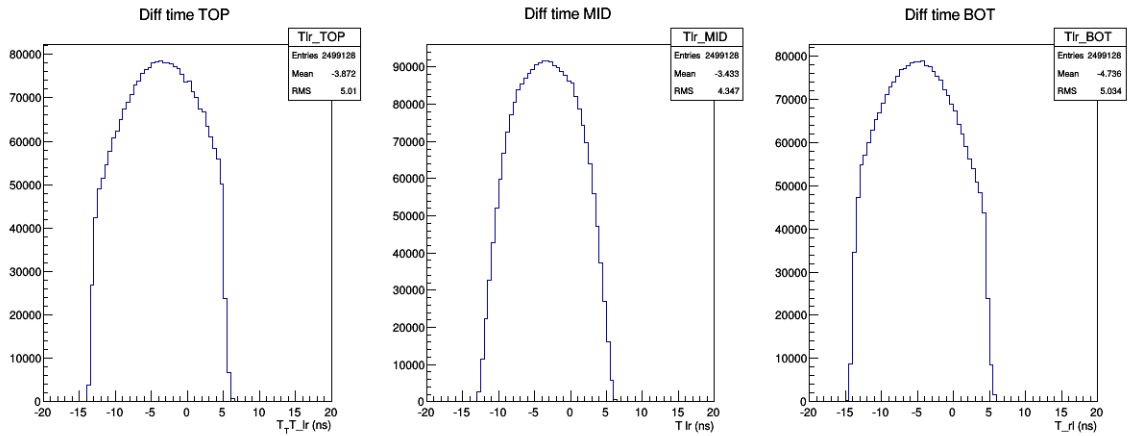


Figure 4.7: Distribution of the time differences  $\delta_T$  as the signal forms inside the Top, Middle and Bottom chamber in units of ns.

Bottom chamber contained in a single datafile are shown in Fig.4.8. In each datafile an histogram for each strip is built and its mean value  $M_{strip}$  is used

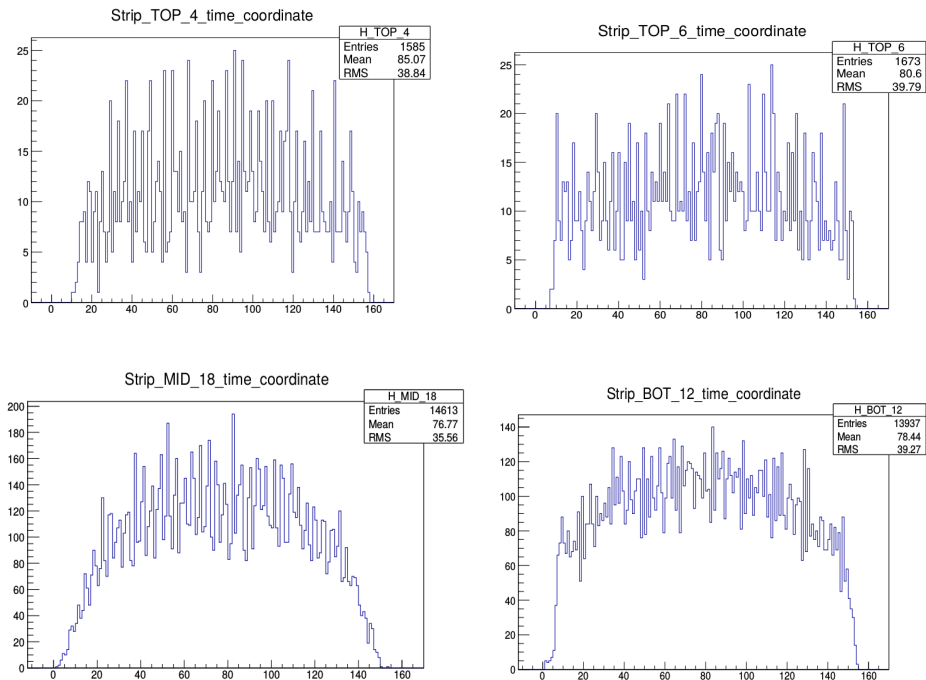


Figure 4.8:  $x$ -coordinate distributions from some strips in the Top, Middle and Bottom chamber from a SAVO-02 datafile

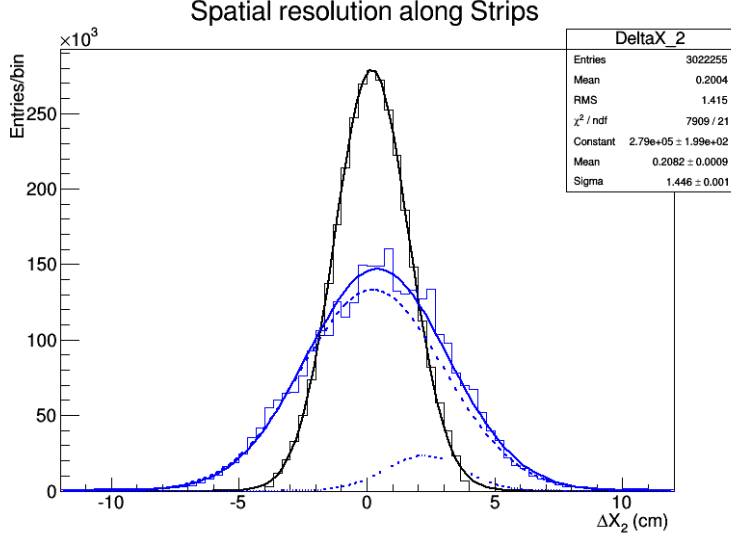


Figure 4.9: Comparison of spatial resolution without (blue) and with (black) the *strip by strip* centering procedure.

for compensating the  $x$ -position on the strip:

$$x_{corr} = x_i - (79 - M_{strip}). \quad (4.8)$$

In Fig.4.9 one can see a comparison between the spatial resolution with the only *mean strip* correction and the spatial resolution corrected by using the *strip by strip* centering procedure in the TORI-02 telescope, measured with data taken in Run2. It is possible to verify that two gaussian contribution are present in the first distribution(*blue*) built with the mean strip calibration. The distribution is fitted with two gaussians function and the convolution fit gives as a result  $\sigma_{\Delta x_2} = 2.4$  cm. The result obtained for the  $x$ -direction resolution is  $\sigma_x = 1.99$  cm whereas the strip by strip calibration has obtained a time resolution of 1.18 cm, with one gaussian fit, an improvement of 40%. The strip by strip calibrations are implemented directly at CNAF during the standard tracking procedure of the entire telescope array.

The  $\sigma_{x_{res}}$  distributions from the telescopes studied during the Run2 and during the Run3 are shown in figure 4.10, The result from a gaussian fit gives a longitudinal resolution of:

$$\sigma_{x \text{ Run2}} = 1.483 \pm 0.038 \text{ cm} \quad , \quad \sigma_{x \text{ Run3}} = 1.494 \pm 0.035 \text{ cm} .$$

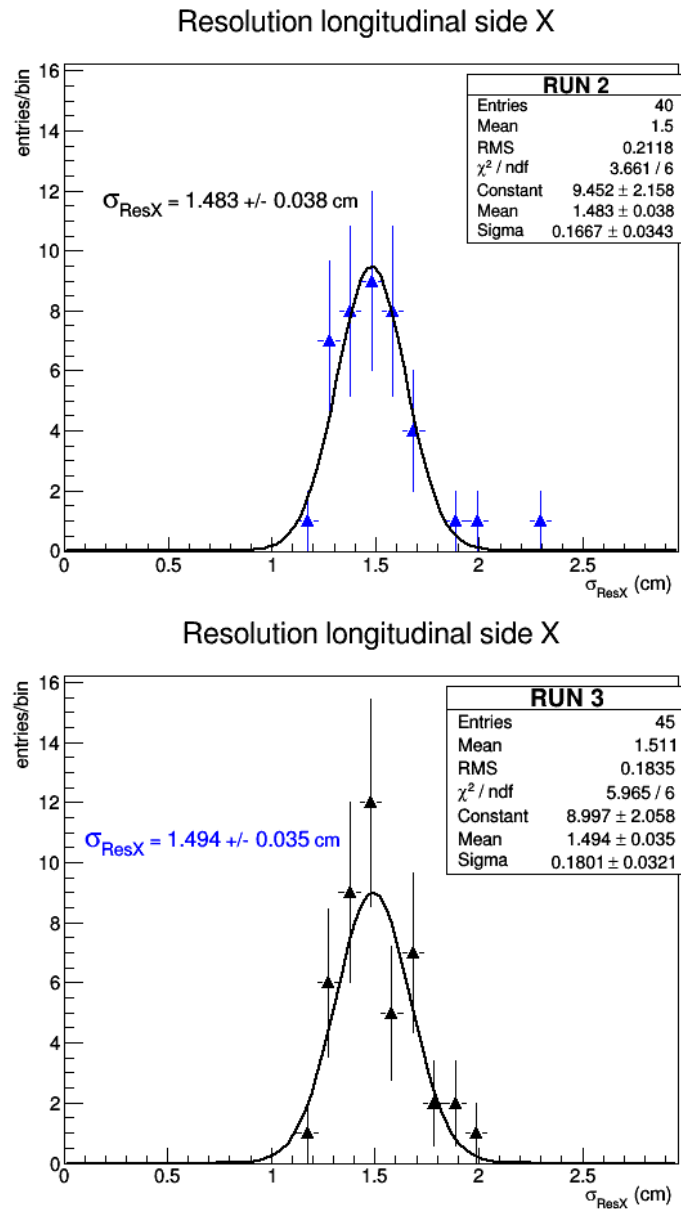


Figure 4.10: The  $x$ -coordinate space resolutions from all the telescopes studied during the Run2 (top) and Run3 (bottom)

The two results are fully compatible, they show the array stability during the two acquisition periods both. If the TDC resolution ( $\sim 100$  ps) and the drift velocity of the signal on the strip ( $v_{drift} = 15.8\text{cm/ns}$ ) are taken into account, the expected longitudinal resolution is:

$$\sigma_{xexp} \sim \sqrt{\sigma_{TDC}^2 + \sigma_{TDC}^2} v_{drift}/2 = 1.1\text{ cm}, \quad (4.9)$$

This value is compatible with the measured one in Run 2 and Run 3.

### Transverse spatial resolution

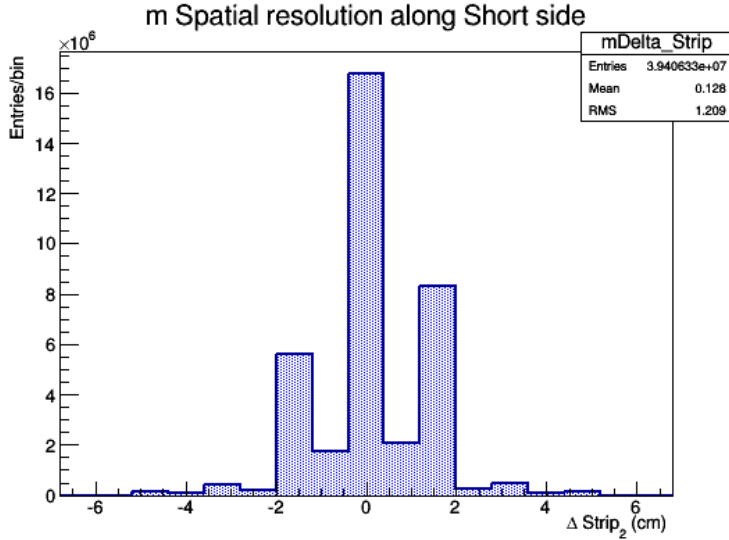


Figure 4.11: spatial resolution of the telescope CAGL-01 measured during Run 2.

The spatial resolution the transverse direction to the strips, the  $y$ -direction, is measured with the usual formula 4.4.

As an example the  $\Delta y_{hit}$  distribution of CAGL-01 during Run2 is plotted in Figure 4.11. The shape of the distribution is due to the position of clusters generated by two hits ( $\sim 10\%$  in each Chamber), evaluated as the mean between the two strip positions. After the unfolding with 3 chambers, the value found of the resolution is 0.99 cm. The resolutions  $\sigma_{y_{res}}$  from the stations selected during Run2 and Run3 are both presented in Figure 4.12, in good agreement with the expected resolution given from the pitch of the strips (3.2 cm):

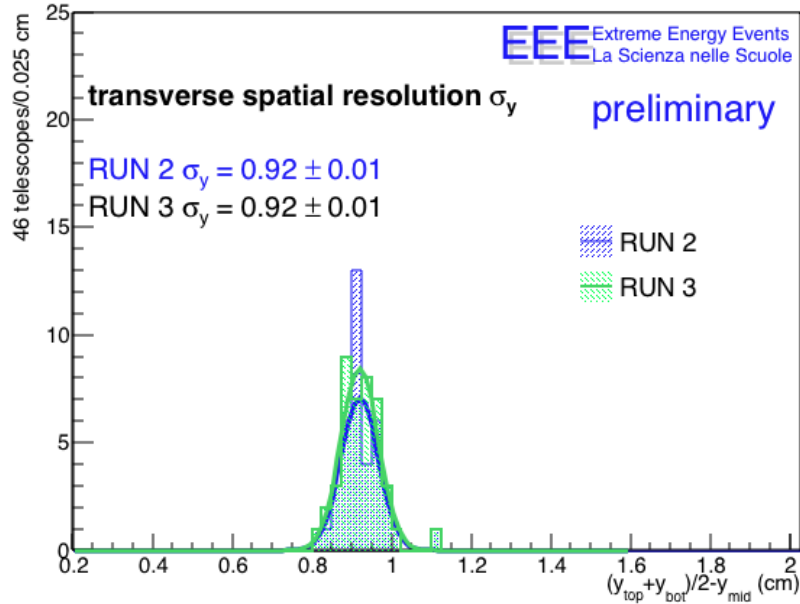


Figure 4.12: The  $y$ -direction space resolutions of all the telescopes analyzed the Run2 (a) and Run3 (b)

$$\sigma_{y(exp)} \sim \text{pitch}/\sqrt{12} \sim 0.92 \text{ cm}$$

## 4.6 Efficiency

The efficiency versus HV curves for each telescope are measured, inside school buildings, before and after a coordinated data taking, to test the stability of the chambers. In the standard procedure two scintillators are placed above and below the detectors, providing the trigger on cosmic muons passing through the 3 chambers. Thus several tests have been performed in several towns with equivalent results [113], [114], [115]. All the measurements showed at a plateau of 17/18 kV, an efficiency higher than 90%, also in the older EEE stations, built in 2007. This value is compatible with that measured on a single chamber in a test beam. Later on, during data acquisition runs, the MRPCs efficiency has been measured without using any additional detector. The procedure uses only the telescope MRPCs and the reconstruction code. This method guarantees the possibility to check periodically the detectors performance and provides efficiency corrections for all the analysis.

### High Voltage stability

The high voltage (HV) applied to an MRPC, or generally to a RPC-based detector is a sensitive parameter for all the applications of these detectors to absolute particle flux measurements as well as for relative measurements performed over a long time period. The HV directly defines the working point of the detector, to be ideally fixed within the *plateau* region, 300-400 V beyond the knee of the efficiency curve and at the same time at the lowest allowed value, in order to limit the *dark rate*. This last parameter is fundamental for such detector, being in a 10 - 1000 kHz typical range. Any HV fluctuation beyond 300-400 V can set the working point of the chamber in a region before the knee, where also tiny fluctuations (tenths of volts) correspond to a few percent efficiency variations. The stability of the HV power supply chain of the EEE telescope is therefore fundamental for allowing the EEE telescopes to be sensitive to phenomena involving a few percent particle flux variations, such as solar activity surveys, and also for the search of very rare events, where a few percent efficiency decrease on all the chambers of a cluster of EEE telescopes drives the cluster to a 20-50% efficiency suppression.

The EEE telescopes are powered by DC-DC converters, with output voltage roughly a factor 2000 with respect to the driving low voltage (LV) (see section 3.5.3 and appendix A). The HV stability declared by the manufacturer is  $\pm 1$  kV at full load (10 kV). The typical working voltage is 8-9 kV, thus very close to the full scale.

The temperature is an independent source of HV unstability for an RPC-based detector, being both the gain and the noise related to ionization phenomena and charge avalanche development in gas [128]. In figure 4.13 the HV time-trend is shown for a set of EEE telescopes. The blue, green and red lines represents the lower, middle and upper chambers, respectively. The differences among the HV applied to the chambers of the same telescope are related to the different plateau position for the various chambers.

Two different approaches can be applied, also in parallel, for correcting HV fluctuations due to temperature variations. The first, already in operation in several EEE sites, is the temperature control of the environment where the telescopes are installed. The second is the online correction of the HV by stabilizing the “effective” HV applied to the chambers, that differs from the actual HV applied, as stated in [143].

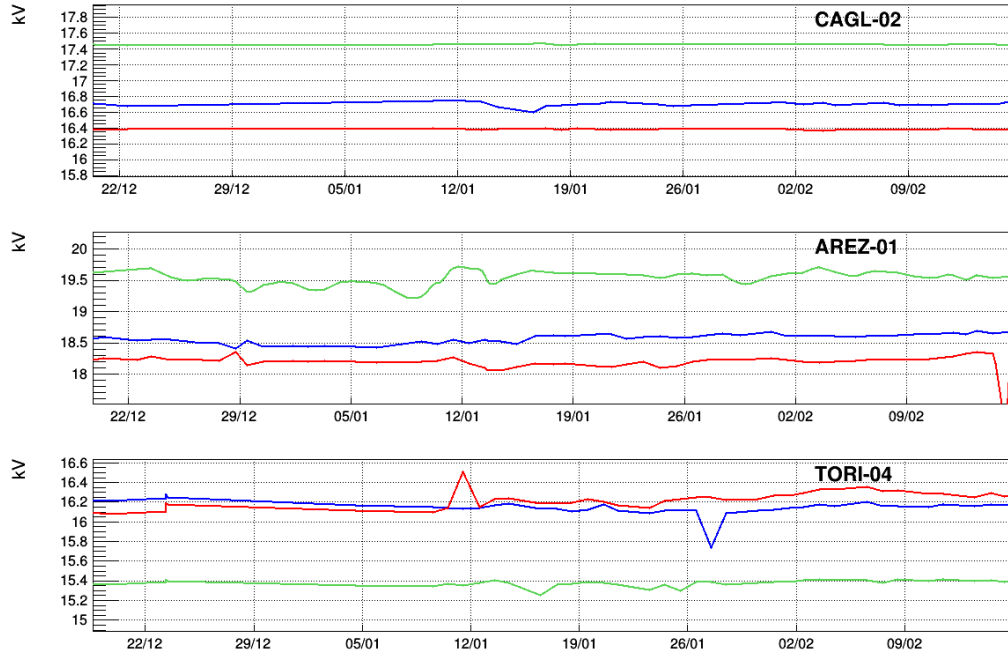


Figure 4.13: High voltage trend across the Run3 as observed at 3 telescopes of the network: CAGL-02, AREZ-01 and TORI-04. The blue, green and red lines represents the lower, middle and upper chambers, respectively.

### Outer chambers as trigger

During data acquisition runs, the MRPCs efficiency has been measured without using any additional detector. The procedure uses only the telescope MRPCs and the reconstruction code. This method guarantees the possibility to check periodically the detectors performances and provides efficiency corrections for all the analysis.

For the efficiency measurements the telescopes trigger pattern are modified from the 3-fold to 2-fold coincidence. Then the applied HV of the MRPC excluded from the trigger is varied. For each value of the applied voltage 150000 events are collected.

Using the reconstruction code one checks if the events acquired using the 2-fold coincidence have a valid hit also in the chamber under test. To reduce the noise due to the trigger condition events with 2-hit clusters in both the triggering chambers are used ( $\sim 5\%$  of the events).

and the middle chamber.

An example of the results of this measurements for the middle MPRC of various telescopes is shown in figure 4.14. During measurements atmospheric pressure  $p$  and temperature  $T$  were recorded so that the applied voltages are expressed as  $H.V_{eff}$  (correcting them for standard pressure,  $p = 1000 \text{ mb}$ , and standard temperature,  $T = 25^\circ \text{ C}$ ).

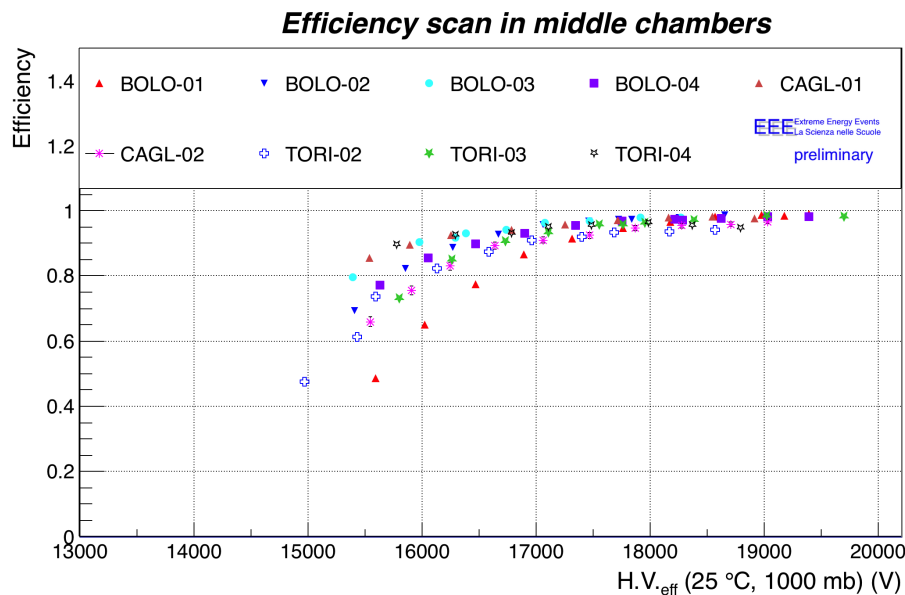


Figure 4.14: Efficiency vs. applied HV (corrected for standard  $p$  and  $T$ ) of the middle MRPCs of various EEE Project telescopes.

As shown in figure all the MRPCs show the typical efficiency curve as function of the applied voltage, reaching almost 100% for applied voltages greater than 17  $kV$ . This method can be used to measure the efficiency of all the MRPCs of the telescope by simply changing the trigger pattern. Once the MRPCs efficiency have been measured and the high voltages are set to the operating values.

Fig. 4.15 shows a distribution of efficiency values at the plateau from 33 telescopes (middle chamber). The result of the fit is a mean efficiency of 96%, compatible with the expectations and with the results from the beam tests performed in 2006 at CERN [142].

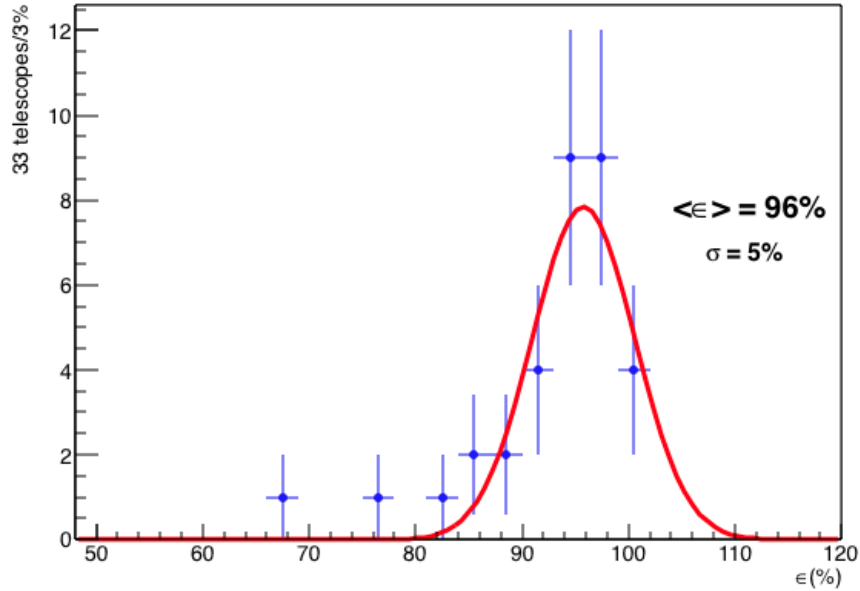


Figure 4.15: Distribution of the efficiency obtained at the plateau (corrected for standard p and T) of the middle MRPCs from 33 EEE telescopes. A gaussian fit gives as a result  $\epsilon = 96\%$ , with a sigma of  $5\%$

### External trigger

In some cases the efficiency measurement is also performed by using an external trigger. In this section a measurement performed on TORI-03 with  $2 \times 2 \times 25 \text{ cm}^3$  scintillators as trigger system is shown. The typical HV scan, together with an estimate of S/B, dark rate and muon rate corrected by  $\epsilon$  has been performed. The scintillators were used to measure the efficiency in two different areas of the 3 chambers, the center and the middle of the longitudinal side. The setup foreseen the connection of the signal coming from the scintillators in the DAQ system of the EEE telescope (by replacing the two outer chambers) and the measurement was done by reconstructing the tracks. In Fig. 4.16 the efficiencies of one of the three chambers is shown, together with the dark rate of the chamber, estimated by counting the OR of the 24 channels in single coincidence configuration (no coincidences with the scintillators). Also the muon rate (acquisition rate at plateau times the efficiency) and the ratio S/B are shown in the figure.

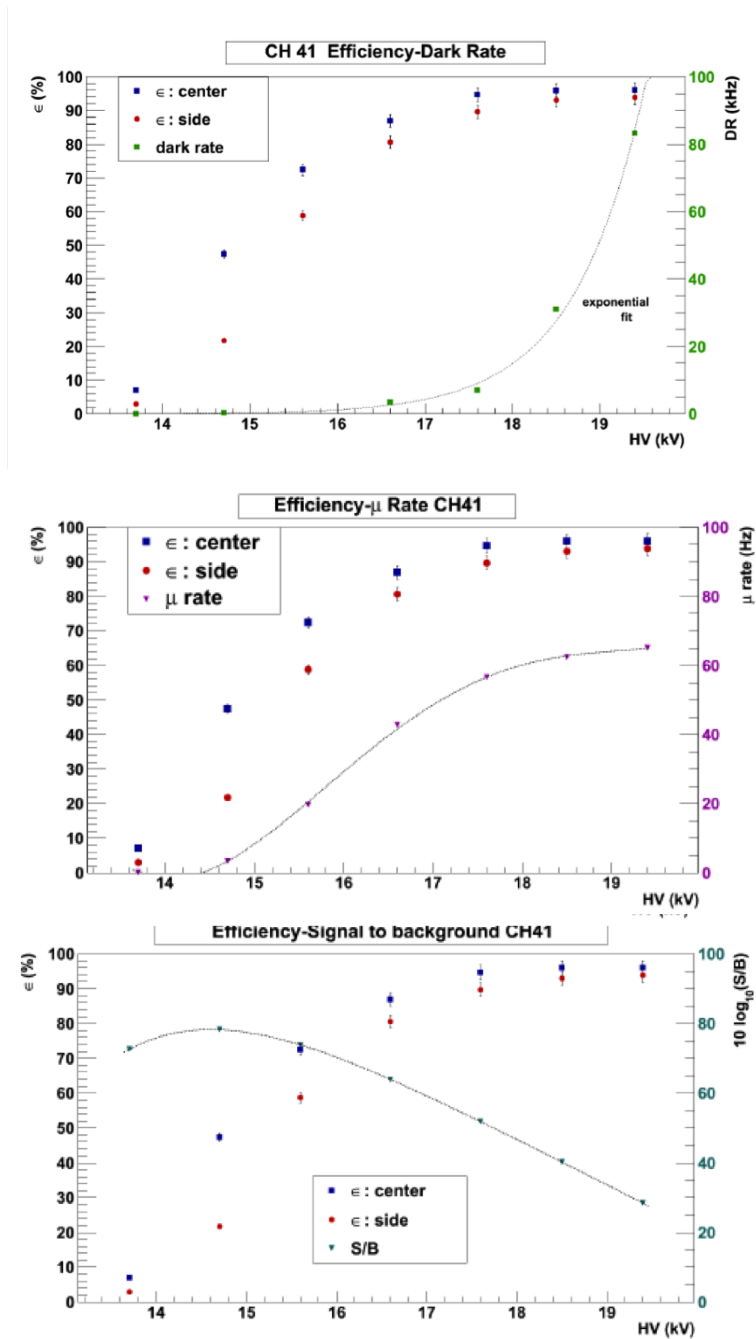


Figure 4.16: Efficiencies (center of the chamber and center of the longitudinal side) of one of the three chambers of TORI-03. The efficiency is shown together with the dark rate of the chamber in the first plot, with the muon rate in the second one and with the ratio S/B in the third one.

### 4.6.1 Long term stability

Long term performance stability is not easy to achieve with detectors hosted in schools, often far away from the nearest referee. To reach the goal an automatic Data Quality Monitor (DQM) has been created. Data collected by each telescope are transferred to the CNAF data center, section 3.5.6, where data analysis and DQM are performed. For each file transferred (covering  $\sim 1$  hour of data taking, depending on the telescope rate) a set of parameters and rates are extrapolated and published online [138]. Daily reports are also automatically generated, illustrating the evolution of the parameters over the last 48 hours. With this tool it is possible to properly react as soon as one station deviates from the standard behavior and make the necessary step to resolve the issue. Starting from the data file generated from the DQM and from the reconstruction output it is also possible to extend such trending plots to longer periods.

In Figure 4.17 and 4.18 the trends for a selection of relevant quantities are reported:

1.  $\chi^2$  : average of the tracks  $\chi^2$ .
2. *Time of Flight* : average of the tracks TOF between top and bottom chambers.
3. *DAQ rate* : raw acquisition rate.
4. *Reconstruction efficiency* : percentage of raw events where at least one track candidate has been found.
5. *Track rate* : rate of events with at least one track candidate.
6. *Multiplicity* : average number of hits on the three chambers in each event.

Data roughly cover 4.5 months of Run 2 data taking for the five telescopes with the best live time (time of active data taking).  $\chi^2$  and TOF together can be used to check the quality of the reconstructed tracks. Mean TOF values may be different for each station since distances between chambers are not the same for all installations.  $\chi^2$  is computed from the best (lower  $\chi^2$ ) tracks in each event, if at least one hit on each chamber has been

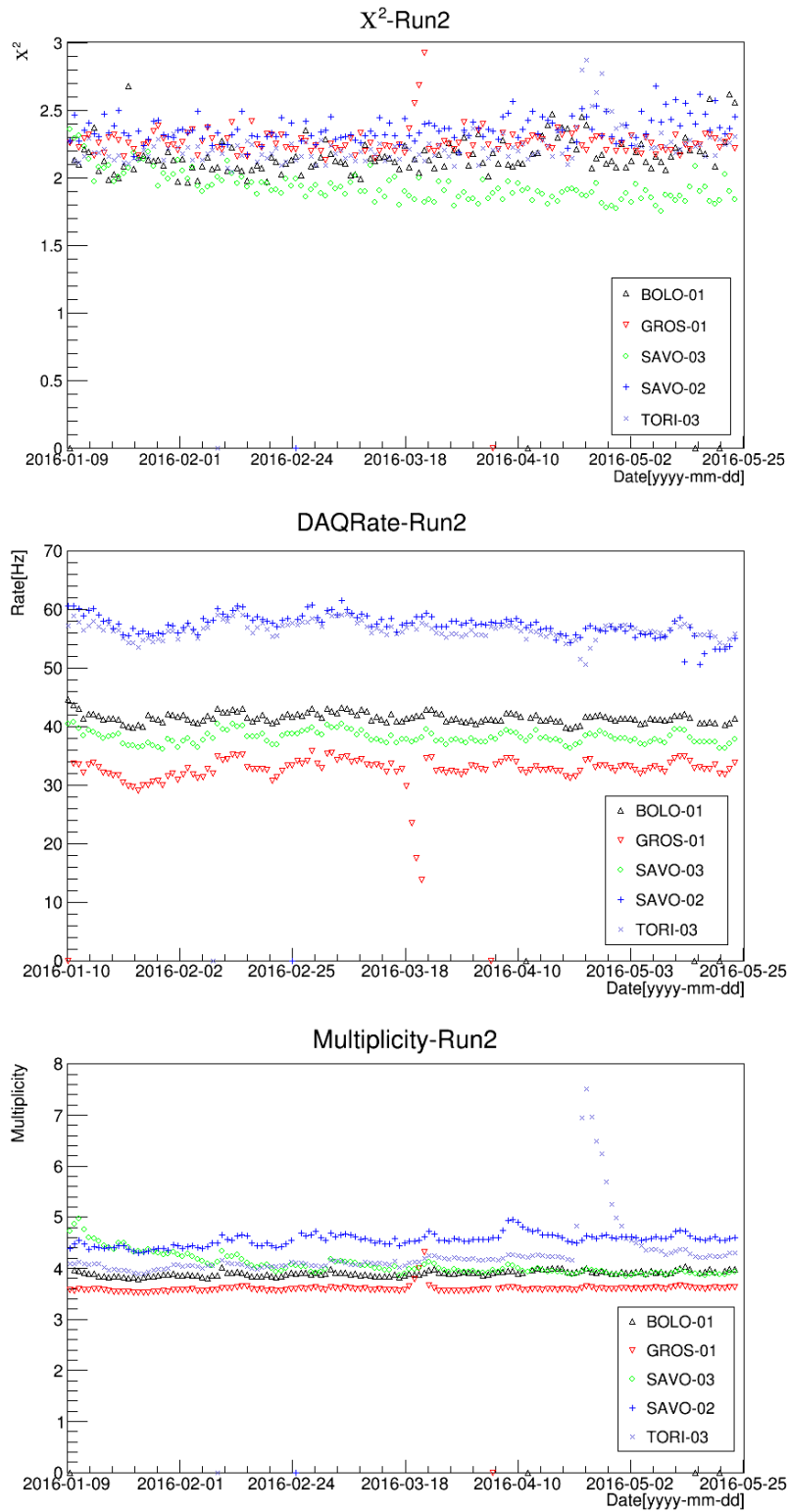


Figure 4.17: Run 2 trending plot for 5 stations, relative to  $\chi^2$  (1. *top*), raw rate in the chambers (2. *middle*), Track multiplicity (3. *bottom*). Point at zero represent days with the telescope not operational.

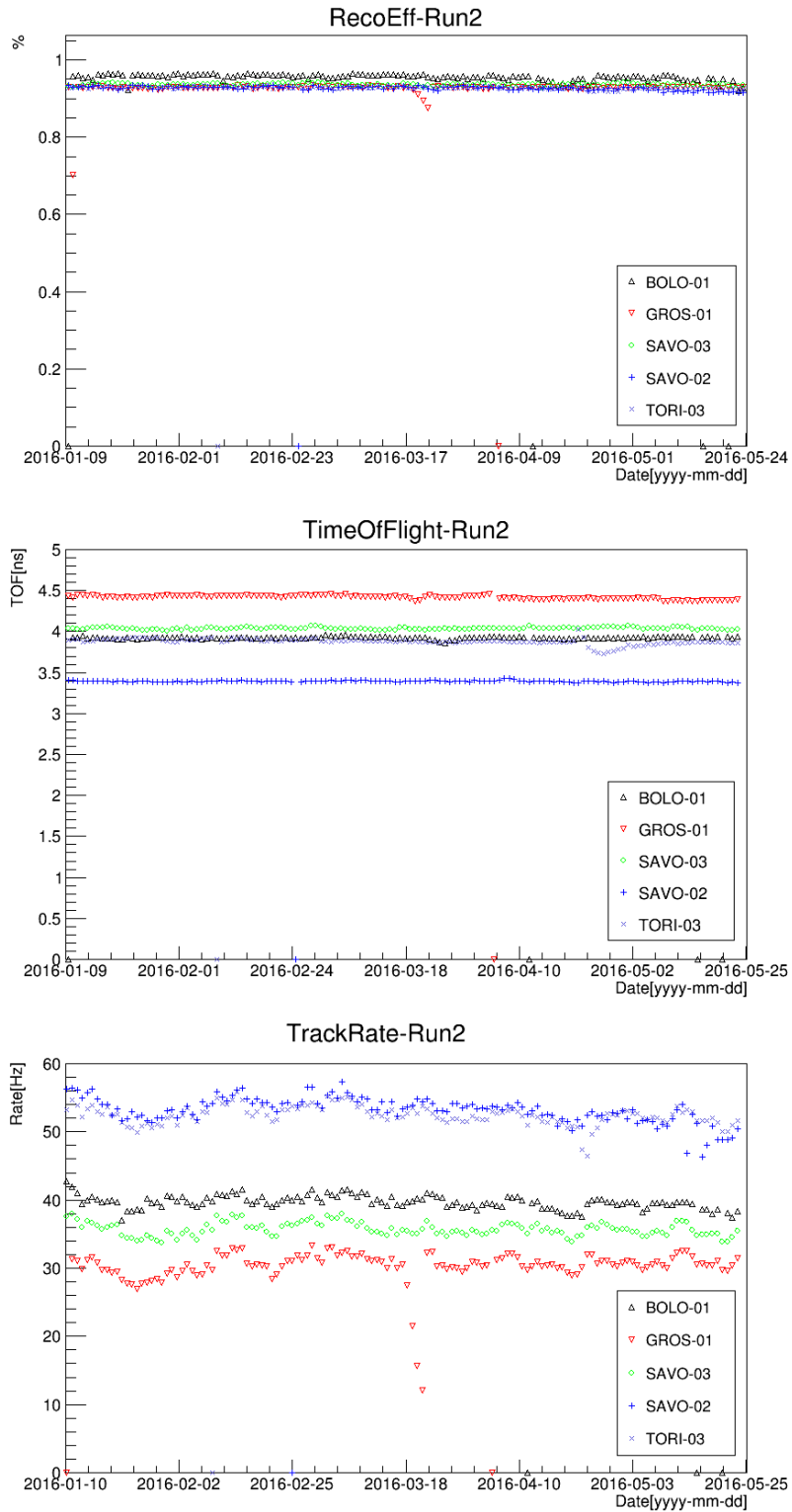


Figure 4.18: Run 2 trending plot for 5 stations, relative to DAQ rate (3. *top*), Time of Flight (4. *middle*), Track rate (5. *bottom*). Point at zero represent days with the telescope not operational.

recorded. Description of the event reconstruction can be found in section 4.1.

The rates are sensible to fluctuation of efficiency and noise rate of the detector, with the reconstruction efficiency used as cross-check. Multiplicity is a vital parameter, because is extremely sensible to gas and HV issues. Multiplicity can be also monitored for each chamber independently (see figure 4.19), where global and single chamber multiplicity are reported in the same period for some of the telescopes of figure 4.17. As an example it can

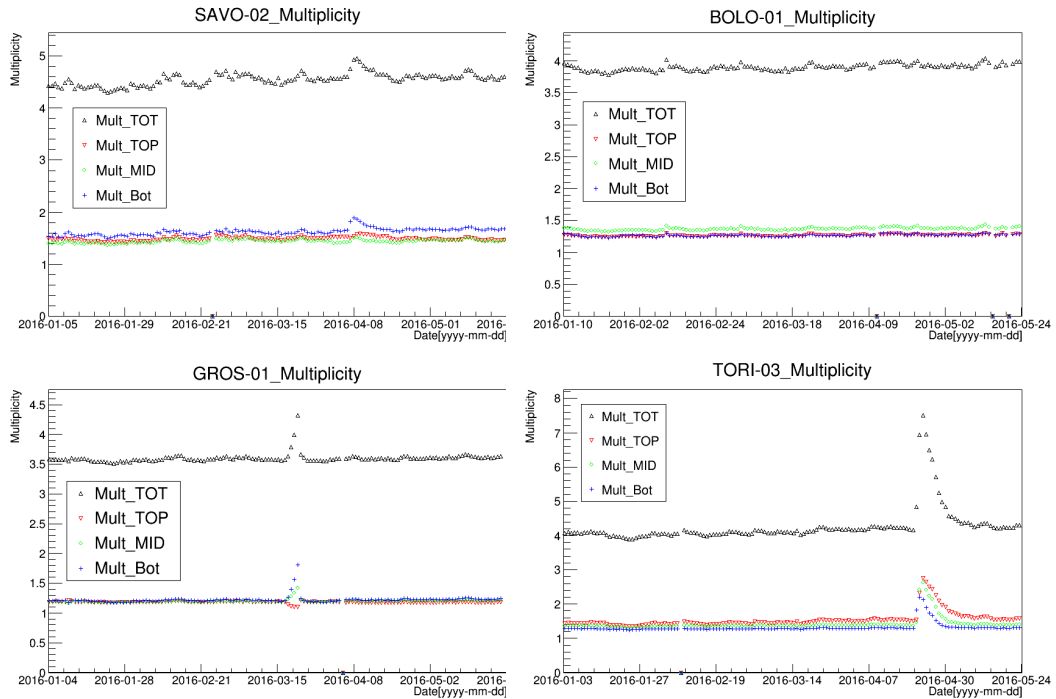


Figure 4.19: Trending plot of the track multiplicity of the 3 MRPCs for 4 stations during the Run2: SAVO-02, BOLO-01, GROS-01, TORI-03. Point at zero represent days with the telescope not operational.

locate an sudden rise of the multiplicity in the GROS-01 telescope. In this case only two chambers register an increase of the mean multiplicity, while the third one is decreasing. This behavior is characteristic of an interruption of the Freon circulation. One chambers start slowly to be filled with the quencher (only 2% of the flux) resulting in an efficiency drop, while the others have infiltration of air with correlated rise of the noise. Restoring the flux bring back the station parameters to normal value. The effect of this reduction is clearly visible also in figure 4.17 and 4.18.

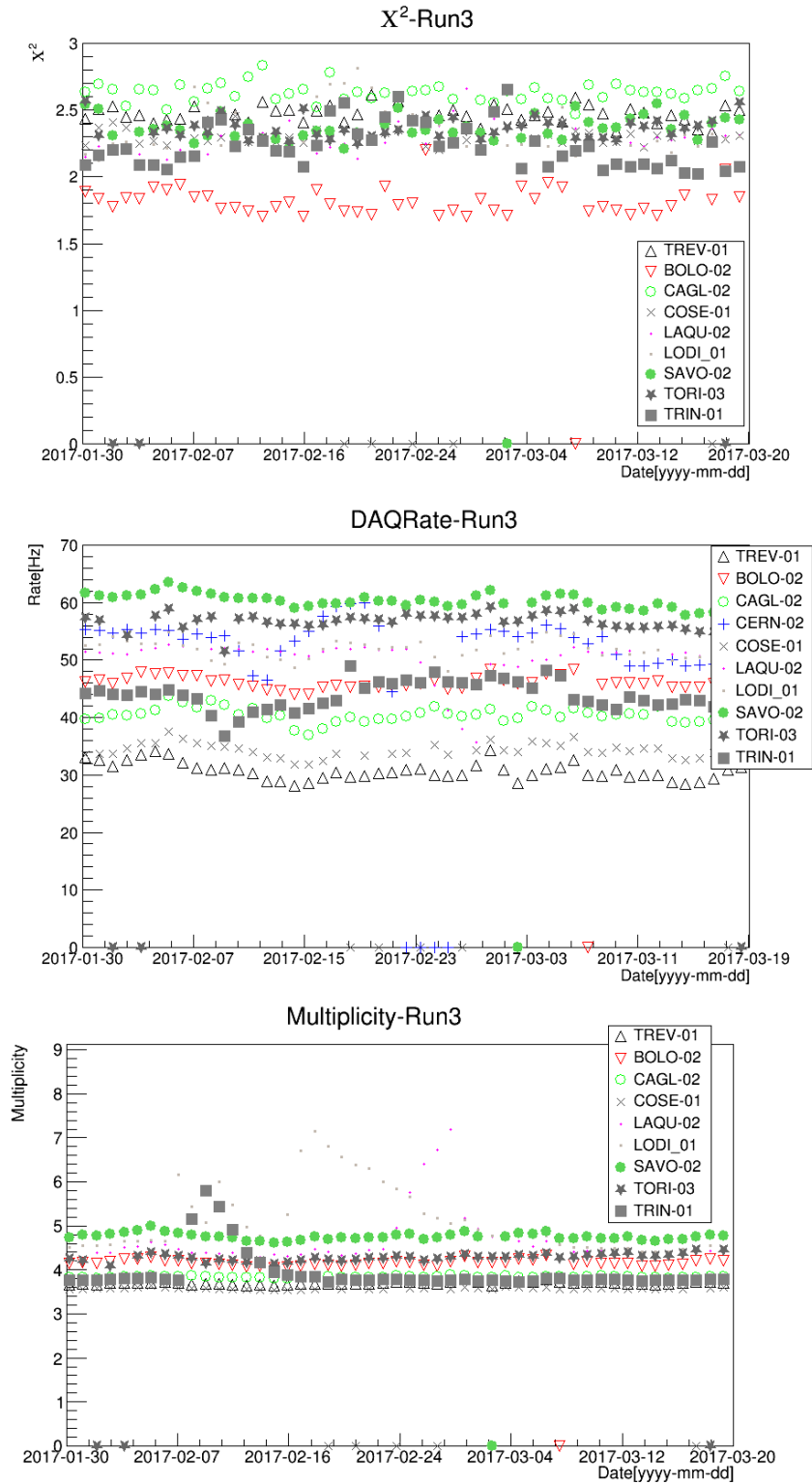


Figure 4.20: Run 3 trending plot for 9 stations, relative to  $\chi^2$  (1. *top*), raw rate in the chambers (2. *middle*), Track multiplicity (3. *bottom*). Point at zero represent days with the telescope not operational.

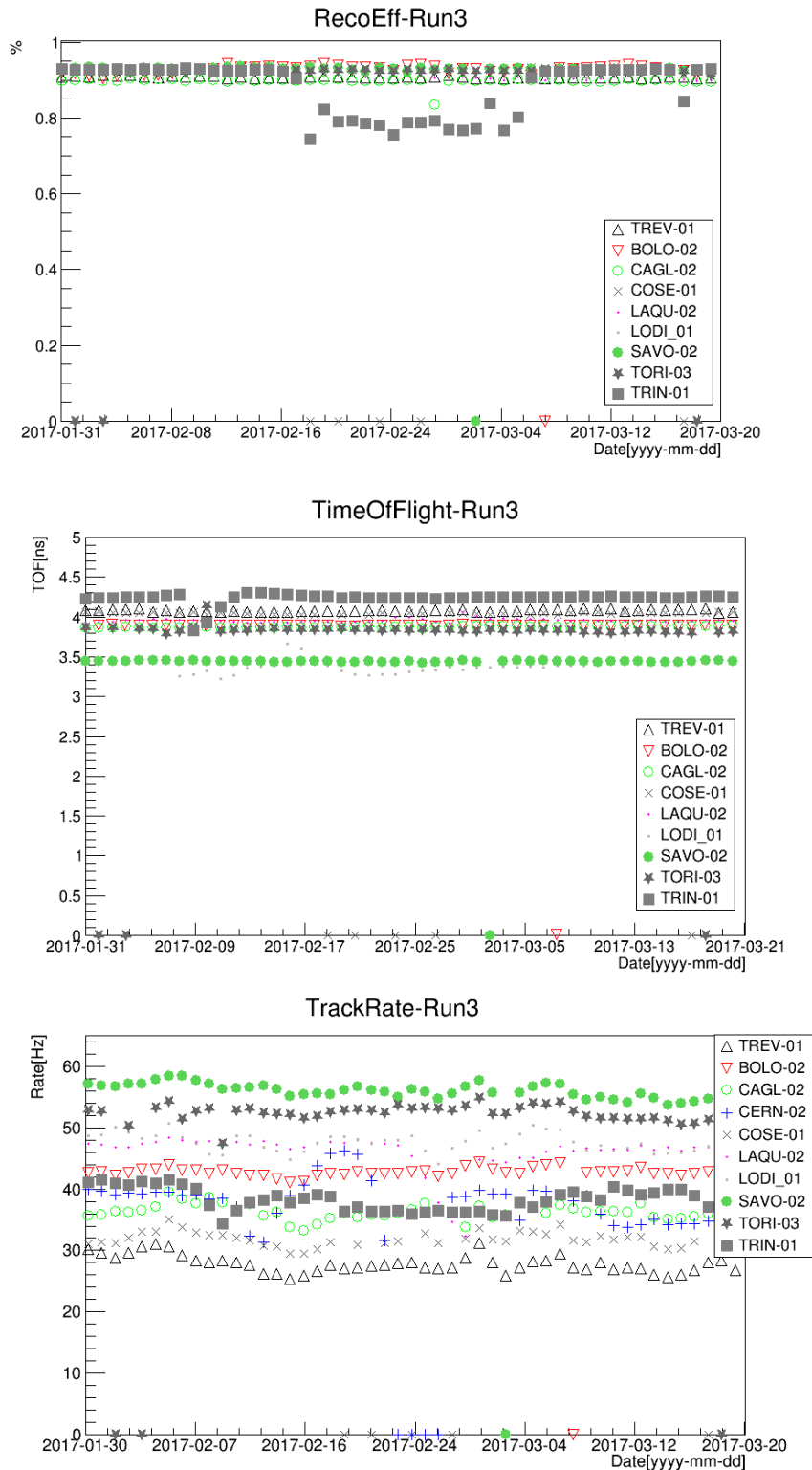


Figure 4.21: Run 3 trending plot for 9 stations, relative to DAQ rate (3. *top*), Time of Flight (4. *middle*), Track rate (5. *bottom*). Point at zero represent days with the telescope not operational.

Also for the Run 3 a report of the long term stability of a subset of stations has been done and reported figure 4.20 and 4.21 for a period of  $\sim 2$  months and a subset of 9 stations.

## 4.7 Comparison with beam-test results

As it was expected performance measured for the single MRPC are higher than Run2 detector performance. The measurements at test beam were acquired in the best conditions: the beam was centered in the middle of the strips, two pairs of scintillators were used to provide the trigger, the TDCs resolution time was 25ps bins. They point at the excellent achievement the EEE detectors are able to reach. Whereas into the field, in the EEE stations, with secondary cosmic rays (most of them are muons, but also electrons, pions etc), many factors can affect these results, as electronic noise, strip miscalibration or multiple scattering. However the results of the analysis on the performance of the array are fully compatible with the expectations in terms of efficiency ( $\sim 93\%$ ), time resolution (243 ps) and spatial resolution (1.5 cm and 0.9 cm respectively for longitudinal and transverse direction). At the moment the EEE Collaboration is focusing on a further improvement of the performance in terms of duty cycle and optimization of the working points of the telescopes.



## Chapter 5

# Study of anisotropy effects

At cosmic ray energies lower of  $\sim 1$  TeV the movements of solar plasma through the heliosphere influenced the Earth's magnetic field, causing a modulation of the cosmic ray anisotropy 1.7, 1.8. Furthermore the Compton-Getting effect predicts a dipole effect due to the moving of the Earth with respect to an isotropic cosmic ray rest system ???. If the Earth is moving in the rest system, the cosmic ray flux from the forward direction becomes larger.

The atmospheric down-going muons produced in air showers induced by interactions of primary cosmic rays in the Earth's atmosphere. Muons with energies above around 500 MeV at the sea level can reach the detectors, inducing primary ionization in the MRPC to reconstruct the direction of the muon. The muons represent a high statistic dataset that can provide information about primary cosmic rays at energies above few TeV. A sidereal variation of the cosmic rays intensity can induced the anisotropy in their arrival direction. However, it can also be caused by the detector exposure asymmetries, non-uniform time coverage, diurnal and seasonal variation of the atmospheric temperature, pressure, local characteristic of the geomagnetic field.

The muon flux  $\Phi(\theta)$  measured on the Earth's surface has a weak dependence on the azimuthal angle but depends strongly on Zenith angle, the angle made by the incident ray with the vertical direction at that point.

$$\Phi(\theta) = I_0 \cos^{n-1}\theta. \quad (5.1)$$

Using the *flat Earth* assumption  $n = 3$ , this expression gives the  $\cos^2 \theta$  distribution, 1.9.4. The expression gives a partially *good* description of the data, but only at lower Zenith angle (it is less useful at higher angles, this means assuming the Earth is flat).

The main challenge for this analysis is accounting for the detector asymmetry, and unequal time coverage in the data due to the detector run selection. The combination of a detector asymmetry with a non-uniform time coverage would induce an azimuthal asymmetry and consequently artificial anisotropy of the arrival direction of cosmic rays. The geometrical asymmetry results in a preferred reconstructed muon direction since the muons would pass by more strips, as an example due to strip with lower efficiency, in one detector direction compared to another. Moreover the combined effect of atmosphere, sea and detector modifies the measured zenith muons distribution, expected to be uniform at the entrance into the atmosphere for the incoming cosmic rays 1.10. Further corrections are needed in order to take into account that the atmospheric temperature fluctuations can affect the observed muon fluxes. Indeed, the density in the upper atmosphere is related to the temperature and so the relative probability for a meson to decay or to interact is also a function of the temperature. This meteorological variations of the cosmic ray muon flux could mimic a flux anisotropy. Once the correction has been applied, it will be possible to observe the obtained rate of events in equatorial coordinates and to study of the rate modulation along the Right Ascension.

### 5.0.1 Transformation of EEE data to equatorial coordinates

The basic way to extract the orientation of a muon track by measurements with one of the EEE telescopes is to employ the local altazimuth coordinate system. The orientation of a muon track, as derived from a fit performed on the hits detected on the three MRPC chambers, is defined by the values of the azimuthal angle  $\phi$  (which is usually referred to the magnetic North direction) and by the polar angle  $\theta$ , measured starting from the vertical direction ( $\theta = 0$ ), or by the altitude  $a = (90 - \theta)$ . Such coordinate system is very easy to implement and use, and at a first approximation allows also to correlate information from two close telescopes. Imposing that the time correlated tracks impinging on two telescopes have similar directions if they come from a single extensive air shower may be simply done evaluating the

### 5.0.1 Transformation of EEE data to equatorial coordinates 127

relative angle  $\theta_{1,2}$  between the directions  $(\theta_1, \phi_1)$ ,  $(\theta_2, \phi_2)$  of the two tracks, and choosing an upper cut (for instance  $\theta_{1,2} < 10^\circ$ ). Although this is not strictly correct, due to the Earth curvature, for telescopes which are not so far away, it represents a very good approximation. For instance, muon tracks detected both as vertical in two telescopes located in the same metropolitan area (3 km distance) have a relative angle smaller than  $0.03^\circ$ . In case of telescopes located in close towns (30-50 km) this effect amounts to about  $0.4^\circ$ , reaching about  $10^\circ$  for telescopes located very far away (1000 km apart). More important however is the fact that the use of an altazimuth reference system implies that the coordinates of a sky object change with time. For instance, two muon tracks - seen as vertical by the same telescope but at different times - clearly originate from a different region of the sky.

To define the position of any astronomical object, one needs to have a reference frame or coordinate system, in order to unambiguously identify the position of the object by two numerical quantities. While the altazimuth system (also called horizon system) makes use of the plane of the observer's horizon to define the azimuth and altitude of the celestial object, other coordinate systems are largely employed in astronomy. The equatorial coordinate system makes use of the plane of Earth's equator, extending such plane to cut the celestial sphere. The two coordinates needed in such a system are called the Right Ascension *RA* and the Declination *Dec*. The Declination is measured in degrees, positive north of the equator, negative south of it. The Right Ascension may be measured in hours, 0 to 24, or in degrees,  $\theta$  0 to 360, or  $-180^\circ$  to  $+180^\circ$ , and the origin is usually related to a fixed direction in the sky, namely the first point of Aries or *vernal equinox*, along the line of the intersection of the plane of the Earth's equator with that of the Earth's orbit around the Sun (Fig.5.1). This is the common system employed by astronomers to define the position of star objects in the near Universe, for instance location of individual stars, since such coordinates do not depend on time and have a unique meaning for all observers located in different regions of the Earth. This is then the most convenient one to study the properties of the astronomical environment around the Solar System. Other coordinate systems exist, which are most convenient to investigate more easily specific aspects of the sky: the ecliptic system, making use of the plane of the Earth's orbit around the Sun, makes it more convenient the study of objects belonging to the Solar system while the galactic system, where the reference plane is the plane of our Galaxy and the important

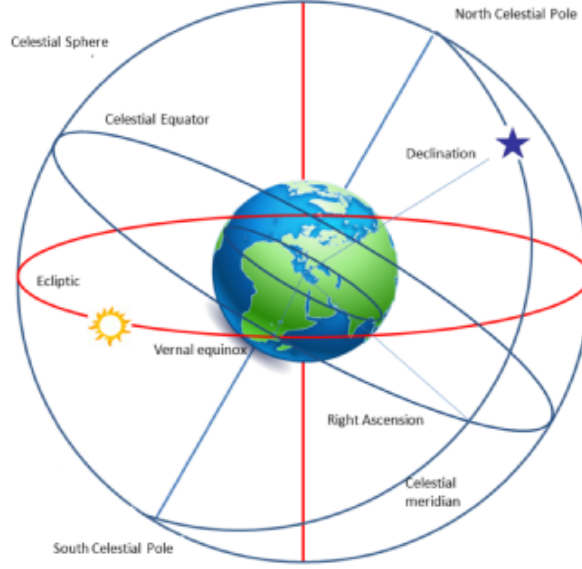


Figure 5.1: Schematic view of the equatorial system coordinate.

direction is that connecting our Sun to the center of the Galaxy, allows an easy location of stars with respect to the Milky Way.

To transform from one reference system to the other by the use of appropriate variable transformation requires to know the location of the site on Earth, and the observation time for each event. In our case it needs to transform from the altazimuth to the equatorial reference system. Given the orientation of a muon track (altitude  $a$  and azimuth  $\phi$ ), its declination  $\delta$  and hour angle  $H$  are given by [98]:

$$\sin\delta = \sin a \sin\phi + \cos a \cos\phi_L \cos\phi \quad , \quad \cos H = \frac{\sin a - \sin\phi_L \sin\delta}{\cos\phi_L \cos\delta} \quad (5.2)$$

where  $\phi_L$  is the observer's geographical latitude. The hour angle  $H$  and the Right Ascension  $RA$  are related by the formula

$$H = LST - RA \quad (5.3)$$

where  $LST$  is the local sidereal time, which depends in turn on the GPS time associated to the detected event. Useful macros were implemented to manage all these transformations on an event-by-event basis, so as to map each detected event into the  $(RA, Dec)$  plane.

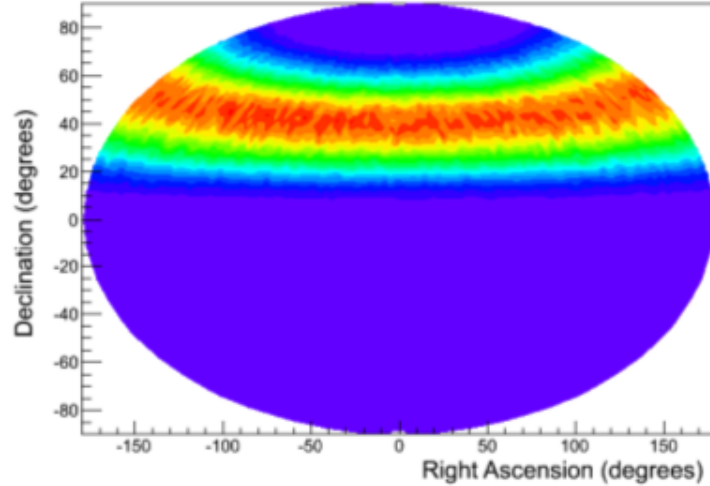


Figure 5.2: Aitoff map of the sky coverage of a typical EEE telescope, located around  $37^\circ$  Lat. North.

The fraction of sky covered by a particular cosmic ray detector depends on its geographical location and on the geometrical acceptance of the detector. Since all the telescopes of the EEE networks are presently located in Italy or very close to it (CERN), hence along geographical latitudes between  $37^\circ$  and  $46^\circ$ , they mostly cover that part of the sky between the equator and about  $70^\circ$  in Declination. The amount of coverage in Declination also depends on the largest polar angle with respect to the vertical the telescope is able to see, which for most of the telescopes is around  $40^\circ$ . As an example, Fig.5.2 shows the Aitoff projection map describing the sky coverage of a telescope situated at about  $37^\circ$  Lat. North, in one complete day (24 hours) of data taking.

## 5.0.2 Muon orientation with respect to primary axis

It is well known that most of the secondary particles produced in the development of an extensive air shower in the Earth atmosphere are concentrated along the direction of the primary particle producing the shower. This near parallelism around the primary axis is the basis for a rough reconstruction of the distribution of the incoming direction of the primary by a single muon detector. The average relative angle of the secondary particles with respect to primary depends however on several factors, namely the species of secondary products being considered, its energy as well as the energy of the primary.

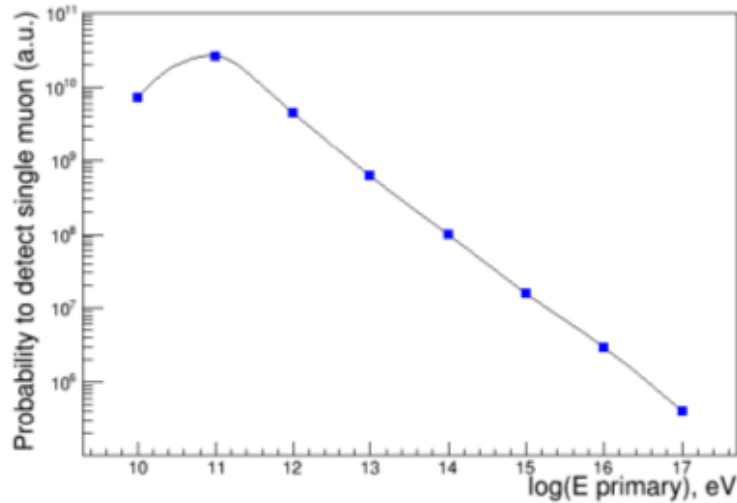


Figure 5.3: Probability to detect individual muons as a function of the energy of the primary proton.

To quantify such aspects in our case, it carried out quantitative CORSIKA calculations of extensive air showers initiated by primary protons of various energies, arriving with an isotropic random distribution of their original orientations, between the vertical and  $60^\circ$ . Particles were followed down to the sea level, with only a very small cut on their energy. Proton energies between  $10^9$  and  $10^{17}$  eV were considered. The number of simulated showers was of the order of 40000 for low energy primaries, and correspondingly lower for the more energetic showers, in the order 0.85 of a few hundred. Taking into account the number of muons in the shower, which roughly scales as  $E^{0.85}_{primary}$ , and the primary flux as in eq.  $\frac{dN(E)}{dE} = k E^{-\gamma}$ , with  $\gamma = 2.7$  1.2, the probability to detect individual muons with respect to the energy of the primary nucleus may be evaluated. As it is seen from Figure 3, most of the muons detected at the sea level come from extensive air showers in the range  $10^{10}$  -  $10^{12}$  eV. Secondary muons were selected in the list of produced particles, and for each particle the relative angle with respect to the primary axis was considered, Fig.5.3. The blue symbols report the values obtained taking into consideration all secondary muons. It is expected that muons of higher energy are more concentrated around the primary axis. A cut on the muon energy at 1 and 10 GeV has been applied to filter the data, and the results are shown in green symbols (for those muons of energy higher than 1 GeV) and in red symbols (for the muons with energy higher than 10 GeV).

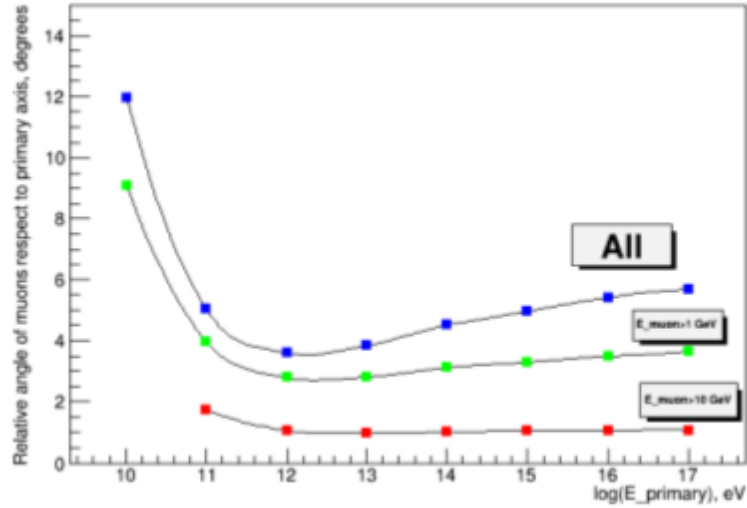


Figure 5.4: Average relative angle of secondary muons with respect to primary axis. The blue squares show all muons, while green and red squares report the values obtained for those muons with energy larger than 1 or 10 GeV respectively.

As it is seen from the plot, at low primary energy, of the order of  $10^{11}$  eV, the average value of the relative angle is about  $5^\circ$ , decreasing to about  $4^\circ$  for more energetic showers. Due to some shielding around most of the EEE telescopes, some degree of muon absorption is always present. Several layers of concrete are able to absorb muons of several hundred MeV. A cut at 1 GeV results in slightly smaller values of the average relative angle (about  $3^\circ$ ). Due to the abundance of primary cosmics (as plotted in Fig.3), it may be inferred that for low energy primaries and low values of the secondary muon energy, within a relative angle of the order of a few degrees the direction of the incoming muon mirrors that of the original proton direction.

### 5.0.3 Multiple scattering due to the presence of the building

Another factor which in principle may affect the reconstruction of the orientation of a charged particle moving through a dense material is the amount of multiple scattering suffered during its path. Although believed to be of minor importance with respect to the previous one, quantitative estimation of this effect was done by means of a GEANT simulation incorporating the possible presence of concrete layers above the EEE telescope in a typical installation. Over the various EEE sites, telescopes are located in very different environments, ranging from a very light roof to several concrete

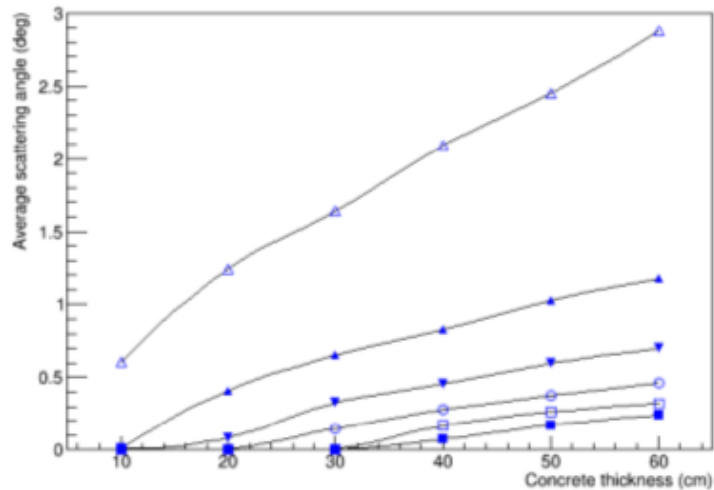


Figure 5.5: Scattering angle of secondary muons with respect to their original direction, as a function of the thickness of traverse concrete. From top to bottom, data refer to muons of increasing momentum (0.5, 1.0, 1.5, 2.0, 2.5 and 3.0 GeV/c).

layers, as it is the case for instance of those installations where the telescope is located at the ground floor (or even in the underground floor) of a tall building with several floors and solid walls around it. Layers in the building were modeled for simplicity as solid blocks of concrete (whose actual composition was introduced in the simulation) with uniform composition, even though the mechanical structure of one of such layers in reality has a complex shape with empty parts, iron and concrete parts. Taking into account a realistic geometry and material composition of the layer separating one floor from the other in a modern building, it may be estimated that the overall effect of such layers on the average energy loss and multiple scattering of muons roughly corresponds to those introduced by 10-15 cm of solid concrete. The average scattering angle was evaluated as a function of the concrete thickness, and for several values of the muon momentum, from 0.5 GeV/c to 3 GeV/c, since it is well known that this effect is larger for small momentum particles. Fig.5.5 shows the results. As the plot shows, the effect of multiple scattering for most of the muons in the range 1-3 GeV/c stays well below  $1^\circ$ ) even for heavy shielding around the detector, so it is not the dominant term in the uncertainty of the original primary direction.

## 5.1 Analysis

### 5.1.1 Acceptance and time exposure corrections

Due to the rectangular shape of the EEE chambers and their relative distance, the geometrical acceptance of a particular telescope is not uniform and must be corrected even to reconstruct the muon angular distributions in local coordinates  $(\theta, \phi)$ . Moreover, the data taking may be affected by interruptions over long periods, resulting in partial coverage of the sky map in equatorial coordinates during each specific 24 hour period. For these reasons, it is quite mandatory to evaluate the specific acceptance in (*Right Ascension, Declination*) of each particular telescope, taking into account not only its geometry but also the effective periods of data taking (time exposure). The so called scrambling or shuffling method is a widely used procedure to obtain corrected data from raw data. Basically, it considers two (RA, Dec) maps. The Data map is obtained from real events considering the values  $(\theta, \phi, t)$  of the local coordinate angles  $\theta, \phi$  together with associated time  $t$  of the event, and transforming these values into (*Right Ascension, Declination*) variables.

A Reference map is also obtained by considering the same  $(\theta, \phi)$  muon orientation, associated to the time  $t_R$  of a random event chosen within a period where the running conditions are believed to be stable. In our case a 24 hours period was assumed, in order to carry out the analysis on a daily basis.

A corrected map is then obtained by the ratio between the Data map and the Reference map. A value of unity in such map means then isotropy. To reduce the statistical error on the Reference map, 20 fake events were generated for each real event, as it is common practice, with a proper normalization. As an example, Fig.5.6 shows the raw Data map (top), the Reference map (middle) and the corrected map (bottom) for a single day of data taking. Taking into account the considerations of the previous Sections, a grid of  $3^\circ \times 3^\circ$  was assumed.

## 5.2 Overall results and discussion

Various datasets, from different telescopes, were analyzed to compare results obtained in different geographical locations and look at the sky map to search for possible deviations from an isotropic pattern.

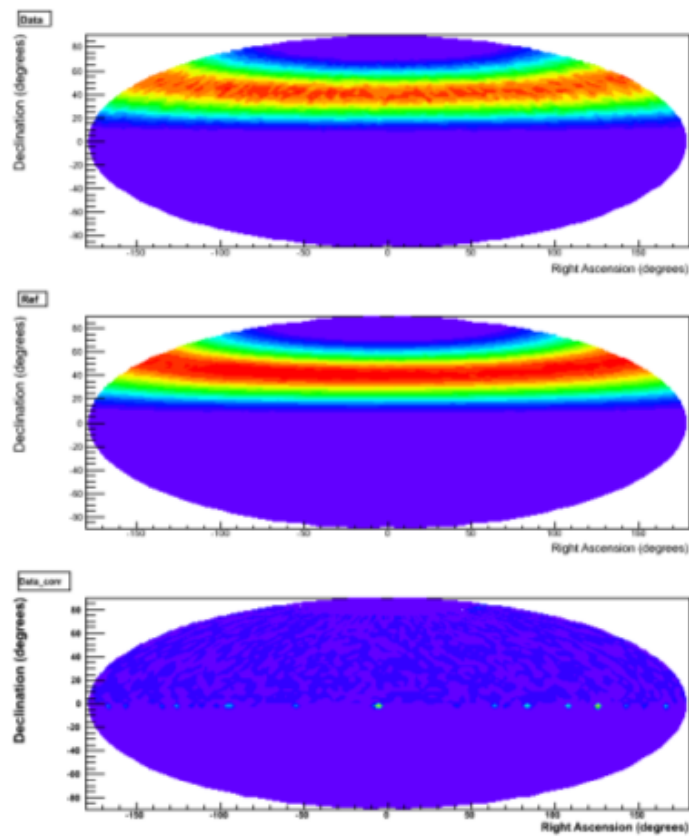


Figure 5.6: Aitoff maps of the sky showing generated events (top map) and accepted events (middle). The ratio between the two maps gives the corrected map, shown on the bottom..

An overall number of about  $1.9 \cdot 10^9$  events were considered in the present analysis, from two different period with the aims to confront two different positions of the Earth along its orbit. The first data set were acquired in April 2015, the second around in November 2015, when approximately the Earth was at the opposite side in the ecliptic, subject to the most different conditions it is possible to obtain with surface detectors. The EEE stations, their geographical locations and the data taking period are listed in Table I (April 2015) and Table II (November 2015).

Results obtained from each individual day in a single telescope station were summed together, with a weight proportional to the number of collected events in each day.

Corrected maps produced in days when the data acquisition has been presented a large discontinuity was excluded from the sample. In fact the scrambling method is not able to correct data maps if there were some interruptions in the data acquisition. Due to the geometrical acceptance of the telescopes, the range between  $21^\circ$  and  $60^\circ$  was considered, to avoid border effects where statistics is low and correspondingly higher statistical fluctuations are observed. For each individual sky map the average number of events in each grid cell ( $3^\circ \times 3^\circ$ ) is of the order of  $10^5$ , with statistical uncertainties around 1%.

*April 2015* The data sample of  $\sim 820 \cdot 10^6$  events collected in a continuous period of 15 days in April 2015 from 25 stations with good tracks parameters (see section 4.1, 3.5.6), were selected, and tracks with  $\chi^2 < 10$  were analyzed.

Figures 5.9-5.8 show the corrected maps for some sites: LAQU-02, SAVO-03, SAVO-01, ALTA-01.

*November 2015* The data sample of  $\sim 960 \cdot 10^6$  events collected in a period of 15 days in November 2015 from 26 station with stable tacks parameters were selected, and tracks with  $\chi^2 < 10$  were analyzed.

Figures 5.9-5.10 show the corrected maps for some sites: LAQU-01, FRAS-03, BOLO-01, CAGL-01.

In the datasets both, apart from a few cells, mostly located close to the border regions, the majority of the cells exhibit variations within 2-3%, compatible with the isotropy hypothesis, within the statistical uncertainties associated to the number of events analyzed. Since the geographical locations of the various EEE sites are not too much different each other and

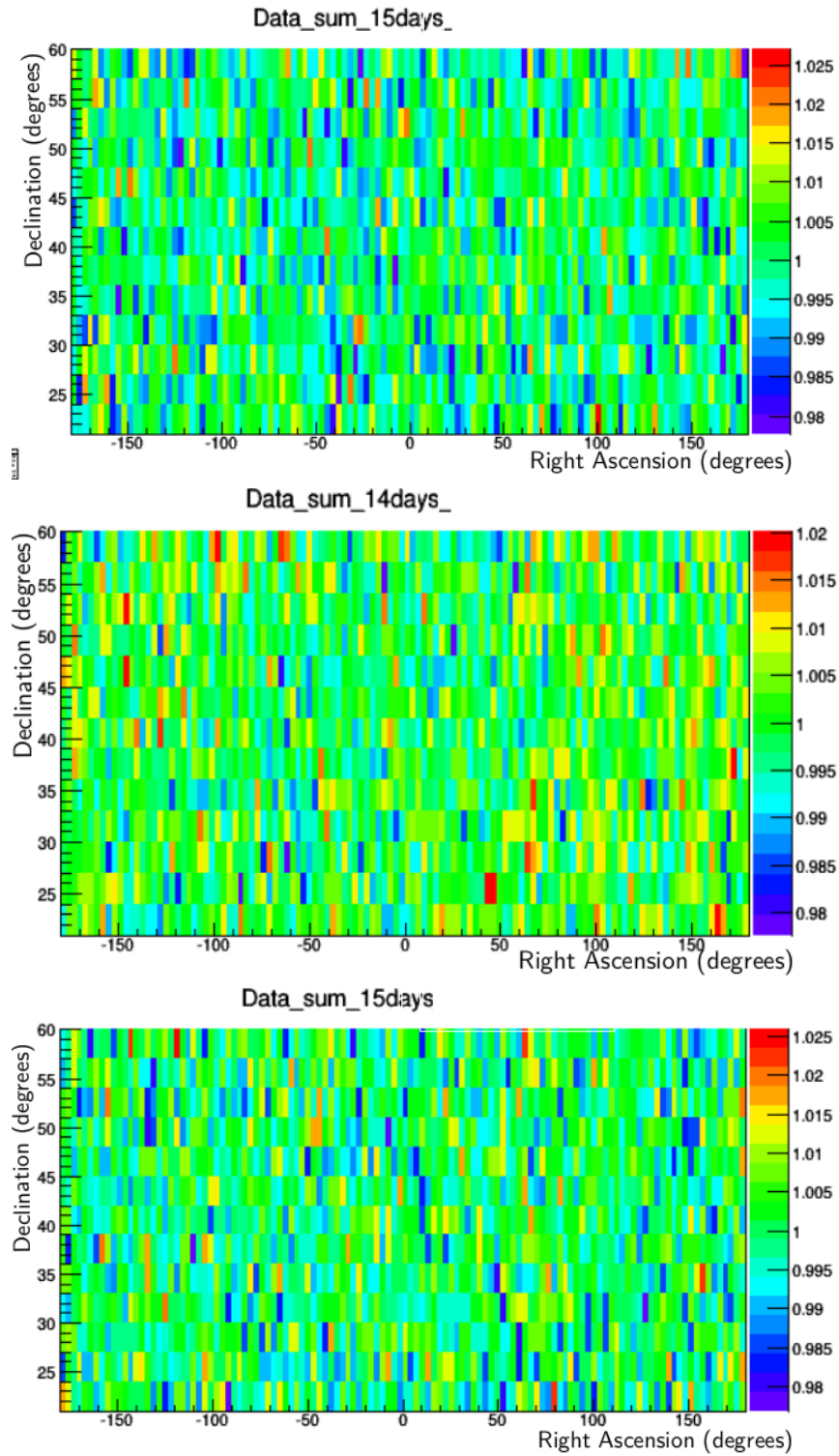


Figure 5.7: Correct Aitoff maps, from  $21^\circ$  to  $60^\circ$  in Declination, relative to 15 days in April 2015 from SAVO-03 (top), SAVO-01 (middle) and LAQU-02 (bottom) sites.

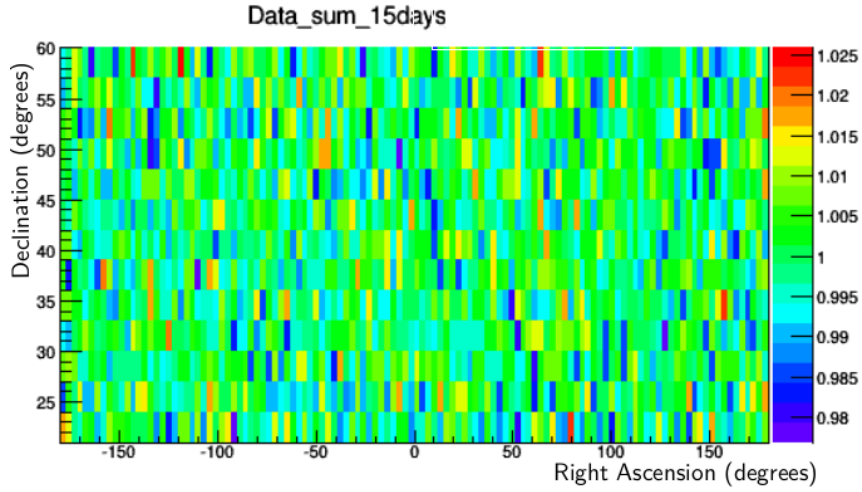


Figure 5.8: Aitoff map correct, from  $21^\circ$  to  $60^\circ$  in Declination, relative to 15 days in April 2015 from ALTA-01.

the various sites are all at the sea level with a similar amount of shielding above them (hence similar muon thresholds), one can in principle sum the various maps with a proper weight given by the number of events collected in each site. The result from the April dataset is reported in Figure 5.11 and from November in Figure 5.12. The results shows how the cell-to-cell fluctuations are further reduced, down to the level of 0.5 % for the dataset both. The results from the two dataset collected during periods distance six month do not show particular differences, and it is possible to think that the variations of some single telescopes were due to local meteorological parameters or magnetic features.

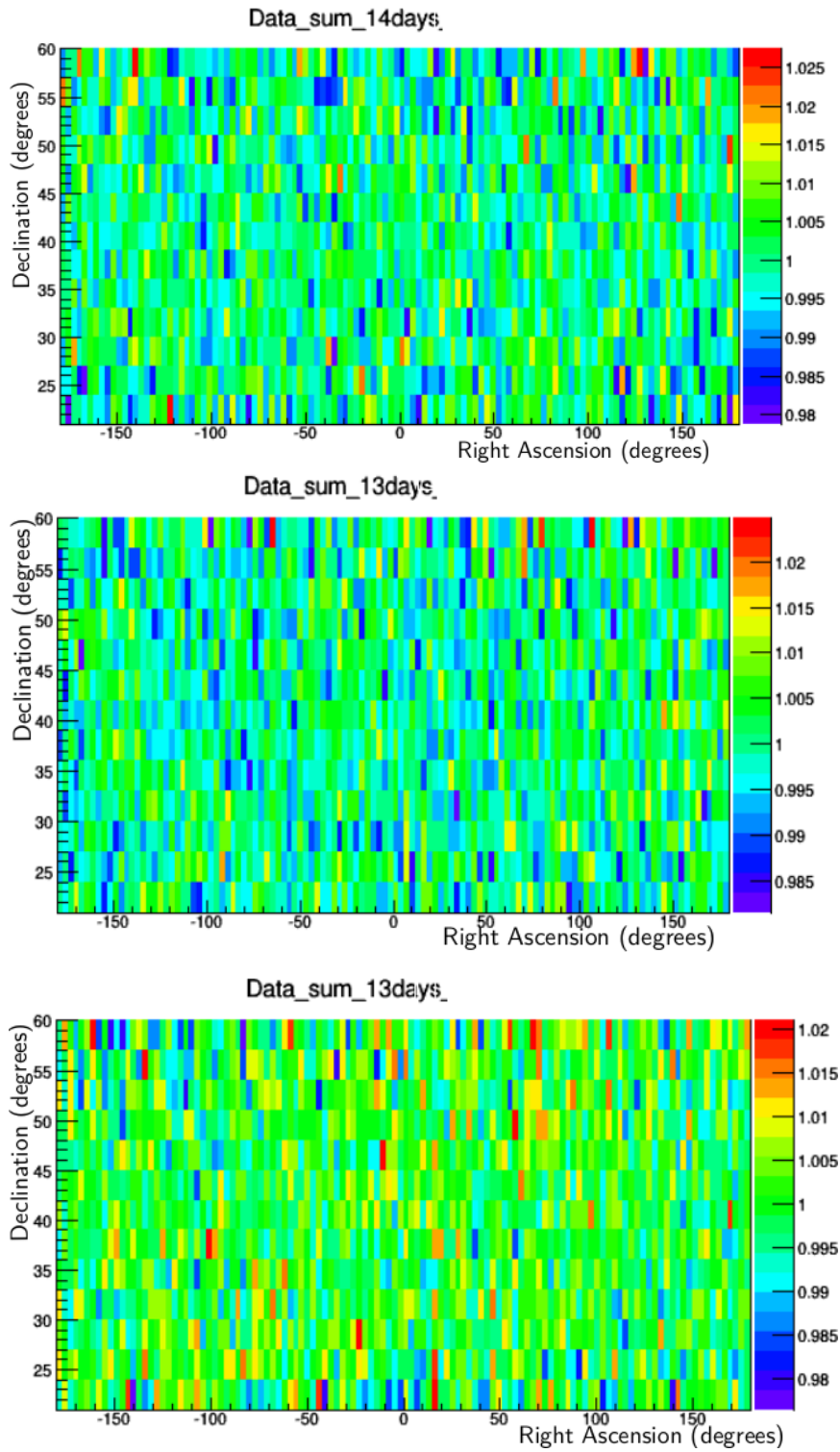


Figure 5.9: Correct Aitoff maps, from  $21^\circ$  to  $60^\circ$  in Declination, relative to 15 days in April 2015 from LAQU-01 (top), FRAS-03 (middle) and BOLO-01 (bottom) sites.

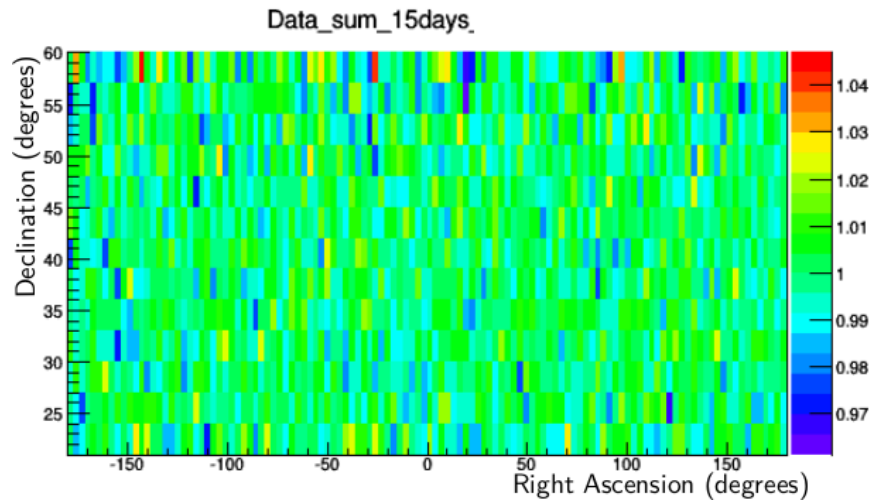


Figure 5.10: Aitoff map correct relative to 15 days in November 2015 from CAGL-01,  $21^\circ$  to  $60^\circ$ .

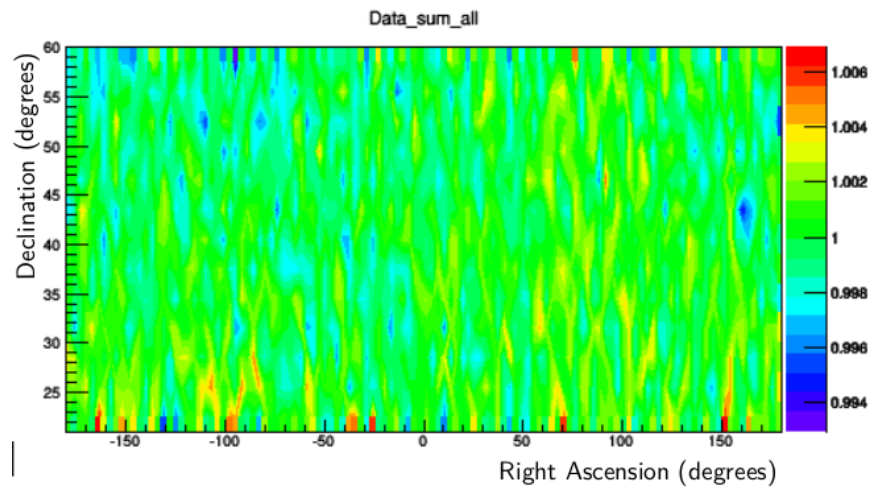


Figure 5.11: Correct Aitoff map summed over the available statistics ( $7.0 \cdot 10^8$  tracks) from the different sites of the *April* dataset.

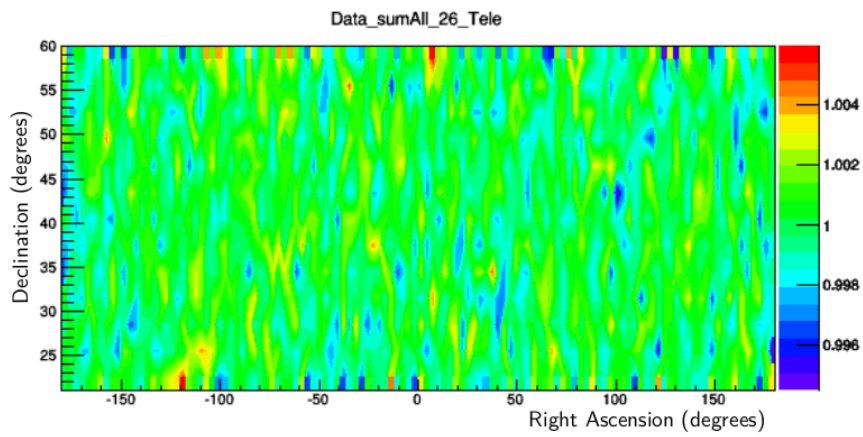


Figure 5.12: Correct Aitoff map summed over the available statistics ( $8.8 \cdot 10^8$  tracks) from the different sites of the *November* dataset.

## Chapter 6

# Conclusion

A analysis of a dataset of cosmic muon tracks detected in various sites of the EEE network has been carried out to build a skymap in equatorial coordinate and look for possible anisotropies in an energy region of the primary cosmics dominated by sub-TeV extensive air showers, where the influence of the eliosphere and local magnetic fields could play an important role. More than  $10^9$  events, collected by 25 EEE telescopes distributed over the Italian territory, were fully reconstructed after track quality selection. Raw data were corrected for the time exposure of each telescope and its geometrical acceptance by the scrambling method, and corrected maps were extracted and plotted as a function of the Right Ascension and Declination. Corrected data maps are compatible with isotropic distributions at the level of 0.005-0.01, resulting from the statistical fluctuations associated to the number of analyzed events. The amount of analyzed data is currently only a fraction of the overall statistics collected so far by the EEE network. The recent RUN3, which went on for a period of seven months, gave approximately  $20 \times 10^9$  events, a factor 10 with respect to the sample analyzed in the present paper, and the ongoing data taking will give the possibility to increase the available data sample even further, allowing to probe disomogeneities of the order of 0.001. Additional analyses might then be carried out in the near future to search for deviations from an isotropic pattern at a deeper confidence level.



## Appendix A

# Appendix: LV/HV Voltage Control System



Figure A.1: *a* – On top: unit's front panel. *b* – On bottom: unit's back panel.

First prototype of the LV/HV Voltage Control System, VCS, was realized more than five years ago. Ever since more than 30 modules have been operating in the MRPCs telescopes array. This power supply unit which provides DC/DC converters with the input voltage, are designed, developed

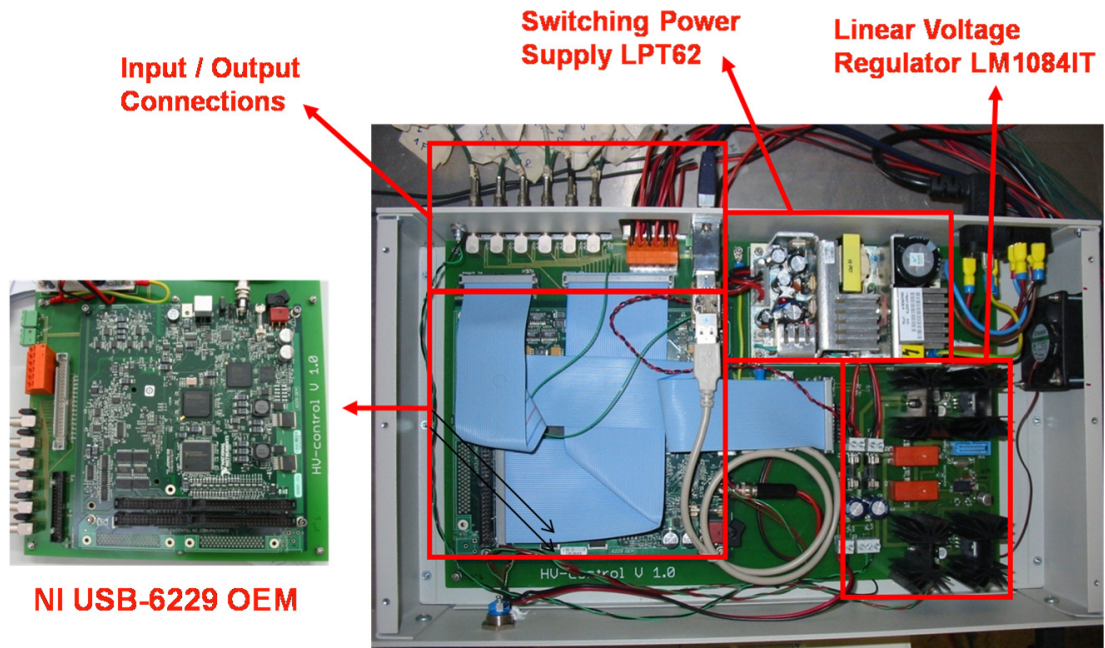


Figure A.2: Voltage Control System main components.

and tested in the INFN Electronic Laboratory of Lecce [133].

The Voltage supply module is embedded in a  $430 \times 240 \times 80 \text{ mm}^3$  metallic box, to be mounted in a 19" standard rack (Fig.A.1).

In Fig.A.1a, the front panel of this module shows:

- Standby/On switch, *S/O*
- Two LEDs to show the module status, the upper one indicates the device status (Standby/On LED), the lower one indicates the status of the data transfer to PC, *Link*.

In Fig.A.1b, the back panel shows:

- Mains switch
- Power cord connector ( $220 \text{ V} - 50 \text{ Hz}$ )
- *Kill* input (TTL pulse of width  $> 50 \text{ ns}$ )
- 6 DC/DC converters power supply outputs
- 2 FE boards power supply outputs

- Sense input from FE boards, monitoring the FE voltage (2.5 V) and balancing attenuation of the FE power cables.  $S$
- *USB* port
- 12 *HV/Current* monitor *Inputs* for reading and monitoring six DC/DC converters through coaxial cables.

Each cable connected on both FE outputs is split in three cables to power each MRPC FE boards. The block schematic diagram of the Voltage Control

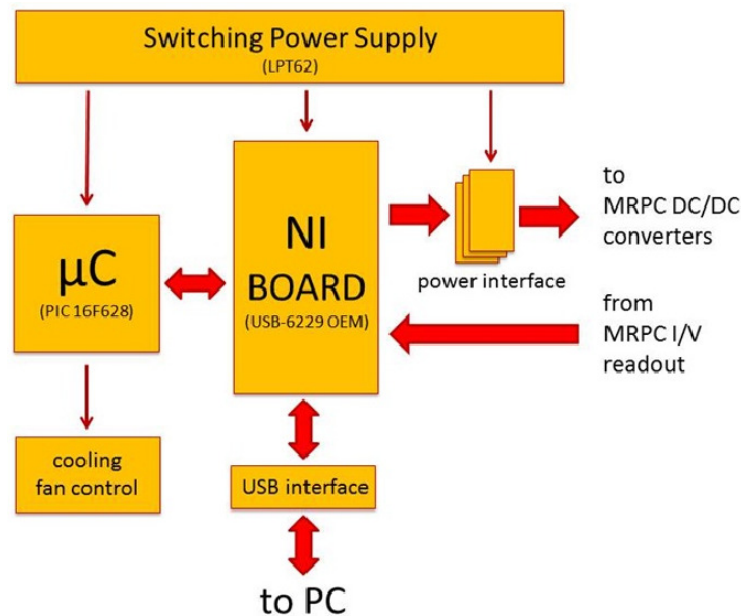


Figure A.3: LV/HV Control System block schematic diagram.

System (VCS) is shown in Fig.A.3. A synthetic description is delineated in what follows [133] (Fig.A.2). The main component of the circuit is the DAQ module, the NI module (NI USB-6229 OEM [135]). This unit is interfaced to a PC through a standard USB port.

The NI module is controlled by a dedicated software in LabVIEW platform [159], (Fig.A.4). Through this software it is possible to set both low voltages to DC/DC converters and FE boards and to check on both HV/current from MRPCs and sense voltage from FE boards. The NI module is equipped with enough analog and digital inputs/outputs to measure all the voltages from DC/DC converters and FE boards (32 analog inputs, 48



Figure A.4: LV/HV control system graphic interface. 1. LV to DC/DC converters; 2. VCS status; 3. HV and currents from MRPCs; 4 Temperature of the VCS board and sense voltage from FE boards

digital I/O's and 4 digital to analog converters). The input high impedance of the internal ADCs of the NI module ( $>10\text{ G}\Omega$  in parallel to  $100\text{ pF}$ ) is useful to measure the voltages from the voltage dividers inside the DC/DC converter with a minimum influence. Since an OEM version of NI module is available, it can be directly embedded in the VCS's main board, as shown in Fig.A.2.

The power for DC/DC converters and FE boards is supply by a Switching Power Supply (SPS) (LPT62 [157]). It was selected to be able to supply different voltages for all the units inside the VCS,  $5\text{ V}$  (to the FE boards and the VCS internal logic) and  $12\text{ V}$  (to the DC/DC converters and NI module). The power for DC/DC converters and FE boards is regulated by the NI module by means of 4 linear voltage regulators LM1084IT-ADJ [160](LVRs), through 4 DACs (3 for the DC/DC converters, 1 for all the FE boards).

A command from the PC via the USB port enables the output voltage for both the DC/DC converters and the FE boards. This command is received by the NI module, converted into a single bit transition and transferred to a microcontroller PIC16F628 ( $\mu\text{C}$ ) [158]. The  $\mu\text{C}$  drives 4 relays connected downstream the LVRs. Whatever a TTL pulse of width  $> 50\text{ ns}$  is applied

to *Kill Input* the  $\mu\text{C}$  switches to zero the voltage to the DC/DC converters and to FE boards both in a time less than 5 ms. The  $\mu\text{C}$  also control a fan for the cooling of the VCS module.

An interface located between the PC and the NI module, avoids NI module's resetting to the default parameters in case of communications failures with the PC, due to USB cable's disconnections, PC reboot, system operator crashes, etc. This interface sends a signal to the Ni module, to emulate the communications with PC and to allow the Ni module to preserve last setting values (*Standby mode*).



# Bibliography

- [1] McLennan, J.C., Burton, E.F., *Physic. Rev.* 16, 184 (1903)
- [2] Rutherford E., Cooke H.L., *Ibid.* 16, 183 (1903)
- [3] Gockel, A.: *Physikalische Zeitschrift* 11, 280 (1910)
- [4] Wulf T., *About the radiation of high penetration capacity contained in the atmosphere*, *Physik. Zeitschr.* 10th year, no.5, pages 152-157 (1910)
- [5] Hess V. F., *Über Beobachtungen der durchdringenden Strahlung bei sieben Freiballonfahrten*. *Physik. Zeitschr.*, 13, pages 1084-1091, (1912)
- [6] Pacini D., *La radiazione penetrante alla superficie ed in seno alle acque*, *Il Nuovo Cimento*, 3 (1912) 93.
- [7] Millikan, R. A. *High Frequency Rays of Cosmic Origin*, *Proc. of the National Academy of Sciences U.S.A.* 12, no. 1, pages 48-55 (1926)
- [8] Bothe W., Kohlhoster W., *Z. S. Phys* 56, 751 (1929).
- [9] Bothe W., Kohlhoster W., *Das Wesen der Hohenstrahlung*, *Z. Phys.* Bd.56 (1929) S.751.
- [10] Compton, A.H.: *Physical Review* 43, 387 (1933)
- [11] Auger P., Ehrenfest P., Maze R. et all, *Extensive cosmic-ray showers*, *Rev. Mod. Phys.* 11 (1939), 288-291.
- [12] Rossi B., *Cosmic Rays*, George Allen and Unwin LTD., London 1964.
- [13] Stormer C., *Terrestrial Magnetism and Atmospheric Electricity*, 35, 139 (1930).
- [14] Compton A.H., *Physical Review* 41, 111, (1932)

- 
- [15] Anderson, C.D. and Neddermeyer, S.H., Physical Review 50, 263 (1936)
- [16] Anderson C. D., Phys. Rev. 43, 491, (1933)
- [17] Dirac P. A. M., Proc. Roy. Soc. A 117, 610 (1928).
- [18] Blumer J. and Matthews J., *The northern site of the Pierre Auger Observatory* New J. Phys. 12, (2010) M.S. Longair, High Energy Astrophysics, 2nd edn. (Cambridge University Press, Cambridge, 1994).
- [19] Compton, A. H. and Getting, I. A. 1935, Phys. Rev., 47, 817.
- [20] . Aglietta, M., et al. 1996, ApJ, 470, 501.
- [21] Amenomori, M. et al. 2004, Phys. Rev. Lett., 93, 61101
- [22] Abbasi R. et al, Astrophys. Journal 718(2010)L194
- [23] Guillian G. et al., Phys.Rev. D75 , 063002 (2007)
- [24] Amenomori, M. et al. 2006, Science 314 (2006)439
- [25] Abdo A.A. et al. APJ 698 (2009)2121
- [26] Nagashima, K., Fujimoto, K., and Jacklyn, R. M. 1998, J. Geophys. Res., 103, 17429.
- [27] Kulikov G. and Kristiansen G., On the size spectrum of extensive air showers, Journal of Experimental and Theoretical Physics 35, (1958), 441-444.
- [28] Sun X. H., Reich W., Waelkens A., and Ensslin T. A., Radio Observational Constraints on Galactic 3D-Emission Models. Astron. Astrophys. 477, (2008), 573-592, arXiv:0711.1572.
- [29] Knurenko S. P. et al., Characteristics of EAS and primary particle mass composition in the energy region of  $10^{17} - 3 \cdot 10^{19}$  eV, by Yakutsk data, Nucl. Phys. Proc. Suppl. 151 (2006), 92-95, astro-ph/0411483.
- [30] Ave M. et al., Mass composition of cosmic rays in the range  $2 \cdot 10^{17} - 3 \cdot 10^{18}$  measured with the Haverah Park Array, Astropart. Phys. 19 (2003), 61-75.

- [31] Bird D. et al., Study of Broad-Scale anisotropy of Cosmic-Ray arrival directions from  $2 \times 10^{17}$  eV to  $10^{20}$  eV from Fly's Eye data , *Astrophys. J.* 511 (1999), 739-749.
- [32] Nagano M. et al., Energy spectrum of primary cosmic rays between  $10^{14.5}$  eV and  $10^{18}$  eV, *J. Phys. G10* (1984), 1295.
- [33] Nagano M. et al., Energy spectrum of primary cosmic rays above  $10^{17}$  eV determined from the extensive air shower experiment at Akeno, *J. Phys. G18* (1992), 423-442.
- [34] Abbasi R. et al. (HiRes Collaboration), Observation of the GZK cutoff by the HiRes experiment , *Phys. Rev. Lett.* 100 (2008), 101101, [astro-ph/0703099](https://arxiv.org/abs/astro-ph/0703099).
- [35] Greisen K., The Extensive Air Showers, *Prog. Cosmic Ray Phys.* III (1956), 1-141.
- [36] Zatsepin G. T. and V. A. Kuzmin, Upper limit of the spectrum of cosmic rays, *JETP Lett.* 4 (1966), 78-80.
- [37] Muecke A. et al., Monte-Carlo simulations of photohadronic processes in astrophysics. *Comput.Phys. Commun.* 124, (2000) 290-314.
- [38] Kotera K., A.V. Olinto, The astrophysics of ultrahigh-energy cosmic rays, *Annu. Rev. Astron.Astrophys.* 49, (2011) 119-153, [arXiv:1101.4256](https://arxiv.org/abs/1101.4256),
- [39] Bleeker J. A., *The Century of Space Science*. Springer, 2001.
- [40] Ahn H. S. et al. Discrepant Hardening Observed in Cosmic-ray Elemental Spectra. *Astrophys. J. Lett.* 714, (2010) L89-L93.
- [41] Abbasi R. et al. Cosmic Ray Composition and Energy Spectrum from 1-30 PeV using the 40-string Configuration of IceTop and IceCube. *Astropart. Phys.* 42, (2013) 15-32. [arXiv:1207.3455](https://arxiv.org/abs/1207.3455).
- [42] Apel W. D. et al. Kneelike Structure in the Spectrum of the Heavy Component of Cosmic Rays Observed with KASCADE-Grande. *Phys. Rev. Lett.* 107 (17), 2011, [arXiv:1107.5885](https://arxiv.org/abs/1107.5885).
- [43] Abraham J. et al. Measurement of the Depth of Maximum of Extensive Air Showers above  $10^{18}$  eV, *Phys. Rev. Lett.* 104 (2010), 91-110. [arXiv:1002.0699](https://arxiv.org/abs/1002.0699).

- 
- [44] Ikeda D. et al. Recent Results of the Energy Spectrum and Mass Composition from Telescope Array Fluorescence Detector, *J. Phys. Conf. Ser.* 409 (2013), 12-97.
- [45] Hayashida N. et al. (Agasa Collaboration), The anisotropy of cosmic ray arrival direction around  $10^{18}$  eV, *Astropart. Phys.* 10 (1999), 303-311, astro-ph/9906056.
- [46] Roth M. (Pierre Auger Collaboration), Measurement of the UHECR energy spectrum using data from the Surface Detector of the Pierre Auger Observatory, arXiv:0706.2096 astro-ph.
- [47] Perrone L. (Pierre Auger Collaboration), Measurement of the UHECR energy spectrum from hybrid data of the Pierre Auger Observatory, 0706.2643.
- [48] Facal San Luis P. (Pierre Auger Collaboration), Measurement of the UHECR spectrum above 10 EeV at the Pierre Auger Observatory using showers with zenith angles greater than 60 degrees, 0706.4322.
- [49] Wefel F., Cosmic rays, supernovae and the interstellar medium, NATO ASIC Series 337, (1991), 29.
- [50] Fermi E., On the Origin of the Cosmic Radiation, *Phys. Rev.* 75 (1949), 1169-1174.
- [51] Longair M.S., High Energy Astrophysics 2nd edn., Cambridge University Press, Cambridge, (1994).
- [52] Grupen C., Astroparticle Physics. Springer, (2005).
- [53] Drury L. O., An introduction to the theory of diffusive shock acceleration of energetic particles in tenuous plasmas, *Reports of Progress in Physics* 46 (1983), 973-1027.
- [54] Enomoto R. et al., The Acceleration of cosmic ray protons in the supernova remnant RX J1713.7-3946, *Nature* 416 (2002), 823-826.
- [55] Aharonian F. A. et al. (The HESS Collaboration), High-energy particle acceleration in the shell of a supernova remnant, *Nature.* 432 (2004), 75-77, astro-ph/0411533.

- 
- [56] Cesarsky C. J. and Montmerle T., Gamma rays from active regions in the galaxy -The possible contribution of stellar winds, *Space Sci. Revs.* 36 (1983), 173-193.
- [57] Jokipii J. R. and Morfill G., Ultra-high-energy cosmic rays in a galactic wind and its termination shock, *Astrophys. J.* 312 (1987), 170-177
- [58] Harding A. K. and Gaisser T. K., Acceleration by pulsar winds in binary systems, *Astrophys. J.* 358 (1990), 561-574.
- [59] Cheng K. S., Ho C. and Ruderman M., Energetic radiation from rapidly spinning pulsars, I. Outer magnetosphere gaps, II. VELA and Crab, *Astrophys. J.* 300 (1986), 500-539.
- [60] Sigl G., The enigma of the highest energy particles of nature, *Ann. Phys.* 303 (2003), 117-141.
- [61] Ackermann M. et al., Detection of the Characteristic Pion-Decay Signature in Supernova Remnants. *Science*, 339 (2013), 807-811, arXiv:1302.3307.
- [62] Hillas A. M., The Origin of Ultra-High-Energy Cosmic Rays. *Annu. Rev. Astron. Astrophys.*, 22 (1984), 425-444.
- [63] Anchordoqui L. A. and Montaruli T., In Search of Extraterrestrial High-Energy Neutrinos. *Annu. Rev. Nucl. Part. Sci.*, 60 (2010), 129-162, arXiv:0912.1035.
- [64] Paneque D., Experimental Gamma-Ray Astronomy, *J. Phys. Conf. Ser.*, 375 (5) (2012).
- [65] Atwood W. B. et al. The Large Area Telescope on the Fermi Gamma-Ray Space Telescope Mission. *Astrophys. J.*, 697 (2009), 1071-1102, arXiv:0902.1089.
- [66] Ackermann M. et al. Detection of the Characteristic Pion-Decay Signature in Supernova Remnants. *Science*, 339 (2013), 807-811, arXiv:1302.3307.
- [67] Baade W. and Zwicky F., Cosmic Rays from Supernovae. *Proceedings of the National Academy of Science*, 20 (1934), 259-263.

- [68] Ginzburg V. L. and Syrovatskii S. I., *The Origin of Cosmic Rays*. Gordon and Breach, 1964.
- [69] Abdo A. A. et al., TeV Gamma-Ray Sources from a Survey of the Galactic Plane with Milagro. *Astrophys. J. Lett.*, 664 (2007), L91-L94, arXiv:0705.0707.
- [70] Funk S., *The Status of Gamma-Ray Astronomy*. In Proc. of the 32nd ICRC, Beijing, (2011).
- [71] Spurio M., *Particles and Astrophysics. A Multi-Messenger Approach Astronomy and Astrophysics Library*, Springer, 2015.
- [72] Abbasi R. et al. An Absence of Neutrinos Associated with Cosmic-Ray Acceleration in  $\gamma$ -Ray Bursts. *Nature*, 484 (2012), 351-354, arXiv:1204.4219.
- [73] Abraham J. et al. Correlation of the Highest-Energy Cosmic Rays with the Positions of Nearby Active Galactic Nuclei. *Astropart. Phys.*, 29 (2008), 188-204, arXiv:0712.2843.
- [74] TeV Gamma-ray catalog, TeVCat website: <http://tevcat.chicago.edu> .
- [75] Obermeier A., Boyle P., Horandel J., and Muller D. The Boron-to-Carbon Abundance Ratio and Galactic Propagation of Cosmic Radiation. *Astrophys. J.*, 752 (2012), 69, arXiv:1204.6188.
- [76] Aguilar M. et al. (AMS-02 collaboration), AMS-02 provides a precise measure of cosmic rays. *CERN Courier* 53 (2013) 8, 23-26.
- [77] Evoli C., Gaggero D., Grasso D., and Maccione L., Cosmic Ray Nuclei, Antiprotons and Gamma Rays in the Galaxy: a New Diffusion Model, *J. Cosmol. Astropart. Phys.*, 10 (2008), 68, arXiv:0807.4730.
- [78] Farrar F. R., Jansson R., Feain I. J., and Gaensler B., Galactic magnetic deflections and Centaurus A as a UHECR source. *J. Cosmol. Astropart. Phys.*, 1 (2013), 23 arXiv:1211.7086.
- [79] Berenzinskii V. S. et al., *Astrophysics of cosmic rays*, North-Holland, (1990).
- [80] Gaisser T. K., *Cosmic Rays and Particle Physics*. Cambridge University Press, (1990).

- [81] Jansson R. and Farrar G. R., A New Model of the Galactic Magnetic Field, *Astrophys. J.*, 757 (2012), 14, arXiv:1204.3662.
- [82] Gleeson L.J. and Axford W.I., *Solar modulation of galactic cosmic rays*, *Astrophysical Journal*, 168, 1011-1026, 1968.
- [83] Riley P., Linker J.A., Mikic Z., *Modeling the heliospheric current sheet: Solar cycle variations* *Journal of Geophys. Res.*, 107, 1136, 2002.
- [84] Singh M., Singh, Badruddin Y.P., *Solar Modulation of galactic cosmic rays during the last five solar cycles*, *Jour. Atm. Solar Phys.*, 70, 169-183, 2008.
- [85] Parker E.N., *The passage of energetic charged particles through interplanetary space*, *Planetary and Space Science* 13, 9, 1965.
- [86] <http://www.bartol.udel.edu/gp/neutronm/>
- [87] Mitchell W., Abe K. , Fuke H., *Solar Modulation of Low-Energy Antiproton and Proton Spectra Measured by BESS*. *International Cosmic Ray Conference*, vol. I, 455 - 458, 2008.
- [88] Wiebel-Sooth B., Biermann P.B. and Meyer H., *Cosmic rays VII. Individual element spectra: prediction and data*, *Astron. Astrophys.* 330(1998), 389-398.
- [89] Rossi B., *Cosmic Rays*, George Allen and Unwin LTD., London 1964.
- [90] Smart D.F., M.A. Shea, *Advances in Space Research*, 36, 2012-2020, 2005.
- [91] Patrignani C. et al. (Particle Data Group), *Chin. Phys. C*, 40, 100001 (2016).
- [92] Allkofer O.C. et al., *Astrophysical Sources of High Energy Particles and Radiation*, *Lett. Nuovo Cim*, 12 (1975) 107.
- [93] Cecchini S., Sioli M., *Cosmic Ray Muon Physics*, (2000), arXiv:hep-ex/0002052.
- [94] . Dorman L. I., *Cosmic Ray Variation*, State Publ. House for Tech. and Theor. literature Moscow, translation by US Air Force Tech. Doc. Liason Office (1958).

- [95] T. Antoni et al. (KASCADE Collaboration), Electron, muon, and hadron lateral distributions measured in air showers by the KASCADE experiment, *Astropart. Phys.* 14 (2001), 245-260, astro-ph/0004233.
- [96] K. Greisen, The Extensive Air Showers, *Prog. Cosmic Ray Phys.* III (1956), 1-141.
- [97] K. Kamata and J. Nishimura, The Lateral and the Angular Structure Functions of Electron Showers, *Prog. of Theo. Phys. Suppl.* 6 (1958), 93-155.
- [98] P. Duffet-Smith and J. Swart, *Practical Astronomy with your calculator or spreadsheet*, Cambridge University Press 2011.
- [99] Centro Fermi web site: <http://www.centrofermi.it/eee>.
- [100] Zichichi A., Progetto “La Scienza nelle Scuole” - EEE: Extreme Energy Events (Società Italiana di Fisica, Bologna, 2004).
- [101] W. Brouwer et al., The ALTA cosmic ray experiment electronics system, *Nucl. Instr. and Meth. A* 539 (2005) 595-605.
- [102] Proceedings of the 31st ICRC, 2009, ALTA/CZELTA - a sparse very large air shower array: overview of the experiment and first results,
- [103] S. Giani, C. Leroy, P. G. Rancoita, *Cosmic Rays for Particle and Astroparticle Physics*, World Scientific, 2011.
- [104] R. D. McKeown, B. E. Carlson, E. Brobeck, C. J. Jillings, M. B. Larson, T. W. Lynn, J. E. Hill, B. J. Falkowski, R. Seki, J. Sepikas, G. B. Yodh Search for Correlated High Energy Cosmic Ray Events with CHICOS, 29th ICRC Pune (2005) 6, 377-380.
- [105] T. J. Haines, The status of the CYGNUS experiment: Past, present, and future, *Nucl. Phys. B Proc. Suppl.* 14 (1990) 244-249.
- [106] <http://www.hisparc.nl/en/>
- [107] R. Hart, B. van Eijk, D. Fokkema, A. de Laat, The HiSPARC control system, 14th ICALEPCS (2013) 2, 1220-1223.
- [108] C. Timmermans, HiSPARC collaboration, Setup and first results of the HiSPARC experiment, 29 ICRC (2005) 00, 101-104.

- 
- [109] Apel, W.D. et al. - LOPES collaboration, LOPES-3D: An antenna array for full signal detection of air-shower radio emission, Nucl. Instr. and Meth. A (2012) 696 100-109.
- [110] H. Rottgering, Lofar a new low frequency telescope, New Astronomy Reviews (2003) 47:405.
- [111] T. Helio, MARIACHI - Detecting Ultra High Energy Cosmic Rays with radar, APS Meeting (2006).
- [112] P. Hofverberg, M Pearce, Cosmic ray anisotropy studies with the Stockholm Educational Air Shower array, arXiv:1112.3902.
- [113] M. Abbrescia et al., The EEE project: cosmic rays, multigap resistive plate chambers and high school students, JINST 7 (2012) P11011.
- [114] M. Abbrescia et al., Extreme Energy Events Project: construction of the detectors and installation in Italian High Schools, Nucl. Instrum. Meth. A **588** (2008) 211.
- [115] An S. et al., Multigap resistive plate chambers for EAS study in the EEE Project, Nucl. Instrum. Meth. A **581** (2007) 209-212
- [116] M. Abbrescia et al. (EEE collaboration), Nuovo Cimento B **125**, 243 (2010).
- [117] ALICE Collaboration, Addendum to TOF Technical Design Report, CERN/LHC, 2002-016.
- [118] R. Santonico and R. Cardarelli. Development of resistive plate counters. Nucl. Instr. and Meth. **187** (1981) 377-380.
- [119] R. Santonico and R. Cardarelli. Progress in resistive plate counters. Nucl. Instr. and Meth. A **263** 20-25 (1988).
- [120] Yu. N. Pestov et al., A spark counter with large area, Nucl. Instr. and Meth. **93**, (1971) 269-276
- [121] G.F. Knoll, Radiation Detection and Measurement, Wiley, 1989
- [122] W-M Yao et al., J. Phys. G: Nucl. Part. Phys. 33 (2006) 1.

- [123] R.Cardarelli, V.Makeev, R.Santonico, Avalance and streamer mode operation of resistive plate chambers. Nucl. Instr. and Meth. A **382**, (1996) 470-474.
- [124] H. Raether, Electron avalanche and breakdown in gases, London Butterworths 1964.
- [125] P. Camarri, R. Cardarelli, A. Di Ciaccio, R. Santonico, Streamer suppression with SF 6 Nucl. Instr. and Meth. **414**, (1998) 317.
- [126] R. Arnaldi et al. Study of resistive plate chambers for the ALICE dimuon spectrometer, Nucl. Phys. B - Proc. Suppl.,**78**, (1999) 84-89.
- [127] Proc. II. Int. Workshop on the RPC in Particle Physics and Astrophysics, Pavia (1993).
- [128] E. Cerron Zeballos, I. Crotty, D. Hatzifotiadou, J. Lamas-Valverde, S. Neupane, M. C. S. Williams, A. Zichichi, A new type of resistive plate chamber : the multigap RPC, Nucl. Instr. Meth. A 374, (1996) 132-135.
- [129] A. Akindinov et al., Nucl. Instrum. Methods Phys. Res. A **456**, 16 (2000).
- [130] M. Abbrescia et al. (EEE collaboration) Performance of a six gap MRPC built for large area coverage, Nucl. Instrum. Meth.A **593** (2008) 263-268.
- [131] A. Akindinov, A. Alici, F. Anselmo, P. Antonioli et al., Nucl. Instrum. Meth. A 533 (2004) 93-97.
- [132] F. Anghinolfi et al., NINO: An ultra-fast and low-power front-end amplifier/discriminator ASIC designed for the multigap resistive plate chamber, Nucl. Instrum. Meth. A 533 (2004) 183.
- [133] A. Corvaglia, M. Panareo, M.P. Panetta, C. Pinto, Voltage control system for a Multigap Resistive Plate Chambers telescope, Proceedings of 6th IWASI (2015), 72-74.
- [134] Q101-Q101N Datasheet "Q Series, Isolated, Proportional DC to HV DC Converters"  
<http://www.emcohighvoltage.com/pdfs/qseries.pdf>

- [135] NI USB-6229 OEM Datasheet "M Series Multifunction Data Acquisition NI 622x Specifications + USER GUIDE"  
<http://sine.ni.com/nips/cds/view/p/lang/en/nid/203621#>
- [136] EEE Collaboration, Manuale di installazione ed utilizzo delle schede di trigger del Progetto EEE, internal note.
- [137] R. Brun and F. Rademakers, *ROOT—An Object Oriented Data Analysis Framework*, Nucl. Inst. Meth. Phys. Res. A **389** 81–86 (1997). See also <http://root.cern.ch/>
- [138] EEE monitor: <https://www1.cnaf.infn.it/eee/monitor//>.
- [139] M. Abbrescia et al. (EEE collaboration), Cosmic rays Monte Carlo simulations for the Extreme Energy Events, Eur. Phys. J. Plus (2014). **129**, 166.
- [140] CNAF web site: <https://www.cnaf.infn.it/en/>.
- [141] F. Noferini, The computing and data infrastructure to interconnect EEE stations, Nucl. Instrum. Meth. A 824 (2016) 329–330.
- [142] M. Abbrescia et al., Performance of a six gap MRPC built for large area coverage, Nucl. Instrum. Meth. A 593 (2008) 3.
- [143] M. Abbrescia et al., A Multigap Resistive Plate Chambers for the EAS study in the EEE Project, Proceedings of the 30th ICRC (2008), 5, HE 2, 155–156.
- [144] M. Abbrescia et al., First results from Run1 of the Extreme Energy Events experiment, PoS(ICRC2015), 306, 2015.
- [145] M. Abbrescia et al., A Multigap Resistive Plate Chambers array for the Extreme Energy Events Project, JINST 9 (2014) C10024.
- [146] M. Abbrescia et al., Results from the observations of Forbush decreases by the Extreme Energy Events experiment, PoS(ICRC2015), 097, 2015.
- [147] M. Abbrescia et al., Time correlation measurements from extensive air showers detected by the EEE telescopes, Eur. Phys. J. Plus **128** (2013) 148.

- [148] M.P. Panetta, The EEE Project: an extended network of muon telescopes for the study of cosmic rays. stations, Nucl. Instrum. Meth. A 824 (2016) 642–643.
- [149] EEE Collaboration, M. Abbrescia et al., First detection of extensive air showers with the EEE experiment, Nuovo Cimento B **125** (2010) 243-254.
- [150] M. Abbrescia et al., Looking at the sub TeV sky with cosmic muons detected in the EEE MRPC telescopes, Eur. Phys. J. Plus 130 (2015) 187.
- [151] M Abbrescia et al., A study of upward going particles with the Extreme Energy Events telescopes, Nucl. Instrum. Meth. A 816 (2016) 142–148.
- [152] M. Abbrescia et al., Observation of the February 2011 Forbush decrease by the EEE telescopes, Eur. Phys. J. Plus **126** (2011) 61.
- [153] M. Abbrescia et al., The EEE experiment project: status and first physics results, Eur. Phys. J. Plus **128** (2013) 62.
- [154] R. Antolini et al. (EEE collaboration), *The EEE Project, 29th ICRC Proceedings*, Pune 8, (2005) 279
- [155] M. Ambrosio et al. (MACRO collaboration), Phys. Lett. B Vol. 434, Issue 3-4, 451-457 (1998).
- [156] M. Abbrescia et al. (MACRO collaboration), Eur. Phys. J. Plus (2013) **128**:62.
- [157] LPT62 Datasheet "Switching power supply"  
[https://www.artesyn.com/power/assets/lpt60serie\\_1184686568\\_ds.pdf](https://www.artesyn.com/power/assets/lpt60serie_1184686568_ds.pdf)
- [158] PIC 16f628 Datasheet "FLASH-Based 8-Bit CMOS Microcontrollers"  
<http://pdf1.alldatasheet.com/datasheet-pdf/view/75024/MICROCHIP/16F628.html>
- [159] LabVIEW System Design Software:  
<http://www.ni.com/labview/>
- [160] LM1084IT-ADJ Datasheet "Low Dropout Positive Regulators"  
<http://www.ti.com/lit/ds/symlink/lm1084.pdf>

- [161] B. Rossi, "High Energy Particles", Prentice Hall, 1952.